UNIVERSITY OF ALBERTA

Study of High Harmonic Generation in Ionizing Atomic Gases

BY

Clarence Kwok-Yan Kan ©

A thesis submitted to the Faculty of Graduate Studies and Research in partial fulfillment of the requirements for the degree of Doctor of Philosophy.

DEPARTMENT OF ELECTRICAL AND COMPUTER ENGINEERING

Edmonton, Alberta
Fall 1997

National Library
of Canada

Acquisitions and
Bibliographic Services

395 Wellington Street
Ottawa ON K1A 0N4
Canada

Bibliothèque nationale
du Canada

Acquisitions et
services bibliographiques

395, rue Wellington
Ottawa ON K1A 0N4
Canada

Your file Votre référence

Our file Notre référence

The author has granted a non-exclusive licence allowing the National Library of Canada to reproduce, loan, distribute or sell copies of this thesis in microform, paper or electronic formats.

The author retains ownership of the copyright in this thesis. Neither the thesis nor substantial extracts from it may be printed or otherwise reproduced without the author's permission.

L'auteur a accordé une licence non exclusive permettant à la Bibliothèque nationale du Canada de reproduire, prêter, distribuer ou vendre des copies de cette thèse sous la forme de microfiche/film, de reproduction sur papier ou sur format électronique.

L'auteur conserve la propriété du droit d'auteur qui protège cette thèse. Ni la thèse ni des extraits substantiels de celle-ci ne doivent être imprimés ou autrement reproduits sans son autorisation.

0-612-23001-5

Canada

UNIVERSITY OF ALBERTA

LIBRARY RELEASE FORM

NAME OF AUTHOR: Clarence Kwok-Yan Kan

TITLE OF THESIS: Study of High Harmonic Generation in Ionizing Atomic Gases

DEGREE: Doctor of Philosophy

YEAR THIS DEGREE GRANTED: 1997

Permission is hereby granted to the University of Alberta Library to reproduce single copies of this thesis and to lend or sell such copies for private, scholarly or scientific research purposes only.

The author reserves all other publication and other rights in association with the copyright in the thesis, and except as hereinbefore provided neither the thesis nor any substantial portion thereof may be printed or otherwise reproduced in any material form whatever without the author's prior written permission.

(Signed) Clarence Kan

Clarence Kwok-Yan Kan
10820 19B Avenue
Edmonton, Alberta
Canada T6J 6N7

Date: June 27, 1997

UNIVERSITY OF ALBERTA

FACULTY OF GRADUATE STUDIES AND RESEARCH

The undersigned certify that they have read, and recommend to the Faculty of Graduate Studies and Research for acceptance, a thesis entitled **Study of High Harmonic Generation in Ionizing Atomic Gases** submitted by Clarence Kwok-Yan Kan in partial fulfillment of the requirements for the degree of Doctor of Philosophy.

Dr. C. E. Capjack (Supervisor)

Dr. N. H. Burnett (Supervisor)

R Rankin

Dr. R. Rankin (Supervisor)

D. Routledge (for)

Dr. H. M. Milchberg (External)

Robert Fedosejevs

Dr. R. Fedosejevs (Examiner)

Dr. A. M. Robinson (Examiner)

Dr. W. Rozmus (Examiner)

F.E. Vermeulen

Dr. F. E. Vermeulen (Examiner)

Date: June 25, 1997

To my wife Jocelyn
for her love and support

Abstract

High harmonic generation (HHG) in atomic gases has been considered as a potential coherent x-ray source which can have many important applications in science and engineering. In this Ph.D. thesis, a number of important and practical issues in HHG have been theoretically investigated. These include: (1) spectral and temporal characteristics of the high harmonic emission; (2) improving harmonic conversion efficiency through high order difference frequency mixing (HDM); and (3) generation of attosecond coherent soft-x-ray pulses.

These investigations have been facilitated by the development of a number of computational models which are designed to study HHG at both the microscopic and macroscopic levels. In microscopic studies, a semi-classical dipole model has been used to describe harmonic generation from individual atoms. In macroscopic studies, the one dimensional nonlinear wave equation incorporating the microscopic dipole model has been used to describe harmonic emission from the overall macroscopic medium.

From these studies, several important findings have been obtained. First, it has been found that XUV harmonics can have large spectral blue shifts and linewidths under typical experimental conditions and that these harmonics can be generated with temporal durations of only a few femtoseconds. Secondly, it has been found that as opposed to previous anticipation, HDM cannot be used to increase harmonic conversion efficiency arbitrarily. Finally, it has been found that efficiency coherent soft-x-ray pulses can be generated by using driving lasers with temporal durations of several laser cycles.

Acknowledgements

I would like to thank my supervisors, Dr. C. E. Capjack, Dr. N. H. Burnett and Dr. R. Rankin, for their patient guidance and support during the course of this thesis research.

I would also like to thank Dr. P. B. Corkum and Dr. M. Yu. Ivanov at the National Research Council of Canada for many helpful discussions.

Finally, I would like to thank Dr. T. Brabec at the Technische Universitat Wien for his collaboration on the study of high order difference frequency mixing.

List of Symbols

a	Atomic ground state population
a_B	The Bohr radius
c	Speed of light
d	Atomic dipole moment
d_a	Atomic dipole acceleration
d_v	Atomic dipole velocity
$\Delta\theta_q$	Harmonic phase mismatch
$\Delta\theta_{ql}$	Mixed field phase mismatch
e	Charge of electron
$\underline{E}$	Electric field
$\underline{E}_1$	Fundamental electric field
$\underline{E}_c$	Control electric field
$\underline{E}_h$	High frequency electric field
$\underline{E}_q$	Harmonic electric field
E	Electric field envelope
E_1	Fundamental electric field envelope
E_c	Control electric field envelope
E_h	High frequency electric field envelope
E_q	Harmonic electric field envelope
E_a	Atomic unit of electric field
$FWHM$	Full width at half maximum
γ	The Keldysh parameter

$\hbar$	Planck's constant
HDM	High order difference frequency mixing
HHG	High harmonic generation
I	Laser intensity
I_1	Fundamental field intensity
I_c	Control field intensity
I_h	High frequency field intensity
I_q	Harmonic field intensity
I_p	Ionization potential
I_h	Ionization potential of a hydrogen atom
k_c	Control field wave vector
k_o	Fundamental field wave vector
k_q	Harmonic field wave vector
k_{ql}	Mixed field wave vector
KE	Electron kinetic energy
λ	Wavelength
λ_c	Control field wavelength
λ_o	Fundamental field wavelength
λ_q	Harmonic field wavelength
λ_{ql}	Mixed field wavelength
m	Mass of electron
n_c	Critical number density
n_e	Electron number density
n_o	Background number density
ω	Frequency
ω_a	Atomic unit of frequency
ω_c	Control field frequency
ω_o	Fundamental field frequency
ω_h	High frequency field frequency

ω_{pe}	Plasma frequency
ω_q	Harmonic field frequency
ω_{ql}	Mixed field frequency
P	Ionization probability
$\underline{P}$	Medium polarization
$\underline{P}_q$	Harmonic polarization
P_q	Harmonic polarization envelope
P_{ql}	Mixed field polarization envelope
Ψ, ψ	Atomic wave function
r_s	Electron wavefunction spread
R_t	Tunnel ionization rate
S	The accumulated phase
t_o	Fundamental cycle
t'	Electron release time
t_q	Electron re-collision time
θ_1	Fundamental phase
θ_c	Control field phase
θ_q	Harmonic phase
θ_{ql}	Mixed field phase
θ_h	High frequency field phase
U_p	Ponderomotive potential
v	Electron velocity
v_o	Atomic unit of velocity
v_R	Electron re-collision velocity
V	Atomic potential
x	Electron trajectory
XUV	Extreme ultraviolet
Z	Charge of atomic residue

Contents

1 Introduction **1**

1.1 General HHG Experimental Observations 3

1.2 Theoretical Investigation 5

1.2.1 Single atom analysis 7

1.2.2 Propagation analysis 12

1.3 Scope of Thesis 13

2 Spectral and Temporal Study of High Harmonic Generation **15**

2.1 Single Atom Analysis 16

2.1.1 Tunnel ionization 16

2.1.2 Classical motion of tunnel ionized electrons 20

2.1.3 The semi-classical dipole model 23

2.1.4 The quantum dipole model 29

2.1.5 The ionization model 32

2.1.6 Evaluation of the various dipole moments 33

2.1.7 Results and discussion 37

2.2 Propagation Analysis 56

2.2.1 The one dimensional propagation model 56

2.2.2 The qth harmonic polarization component 59

2.2.3 Simulation results and discussions 61

2.3 Summary and Conclusions 73

3 High Order Difference Frequency Mixing **74**

3.1 The HDM Phase Matching Condition 75
3.2 The Mixed field Atomic Response 77
3.2.1 Preliminary analysis 77
3.2.2 Numerical results 79
3.3 One Dimension Propagation Study 87
3.3.1 Results and Discussion 88
3.4 Summary and Conclusions 102

4 Coherent Attosecond Soft-X-Ray pulses **104**
4.1 Single Atom Analysis 105
4.1.1 Ionization of the atom 105
4.1.2 The dipole response 105
4.2 Propagation Analysis 110
4.2.1 The one dimension model 110
4.2.2 Solving the wave equations 111
4.3 Results and Discussion 112
4.3.1 Understanding of the conversion saturation 116
4.4 Summary and Conclusions 129

5 Two Dimensional Propagation Considerations **130**

6 Conclusions **138**

A Stationary Phase Evaluation of the qth Harmonic Dipole Component **150**

B The One Dimension HHG Wave Solver **152**

C The One Dimension HDM Wave Solver **159**

D Phase and Amplitude of an Ultra-Short Laser Pulse in a Steep Ionization Front **162**

List of Figures

1.1 A typical schematic HHG experimental configuration. 4

1.2 Harmonic spectrum obtained from a 1053 nm, 30 mJ, 1 ps, Nd-glass laser in neon (from Ref. [2]). 6

1.3 Calculated single atom harmonic spectrum for a 1064 nm, 3×10^{13} W/cm^2 laser interacting with xenon from Ref. [19]. Superimposed are the experimental results from Ref. [20]. (The spectra have been adjusted in Ref. [19] to agree at the 7th harmonic.) 9

2.1 (a) The ionizing electric field corresponding to a peak intensity of 5×10^{14} W/cm^2. (b) The tunnel ionization rate for a neon atom in units of t_o^{-1} where the laser period t_o is equal to 2.5 fs. (c) The ionization probability. 19

2.2 (a) The force acting on the electron due to E. (b) The electron trajectories which have negative initial displacements. (c) The electron trajectories which have positive initial displacements. The dashed lines denote those trajectories which will not cross the x-axis again. $F_o = -(e/m)E_o$ and $x_o = -(e/m)(E_o/\omega_o^2)$ 22

2.3 (a) The force acting on the electron due to E. (b) The velocity of the electron during its first re-collision with the parent atom. (c) The kinetic energy of the electron during its first re-collision with the parent atom. $F_o = -(e/m)E_o$, $v_o = -(e/m)(E_o/\omega_o)$ and $U_p = (1/4)(e^2E^2)/(m\omega_o^2)$ 24

2.4 The electron trajectories calculated from two slightly different ionization times. The difference in displacement between these two trajectories at the re-collision time t is denoted by δx. 30

2.5 Dipole acceleration power spectra obtained from (a) the quantum model and (b) the semi-classical model. 38

2.6 Dipole acceleration power spectrum obtained from the Brunel model. A zoom of the first harmonics is shown in the inset. 40

2.7 Zoom of the dipole acceleration spectra near the 55th harmonic component for (a) the quantum model and (b) the semi-classical model. . 41

2.8 Zoom of the dipole acceleration spectra near the 85th harmonic component for (a) the quantum model and (b) the semi-classical model. . 42

2.9 Temporal envelopes of the 55th harmonic dipole acceleration components obtained from (b) the quantum model and (c) the semi-classical model. Shown in (a) are the temporal profiles of the driving laser intensity $I(t)$ and the ionization probability $P(t)$. 43

2.10 Temporal envelopes of the 85th harmonic dipole acceleration components obtained from (b) the quantum model and (c) the semi-classical model. Shown in (a) are the temporal profiles of the driving laser intensity $I(t)$ and the ionization probability $P(t)$. 44

2.11 The re-collision times at which the electrons have the same re-collision energy. 47

2.12 Dipole acceleration power spectrum obtained from the semi-classical model (a) near the 55th harmonic and (b) near the 85th harmonic. The solid lines denote the pre-3.17 component and the dotted lines denote the post-3.17 component. 49

2.13 Dipole acceleration power spectrum near the 55th harmonic obtained from the quantum model with t_a set to $t - nt_o$ where $n = 1, 2, 3, 4$ in (a), (b), (c), (d), respectively. 50

2.14 Dipole acceleration power spectrum near the 85th harmonic obtained from the quantum model with t' set to nt_o where $n = 1, 2, 3, 4$ in (a), (b), (c), (d), respectively. 51

2.15 Shown in (a) is the amplitude of the 55th harmonic dipole acceleration component. Shown in (b) are the phases of the corresponding Pre-3.17 and Post-3.17 components. The solid lines denote results from the semi-classical model and the dashed lines denote the results from the quantum model. 52

2.16 The accumulated phase $S(t_q)$ and the recombination phase $q\omega_o t_q$ for the 55th harmonic Pre-3.17 and Post-3.17 components. 54

2.17 Phase of the Pre-3.17 and Post-3.17 55th harmonic dipole acceleration components. The circles, solid lines and dashed lines denote the results obtained respectively from Eqn. (2.61), the semi-classical model and the quantum model. 55

2.18 Spatial profiles of the driving intensity, I_1, the electron density, n_e, and the 55th harmonic intensity, I_{55}, recorded at $t = 283$ fs, 566 fs, 906 fs and 1586 fs. Direction of propagation is in the positive z direction. The medium has a background density of $n_o = 500$ torr. 63

2.19 Temporal and spectral profiles of the 55th harmonic intensity recorded at $z = 5$ μm, 100 μm, 200 μm, and 400 μm. The dashed lines denote the temporal electron density profiles recorded at these locations. . . 65

2.20 Temporal and spectral profiles of the 85th harmonic intensity recorded at $z = 1$ μm, 5 μm, 10 μm, and 20 μm. The dashed lines denote the temporal electron density profiles recorded at these locations 66

2.21 The energy of the 55th and 5th harmonics. The circles denote the discrete locations at which the harmonic energy is calculated. 67

2.22 Temporal profiles of the 55th harmonic intensity at $z = 200$ μm as obtained by (a) analytical and (b) simulation calculations. 71

2.23 Temporal profiles of the 85th harmonic intensity at $z = 200\ \mu$m as obtained by (a) analytical and (b) simulation calculations. 72

3.1 (a) Dipole acceleration power spectrum obtained for a 150 fs fundamental pulse interacting with neon. The fundamental pulse has a peak intensity of 1.5×10^{15} W/cm^2 and a wavelength of 400 nm. (b) Dipole acceleration power spectrum obtained for the mixing of a CW control field with the same fundamental pulse used in (a). The control field has a wavelength of 10400 nm and an amplitude equal to 0.070 of the fundamental pulse peak amplitude. 81

3.2 Dipole acceleration power spectra near the $26\omega_o - \omega_c$ mixed line obtained for the mixing of the same fundamental pulse used in Figure 3.1 and a CW control field with different amplitudes. E_{co} is the amplitude of the control field and E_{1o} is the peak amplitude of the fundamental pulse. 82

3.3 Energy of the $25\omega_o$, $26\omega_o - \omega_c$ and $26\omega_o - 3\omega_c$ dipole acceleration components. 83

3.4 (a) The normalized fundamental intensity and the ionization probability calculated in the absence of the control field. (b) The normalized control field profile. (c) Temporal profiles of the 25th harmonic at $E_{co} = 0$, the $26\omega_o - \omega_c$ component at $E_{co} = 0.025\ E_{1o}$ and the the $26\omega_o - 3\omega_c$ component at $E_{co} = 0.065\ E_{1o}$. These fields are normalized with respect to the peak 25th harmonic amplitude. 85

3.5 (a) Phase (in rad) of the 25th harmonic dipole component in the absence of the control field. (b) and (c) Phases of the $26\omega_o - \omega_c$ and $26\omega_o - 3\omega_c$ components at two different values of E_c. 86

3.6 The time-integrated energy of the 25th harmonic pulse. The values of the harmonic energy have been calculated at discrete locations as indicated by the circles. 90

3.7 The temporal profiles of the 25th harmonic recorded at different locations. Also plotted are the normalized fundamental intensity and the electron density. The electron density has a maximum value of 50 torr corresponding to 100% ionization of the gas. 91

3.8 Spectral profiles of the near-26 mixed field recorded at different locations in the medium. 93

3.9 Time integrated energy of the near-26th mixed field and the 25th harmonic when there is no control field. The energy is normalized with respect to the maximum 25th harmonic energy. 94

3.10 Temporal profiles of the low frequency control field near the ionization front recorded at different locations in the medium. 95

3.11 Temporal profiles of the $26\omega_o - \omega_c$ sub-band component recorded at different locations in the medium. Also shown are the normalized fundamental intensity and electron density. 96

3.12 The control field frequency shift at different locations in the medium as obtained from the numerical simulation (solid lines) and from the SVE analysis (dashed lines) 100

3.13 Shown on the left is the control phase as obtained from the numerical simulation (solid lines) and from the SVE analysis (dotted lines). Shown on the right is the deviation from the SVE phase. 101

3.14 Energy conversion of the near-26 mixed field generated by the mixing of the same 400nm fundamental field and a 3500nm control field with an initial amplitude equal to $0.07E_{1o}$. 103

4.1 Ground state population for helium as calculated from the average ADK ionization rate for a Gaussian laser pulse with different FWHM durations. Plotted is the ground state population versus the *rising* portion of the laser pulse. The laser has a wavelength of 750 nm and a peak intensity of 2×10^{15}W/cm^2. 106

4.2 Dipole acceleration power spectra for a 750nm, 2×10^{15}W/cm^2 laser pulse interacting with helium. The driving pulse durations are (a) 5 fs and (b) 200 fs. The spectra have been normalized with respect to the energy of the driving pulse. 108
4.3 The temporal profiles of the incident electric field, $\underline{E}_1$, the ionization probability, P, and the intensity envelope of the dipole acceleration, I_h, as seen through a filter which only allows frequency components above $\omega/\omega_o = 210$ to pass through. Here, E_o is the maximum incident field strength corresponding to an intensity of 2×10^{15}W/cm^2, $t_o = 2.5$ fs is the laser's fundamental cycle. The interacting medium is helium. . . 109
4.4 Spectral profiles of the induced harmonic field generated by a 750 nm, 5 fs, 2×10^{15}W/cm^2 incident laser field interacting with 500 torr of helium. The spectral profiles are shown near the cutoff region as a function of propagation distance. 113
4.5 Peak amplitude of the induced field as function of propagation distance. The induced field has been spectrally filtered to contain only frequency components above $\omega/\omega_o = 210$ 114
4.6 Temporal profiles recorded at $z = 20\ \mu$m of the incident electric field, $\underline{E}_1$, the electron density divided by the critical density for the fundamental field, n_e/n_c, and the amplitude envelope of the induced field as seen through a filter which only allows frequency components above $\omega/\omega_o = 210$ to pass through. Here, E_o is the maximum incident field strength corresponding to an intensity of 2×10^{15}W/cm^2 and $t_o = 2.5$ fs is the laser's fundamental cycle. The interacting medium is helium. . 115
4.7 Magnitude of the Fourier transformed dipole velocity calculated at different locations in the medium. 117
4.8 Phase of several frequency components near the cutoff region of the Fourier transformed dipole velocity as function of z'. 118

4.9 The amplitude and phase of the complex fundamental envelope in the retarded time frame recorded at various locations in the medium. E_o and t_o are respectively the initial peak field amplitude at $z = 0$ and the fundamental cycle. The dotted lines denote the phase calculated from the slowly varying envelope approximation. 121

4.10 The phase and amplitude of the complex fundamental envelope in the retarded time frame recorded at $z = 16$ μm in the medium. E_o and t_o are respectively the initial peak field amplitude at $z = 0$ and the fundamental cycle. The solid lines denote results obtained from the semi-analytical calculations and the dotted lines denote results from numerical solution to the wave equation 122

4.11 Change in cutoff frequency as predicted from the cutoff law. Here the change in the fundamental's ponderomotive potential is assumed to be due to the average frequency shift and the decrease in the peak intensity in the interval where the responsible electrons are ionized and recombine. 123

4.12 Phase of the ω_h / ω_o frequency component. The circles denote the phase obtained from the numerical simulation. The solid line represent the phase obtained from the semi-analytical analysis. The dashed lines denote the two contributions from the semi-analytical analysis. 127

4.13 Peak intensities of the soft-x-ray attosecond pulse (solid line) and the 201st harmonic generated by a 200 fs incident laser pulse (dashed line). 128

5.1 (a) and (b) Spatial profiles of the incident laser beam with a Rayleigh range of 5 mm and the electron density recorded near $z = 200$ μm. (c) The peak axial intensity recorded at various locations in the medium (solid line) and that calculated from Eqn. (5.3) (dashed line). 133

5.2 (a) and (b) Spatial profiles of the incident laser beam with a Rayleigh range of 20 mm and the electron density recorded near $z = 200$ μm. (c) The peak axial intensity recorded at various locations in the medium (solid line) and that calculated from Eqn. (5.3) (dashed line). 135

5.3 (a) and (b) On axis spatial profiles of the incident laser beam with a Rayleigh range of 20 mm and the electron density recorded near $z = 200$ μm. (c) On axis phase of the laser beam recorded at the same location. The solid line denotes the phase obtained from the numerical simulation while the circles denote the phase calculated from the WKB formula: $-(1/2)k_o z(n_e/n_c)$. 136

B.1 The computation grid and the moving frame. Z_t and T_t are respectively the total simulation length and time; Z_p and T_p are respectively the spatial and temporal extend of the moving frame; and $k_l\Delta z$ and $k_r\Delta z$ are respectively the left and right spatial boundaries of the moving frame. The solid circles denote the grid points near the $(j+1)\Delta t$ time step. 158

Chapter 1

Introduction

Advances in laser technology have made possible the production of very intense optical laser pulses with focussed intensities up to 10^{17} W/cm^2 and with ultra-short durations ranging from a few femtoseconds to a few hundred femtoseconds. One of the most important applications of these lasers is the study of intense field laser-atom interaction where the laser's electric field strength is comparable to the intra-atomic field strength which binds the nucleus and the electrons together. Many interesting phenomena have been experimentally observed as a results of these studies [1]. Among them are above threshold ionization, multiphoton ionization and tunnel ionization. Besides these, an optical process which converts the incident laser light into much higher frequency components has also stirred a lot of excitement in the scientific community.

When low density ($\approx$ 100 torr) atomic gases such as neon and argon are exposed to an intense ($\approx 10^{15}$ W/cm^2), short duration ($\approx$ 150 fs to 1 ps) laser pulse, the output radiation has been found to contain coherent frequency components which are odd harmonics of the incident laser field [2]. The highest harmonic components have been observed in the extreme-ultraviolet (XUV) and soft-x-ray spectral regions. This process has been commonly referred to as high harmonic generation (HHG) and is expected to be a useful source of short wavelength coherent radiation.

Interest in the development of high brightness coherent XUV and soft x-ray sources has been immense. This can be partly seen from the tremendous effort invested in the development of x-ray lasers and synchrotrons in the past decade. Some of the proposed applications of these sources include [3]: Electron Spectroscopy for Chemical Analysis (ESCA) which studies the elemental composition and chemical state of the surface of a material by photoionizing the core electrons and analyzing their kinetic energy distribution; X-Ray Microscopy which uses x-rays to resolve very small structure of living biological specimens; and X-Ray Holography which proposes to use coherent x-rays to take three dimensional holographic images of living cells. For microscopic and holographic applications, the desired x-ray wavelength range is between 2.3 nm and 4.4 nm, which has been referred to as the "water-window". In this wavelength range, carbon-containing biological objects absorb radiation efficiently whereas water is relatively transparent. A radiation source which can produce x-rays in the water-window will allow for very high contrast imaging of the biological objects with respect to their surrounding.

To date, harmonics have been reported with wavelengths as short as 7 nm [4, 5, 6, 7, 8] and energies as high as a few nJ with an energy conversion efficiency of about 10^{-7} [9]. These figures indicate that HHG can be a useful source of XUV or soft x-ray radiation. A number of HHG applications have already been investigated: Haight and co-workers have used harmonic radiation to perform spectroscopic analysis of solid-state surfaces [10, 11, 12]; Balcou *et al* have used high harmonics to measure the relative photo-ionization cross section of a number of rare gases [13]; and Larsson *et al* have used high harmonics to study spectroscopy of helium [14].

When compared with other coherent XUV and soft-x-ray sources such as synchrotrons and x-ray lasers, HHG is anticipated to have a number of distinct advantages according to current HHG experimental and theoretical evidence. These include short pulse duration, high spectral brightness, broad spectral tunability and compact experimental setup. For example, one of the studies to be presented in this thesis predicts that harmonic pulses can have durations of as short as several femtoseconds and that it may be possible to generate coherent soft-x-ray pulses with durations of only a few hundred attoseconds. These pulse durations are at least two orders of magnitude shorter than the picosecond XUV or soft-x-ray pulses generated by synchrotrons and x-ray lasers [15]. The *peak* spectral brightness of high harmonic pulses in the XUV range is estimated to be greater than 10^{23} photons mm^{-2} mrad^{-2} s^{-1} [16] which is many times greater than that of existing synchrotron sources. In addition, since the frequency of the incident lasers can be easily adjusted with existing laser technology, the frequencies of the resulting harmonics are thought to be tunable. This can be potentially a great advantage over x-ray lasers where the lasing wavelength is fixed by the transition levels. Finally, most HHG experiments use compact solid state lasers, such as the Ti:Sapphire lasers, to generate the harmonics. The trend toward smaller and smaller sizes of these lasers will make HHG a potentially "table-top" size device. This represents a great advantage over current synchrotron sources which are laboratory-size devices.

Although a basic understanding of HHG has been obtained through both experimental and theoretical investigations, a number of important and practical issues remain to be investigated. These include the spectral and temporal characteristics of the high harmonic radiation, methods of further improving the energy conversion efficiency and schemes to increase the shortest harmonic wavelength obtainable. In this thesis research, a theoretical investigation has been undertaken to address some of these issues. These studies are detailed in the following chapters. In the remainder of this chapter, an overview of HHG experimental observations and the current theoretical understanding is provided to give a general understanding of the HHG process. This is then followed by a detailed discussion of the scope of the thesis investigation.

1.1 General HHG Experimental Observations

HHG experiments are performed by focussing an intense, linearly polarized [1] laser pulse onto a low density gas target. This is illustrated schematically in Figure 1.1.

---

[1] For elliptically polarized lasers, strengths of the high harmonic radiation have been observed to decrease significantly. An explanation is given in the next section.

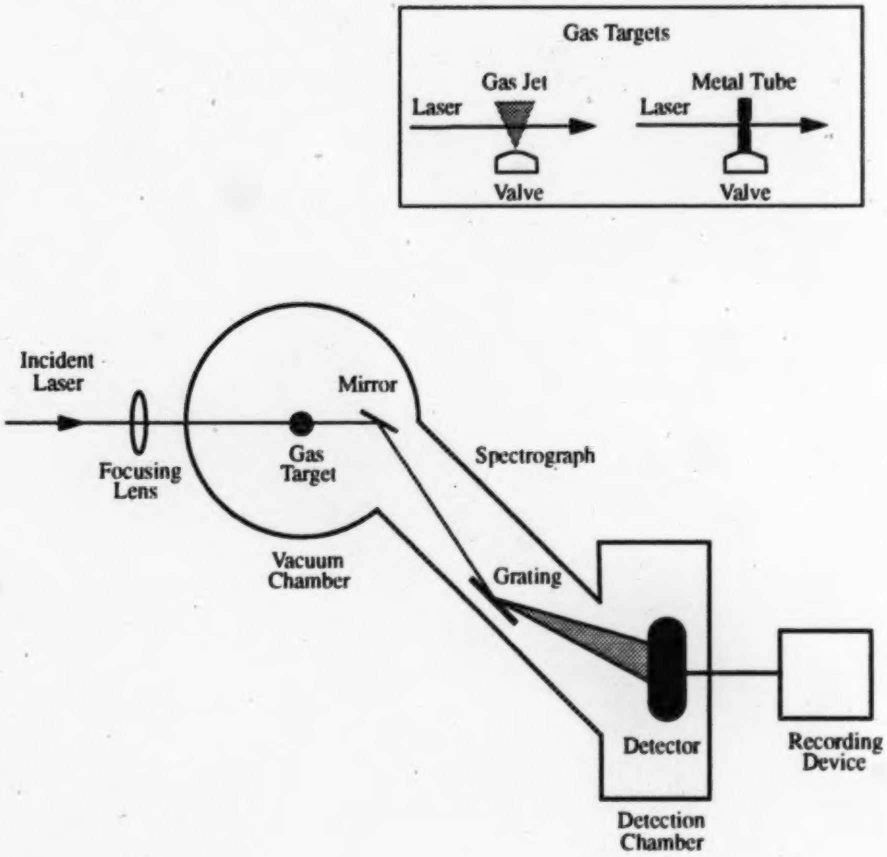
Gas Targets
Gas Jet
Laser
Valve
Metal Tube
Laser
Valve
Incident Laser
Focusing Lens
Gas Target
Mirror
Spectrograph
Vacuum Chamber
Grating
Detector
Recording Device
Detection Chamber

Figure 1.1: A typical schematic HHG experimental configuration.

Typical lasers used in current experiments have wavelengths ranging from 250 nm to 1000 nm and durations in the femtosecond range. The vacuum focussed intensities of these lasers vary from 10^{14} W/cm^2 to 10^{15} W/cm^2 . The gas target is placed inside a vacuum and is in the form of a gas jet or a gas slab confined by a squeezed metal tube (see inset in Figure 1.1). In either case, the gas is allowed into the vacuum chamber from a gas reservoir by opening a pulsed valve prior to the arrival of the laser pulse. The gas medium is usually one of the five noble gases and the target density ranges from a few torr to a few hundred torr. The output radiation emerging from the gas target is directed into a spectrograph and is spectrally dispersed by a reflection grating. Finally, the harmonic signal is detected by an XUV or soft-x-ray detector.

Experimental results of HHG are usually presented in the form of an energy spectrum which depicts the energy distribution of the various detected harmonic components. A typical HHG spectrum is shown in Figure 1.2. Here, two general characteristics common to most experimental spectra are seen. First, only odd harmonics are observed. Secondly, for sufficiently high laser intensities, there exists a "plateau" region in the spectrum where the harmonic strengths are relatively constant. This region is preceded by a rapid fall-off of the first few harmonics and ends with a "cut-off" beyond which harmonic signals decrease very rapidly again. The laser intensities at which harmonic plateaus are formed generally increase from media with lower ionization potentials (e.g. xenon) to media with higher ionization potentials (e.g. helium). Typical intensities where harmonic plateaus occur range from 10^{13} W/cm^2 to 10^{16} W/cm^2.

1.2 Theoretical Investigation

As is common in nonlinear optical studies [17], the theoretical interpretation of HHG experimental results involves two steps. The first step is to determine the polarization of the medium. This is achieved through *single atom analysis* which calculates the microscopic electric dipole moment induced by the laser field. The second step is to

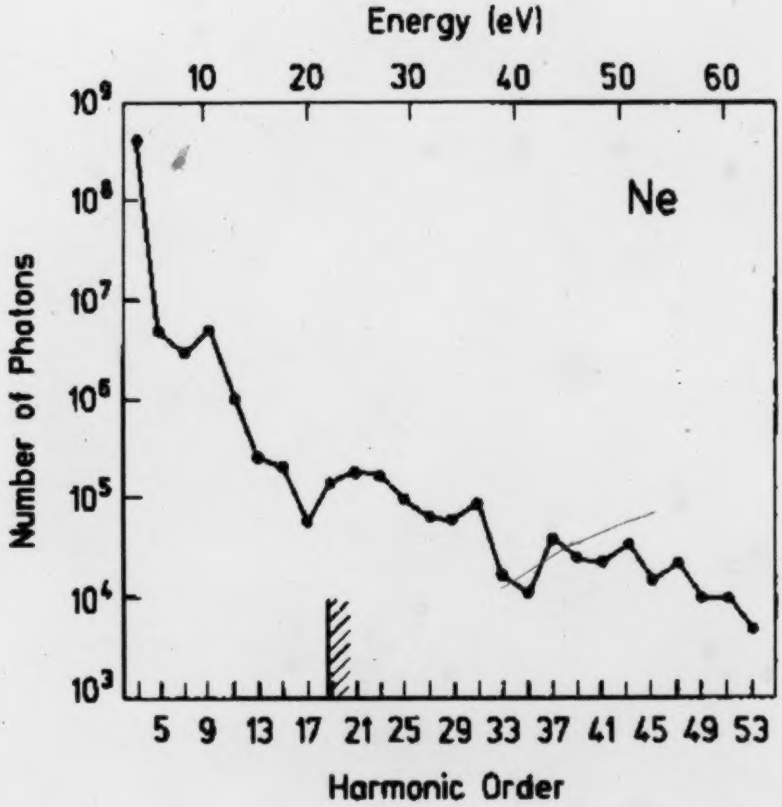

Figure 1.2: Harmonic spectrum obtained from a 1053 nm, 30 mJ, 1 ps, Nd-glass laser in neon (from Ref. [2]).

determine the macroscopic electromagnetic field emerging from the medium. This is achieved through ***propagation analysis*** which seeks solutions to Maxwell's equations using the polarization obtained from single atom analysis. Physically, the first theoretical step can be interpreted as an examination of how individual atoms respond to the driving laser field while the second step is an investigation of how the resulting harmonic field propagates in the macroscopic medium involving many atoms. These two steps are discussed in greater detail below.

1.2.1 Single atom analysis

The source for any radiation scattered from a medium is its induced polarization which is equal to the induced dipole moment per unit volume:

$$\vec{P} = n_o\vec{d} \tag{1.1}$$

Here, n_o is the number density of the medium and $\vec{d}$ is the atomic electric dipole moment induced by an external laser field. In HHG analysis, the dipole moment is obtained from quantum mechanical analysis and is calculated as the expectation value of the dipole operator $e\vec{r}$ for a single atom:

$$\vec{d}(t) = <\Psi|e\vec{r}|\Psi> \tag{1.2}$$

Here, Ψ is the wave function of the atomic system in the presence of the laser field and is a solution to the relevant Schrödinger equation describing the laser-atom interaction.

Various methods have been used to determine the atomic dipole moment responsible for HHG [2]. Specifically, the dipole moment for realistic atomic systems has been calculated and extensively studied by Kulander and co-workers [18]. Assuming that the atom can be treated as a single electron moving in an effective electrostatic potential, they determine the atomic wave function by direct numerical integration of the time-dependent Schrödinger equation:

$$i\frac{\partial}{\partial t}\Psi = \left[-\frac{\hbar^2}{2m}\nabla^2 + V(\vec{r}) - exE\right]\Psi \tag{1.3}$$

Here, E is an external driving electric field linearly polarized in the x direction and V is the effective electrostatic potential, m is the electron mass and e is the electron charge. The calculated single-atom spectra, which is evaluated as the square of the Fourier transform of the time-dependent dipole moment, possess many features of the experimental spectra such as the rapid fall-off of the first harmonics, the constant intensity plateau region, and the sharp harmonic cut-off. An example is shown in Figure 1.3. In addition, when propagation effects are taken into consideration, good quantitative agreement with experimental results have also been obtained [21, 22, 9]. However, despite the success of these theoretical results, such numerical solutions provide a less than complete physical insight into the underlying process.

A physical understanding of the HHG atomic response has been obtained following a proposed scaling law for the single-atom HHG spectra. In [23], by using the numerical methods employed by Kulander *et al* [18], Krause *et al* observe that the cut-off harmonic (ω_{cutoff}) for many atomic systems can be predicted quite accurately by:

$$\hbar\omega_{\text{cutoff}} \approx I_p + 3U_p \tag{1.4}$$

where I_p is the ionization potential of the atom and $U_p = (1/4)(e^2E^2)/(m\omega^2)$ is the laser's ponderomotive potential and ω is the laser's frequency. This scaling law seems to be supported by many experimental results [24, 4, 5]. Following this observation, a physical interpretation of the cut-off law (Eqn. (1.4)) has been proposed by Corkum [25]. It is suggested that HHG is a result of the following process. Firstly, the valence electrons of the atoms are tunnel or field ionized [26, 27, 28, 29] with zero initial velocity [27, 31]. Secondly, these electrons are accelerated by the laser's electric field and their motion is described by Newton's laws of motion [2]. Finally, harmonics are emitted by those electrons which return to the vicinity of the parent atom and recombine to the ground state. A similar interpretation of the HHG process has also been given by Schafer *et al* [30].

---

[2] A more detailed discussion of tunnel ionization and the classical motion of the resulting ionized electrons is given in Chapter 2.

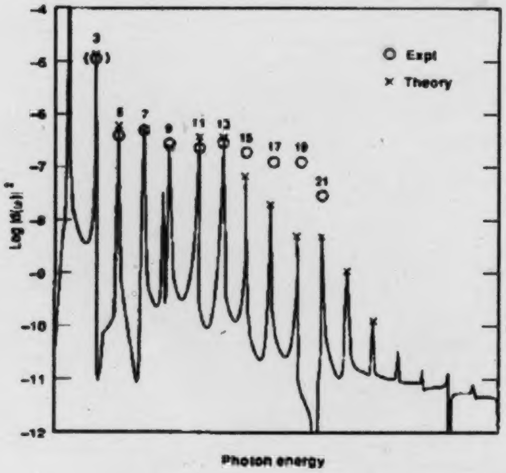

Figure 1.3: Calculated single atom harmonic spectrum for a 1064 nm, 3×10^{13} W/cm^2 laser interacting with xenon from Ref. [19]. Superimposed are the experimental results from Ref. [20]. (The spectra have been adjusted in Ref. [19] to agree at the 7th harmonic.)

From the above semi-classical [3] model, the cut-off law can be readily understood from energy conservation considerations [25, 30]. For an electron released with zero initial velocity from an atom and then accelerated according to Newton's law of motion by an oscillating electric field with a constant intensity, it can be easily shown from numerical calculations that the maximum kinetic energy the electron can have when re-visiting the parent atom is equal to 3.17 U_p and this occurs during the electron's first re-encounter with the atom [4]. Consequently, when the re-colliding electron does recombine with the atom, the maximum energy of the emitted photon must be equal to the maximum acquired kinetic energy of the electron, 3.17 U_p, plus the ionization potential of the atom, I_p. Hence, $\hbar\omega_{\text{cutoff}} = I_p + 3.17\ U_p$.

The semi-classical model has also been able to explain a second general observation from the simulation results of Krause *et al* [23], that is, the strength of the single-atom harmonic plateau is proportional to the medium's ionization rate. According to the semi-classical model, since harmonics are generated by the spontaneous recombination of tunnel *ionized* electrons, the number of harmonic photons produced is proportional to the number of electrons ionized. Therefore, the harmonic intensity will be proportional to the ionization rate. In Ref. [25], Corkum attempts to calculate the dipole moment by phenomenologically constructing the atomic wave function based on the semi-classical approach [5] where ionization is described by tunnel theories [29]. He shows that the resulting harmonic spectrum is indeed proportional to the ionization rate and the height of the calculated harmonic plateau agrees very well with that observed from the numerical calculations by Krause *et al* [23].

The harmonic nature of the emitted radiation can also be understood from this model. Assuming the incident laser has a slowly varying intensity envelope, the ionized electrons will be accelerated and pass the parent atom the same way during each laser cycle. Therefore, any radiation that is emitted by the recombination of these electrons to the ground state will be at a harmonic of the laser frequency. As will be discussed in the next chapter, the observation of only odd harmonics can also be explained by this model since the corresponding dipole moment reverses sign in successive one-half laser periods.

---

[3] The model is semi-classical in that ionization and recombination of the electrons are described quantum mechanically while the electrons' motion in the laser field is described classically

[4] This will be shown in Chapter 2

[5] A more detailed discussion of this model will be given in Chapter 2

After the proposal of the semi-classical model, a more rigorous quantum mechanical analysis has been carried out to justify the semi-classical hypothesis. In Ref. [32], Lewenstein *et al* obtain a closed form solution to the three dimensional Schrödinger equation by ignoring contributions from all bound states except the ground state to the system wavefunction and by neglecting the effect of the atomic potential on the continuum states. These assumptions are valid in the tunnelling regime [27] where the electrons are in the presence of a very strong laser field during ionization and recombination. Analysis of the resulting dipole moment indicates that the main contribution to the emission of a particular harmonic indeed comes from the electrons which, after having tunneled through the atomic potential barrier with zero initial velocity, follow a classical trajectory in the laser field and then return to the nucleus with a kinetic energy equal to the harmonic photon energy minus the atomic potential.

One immediate success of the Lewenstein model is its ability to explain quantitatively the dependence of HHG on the ellipticity of the incident laser light [33, 34]. From classical trajectory considerations, electrons with zero initial velocity can only re-collide with the parent atom when the accelerating laser field is linearly polarized. A very small ellipticity of the laser field will cause the electrons to drift away and miss the atomic nucleus. Consequently, no harmonics can be emitted. In quantum mechanics, the ionized electron is described by a wave function with a time-dependent spatial spread due to the small uncertainty of the electron's initial momentum when it is released from the atom [34]. Therefore, the ellipticity dependence is not as severe as in the classical case and is dependent on the spread of the electron wave function. Theoretical calculations of the harmonic ellipticity dependence obtained from the Lewenstein model, which is capable of describing the spread of the electron wave packet, show very good agreement with experimental results [33].

1.2.2 Propagation analysis

When the medium's polarization is determined, propagation analysis can be carried out to study HHG under more realistic experimental conditions. The general propagation modelling approach [2] is to solve the electromagnetic wave equation derived from Maxwell's equations:

$$\nabla^2 \underline{E} - \frac{1}{c^2}\frac{\partial^2 \underline{E}}{\partial t^2} = \frac{4\pi}{c^2}\frac{\partial^2 \underline{P}}{\partial t^2} \tag{1.5}$$

where $\underline{E}$ is the total electric field inside the medium, including the driving field as well as the generated harmonic fields and $\underline{P}$ is the medium polarization induced by $\underline{E}$ and is determined from single atom analysis.

Extensive propagation modelling of HHG in almost neutral media by a *focussed* laser beam has been done by L'Huillier and co-workers [2, 21, 22, 5, 35, 36]. By neglecting the depletion of the driving field and assuming that harmonics are generated by only the driving field, the wave equation (Eqn. (1.5)) is decomposed into a set of decoupled equations for the driving and harmonic fields. The resulting equations are solved in the two-dimensional paraxial and slowly varying envelope (SVE) approximations [2] using either integral or finite difference methods. The dipole models of Kulander *et al* [18] and Lewenstein *et al* [32] have been used in these propagation studies. For long duration ($\approx$ 1 ps) driving lasers, the calculated harmonic spectra show good quantitative agreement with experimental results.

For HHG from very short duration ($<$ 100 fs) lasers in a rapidly ionizing medium, the SVE approximation used by L'Huillier *et al* is no longer applicable. Recently, Rae and Burnett have developed a model to study HHG in this regime [37]. They numerically solve the fully time-dependent wave equation (Eqn. (1.5)) in the one-dimensional limit. Atomic response is consistently calculated by numerically integrating the Schrödinger equation for a one dimensional atom interacting with the total propagating electric field. Results from this investigation have provided some insight into the fast dynamical response of the HHG process under these conditions, although they cannot be compared directly to experimental results due to the one-dimensionality of the atomic modelling which ignores the important effect of the transverse spread of the electron wave function.

1.3 Scope of Thesis

To date, most experimental and theoretical work has concentrated on the understanding of the harmonic conversion efficiency and the location of the harmonic cut-off. Many experiments have been done to specifically study the strength and extent of the harmonic plateau under various conditions and many theoretical studies have been aimed at interpreting these experimental results. As a result, there are still many important issues which remain to be investigated.

In this thesis, a number of practical and interesting issues which have not been previously studied are examined. These include: (1) the temporal and spectral characteristics of the high harmonic emission; (2) the possibility of increasing harmonic conversion efficiency by high order difference frequency mixing; and (3) the generation of attosecond coherent x-ray pulses. These studies are organized in this thesis as follows:

Chapter 2 examines the spectral and temporal structure of the high harmonic emission generated under conditions which are typical of many current HHG experiments. Here, both single atom and propagation analyses are carried out. The single atomic response is obtained from the dipole models developed by Corkum [25] and Lewenstein *et al* [32]. These models are attractive to use not only because of their mathematical and computational simplicity but also because of their ability to predict experimental results and their agreement with other more rigorous theoretical calculations. The propagation analysis is conducted using a one-dimensional non-SVE propagation model where the polarization current is consistently calculated from the Corkum/Lewenstein model. The main features of this propagation model are that it uses the realistic dipole model developed by Corkum and Lewenstein and that it also allows the study of fast transient effects in HHG. Results from this study indicate that harmonic lines are strongly blueshifted and broadened under realistic experimental conditions and that these harmonics can have durations of only a few femtoseconds.

Chapter 3 investigates the possibility of increasing harmonic conversion efficiency by high order difference frequency mixing. Here, a proposed phase matching scheme is studied. In this scheme, a secondary low frequency, low intensity laser field is allowed to co-propagate with the high frequency high intensity driving laser field. Preliminary studies by others [38, 39, 40] suggest that the output harmonic field strength can be greatly increased. In this part of the thesis study, both the atomic and one-dimensional propagation models have been modified to allow for an additional laser field. Results from this investigation show that the conversion enhancement is not as promising as anticipated and the limitations of the proposed scheme are examined.

Chapter 4 explores the possibility of generating attosecond coherent x-ray pulses by using a driving laser with a duration of only a few optical cycles. Here, the atomic dipole moment of Lewenstein *et al* [32] is used. Single atom calculations predict that the odd harmonic structure usually associated with longer driving pulses no longer exists and the resulting dipole spectrum resembles a continuum spectrum. In propagation analysis, a different model has been developed to describe the propagation of the generated continuum spectrum. Results from this study indicate that attosecond soft-x-ray pulses can be quite efficiently generated from this process.

Chapter 5 addresses some two-dimensional issues which have been ignored in the previous studies in the thesis. Here, a two dimensional paraxial wave solver which has been developed by Rankin *et al* [41] has been used to study the propagation of the driving laser beam. The regime of validity of the previous one-dimension analysis is examined.

Finally, Chapter 6 summaries the findings and conclusions of this thesis investigation. Implications of the thesis results are also discussed.

Chapter 2

Spectral and Temporal Study of High Harmonic Generation

Experiments which investigate high harmonics have all been performed with pulsed lasers. Typical durations of these lasers range from a few picoseconds to just a few femtoseconds. Consequently, all observed harmonics are generated in a time varying environment and the harmonic radiation itself is also a time-dependent quantity. In spite of this fact, not many studies, either experimental or theoretical, have been done to examine the temporal behavior of the harmonic emission. Equally neglected are systematic studies of the spectral constitution of the harmonic emission which can have important implications in many HHG applications.

The objective of this study is to investigate the spectral and temporal characteristics of the high harmonic radiation. Here, harmonic spectral and temporal profiles are obtained and studied via single atom and one dimensional propagation modelling of the HHG process. In this chapter, a detailed description of this investigation [1] is given. Section 2.1 examines the single atom response. Here, the dipole models used in the calculations are described and the single atom harmonic spectral and temporal profiles are presented. Section 2.2 investigates propagation effects. Here, the dipole models used in single atom analysis are coupled to a one dimensional propagation model. Effects on the harmonic spectral and temporal profiles due to propagation are discussed. Finally, the chapter ends with a summary of findings and conclusions of this investigation.

---

[1] A version of this study has been published in Phys. Rev. A **52**, R4336 (1995), entitled "Spectral and temporal structure in high harmonic emission from ionizing atomic gases", by C. Kan, C . E. Capjack, R. Rankin and N. H. Burnett.

2.1 Single Atom Analysis

As discussed in Chapter 1, the first step in HHG modelling is to determine the dipole moment of the atomic system. Only when this quantity is determined can a more realistic propagation analysis be carried out. Physically, the second time derivative of the dipole moment, i.e. the dipole acceleration, is a measure of the scattered radiation emitted by a very dilute atomic gas.

In this study, three dipole models have been used. The first model is based on the HHG model developed by Corkum [25]. Here, the dipole moment is derived formally from a number of intuitive physical arguments. The second model is based on the mathematically rigorous HHG model developed by Lewenstein and co-workers [32]. As will be shown later, although these two models have a few physical and computational differences, they yield essentially the same results. The last model is based on the HHG process described by Brunel [42]. As will be shown later, this model predicts negligible high harmonic emission and is used here mainly to account for free electron induced dispersion in the propagation analysis.

As discussed in Chapter 1, essential in understanding these dipole models are two related processes: tunnel ionization and the classical dynamics of the tunnel ionized electrons in the laser field. Consequently, these processes will be discussed first. A description of the three dipole models will then follow.

2.1.1 Tunnel ionization

When an atom is exposed to a strong external d.c. electric field, there is a finite probability that the valence electron can be ionized from the atom [26]. The physical interpretation behind this process is that the external electric field acts to lower the effective potential as seen by the valence electron. Consequently, there is a finite probability that the electron can tunnel through the lowered potential barrier caused by the external d.c. field and become ionized. Such a process has been referred to as tunnel ionization.

In the case of a strong *low frequency* laser field, it has been shown [27] that if the laser cycle is long compared to the time needed for the electron to pass or tunnel through the effective potential barrier, ionization of the valence electron can also be described by the tunnelling process. Here, the lowered potential barrier is caused by the *instantaneous* value of the external electric field. Quantitatively, this condition is achieved when [27]:

$$\gamma \ll 1 \tag{2.1}$$

Here γ is the so-called Keldysh parameter given by:

$$\gamma \equiv \omega_o \;/\; \omega_t \tag{2.2}$$

where ω_o is the laser frequency and $\omega_t/2\pi$ is the inverse of the tunnelling time Δt_t. As discussed in Ref.[27], the tunnelling time is just the mean free time in which the electron tunnels through the lowered potential barrier and is given by:

$$\Delta t_t = \sqrt{2mI_p} \;/\; eE \tag{2.3}$$

where m and e are respectively the electronic mass and charge; I_p is the ionization potential of the atom; and E is the laser electric field strength.

For complex atoms, the tunnel ionization rate has been obtained by Ammosov, Delone and Krainov and is given by [29]:

$$R_t = \omega_a C^2_{n^*l^*} \frac{I_p}{2I_h} \left[2 \left(\frac{I_p}{I_h} \right)^{3/2} \frac{E_a}{|E|} \right]^{2n^*-1} \exp\left[-\frac{2}{3} \left(\frac{I_p}{I_h} \right)^{3/2} \frac{E_a}{|E|} \right] \tag{2.4}$$

Here ω_a is the atomic unit of frequency equal to 4.134×10^{16} s^{-1}; I_p is the ionization potential of the atom; I_h is the ionization potential of the hydrogen atom equal to

13.6 eV; E is the instantaneous electric field strength; E_a is the atomic unit of electric field equal to 0.514×10^{12} V/m; $n^* = Z/\sqrt{I_p/I_h}$ is the effective principle quantum number where Z is the charge of the atomic residue; $l^* = n^* - 1$ is the effective orbital quantum number; and $C_{n^*l^*}$ is a numerical constant equal to:

$$C^2_{n^*l^*} = \frac{2^{2n^*}}{n^*\Gamma(n^* + l^* + 1)\Gamma(n^* - l^*)} \tag{2.5}$$

where Γ is the gamma function. The ionization probability is determined by the rate equation [42]:

$$\frac{dP(t)}{dt} = R_t(1 - P(t)) \tag{2.6}$$

from which it can be readily shown that:

$$P(t) = 1 - \exp\left(-\int^{t} R_t dt''\right) \tag{2.7}$$

Shown in Figure 2.1 are the tunnel ionization rate and the tunnel ionization probability calculated for an electric field with a peak intensity of 5×10^{14} W/cm^2 interacting with a neon atom for two laser cycles. It is seen that due to its dependence on E, the ionization rate becomes significant only near the peaks of $|E|$. This results in a step-like ionization probability profile as shown in Figure 2.1(c).

It should be noted that the tunnel ionization rate given by Eqn. (2.4) is only valid for $|E| \ll E_a$ [45]. Specifically, it has been proposed [46] that when $|E|$ reaches a certain critical strength, E_{cr}, the ionization probability immediately becomes unity. The critical field strength is just the external electric field strength which is needed to lower the atomic potential barrier by an amount equal to the atomic ionization potential such that the bound electron can escape freely from the atom without tunnelling. This critical field strength (in atomic units) is given by[46]:

$$E_{cr} = \frac{(I_p/I_h)^2}{16Z} \tag{2.8}$$

It should also be noted that in the case where $\gamma > 1$, ionization is described by multiphoton ionization [27] in which the bound electron is ionized by simultaneously

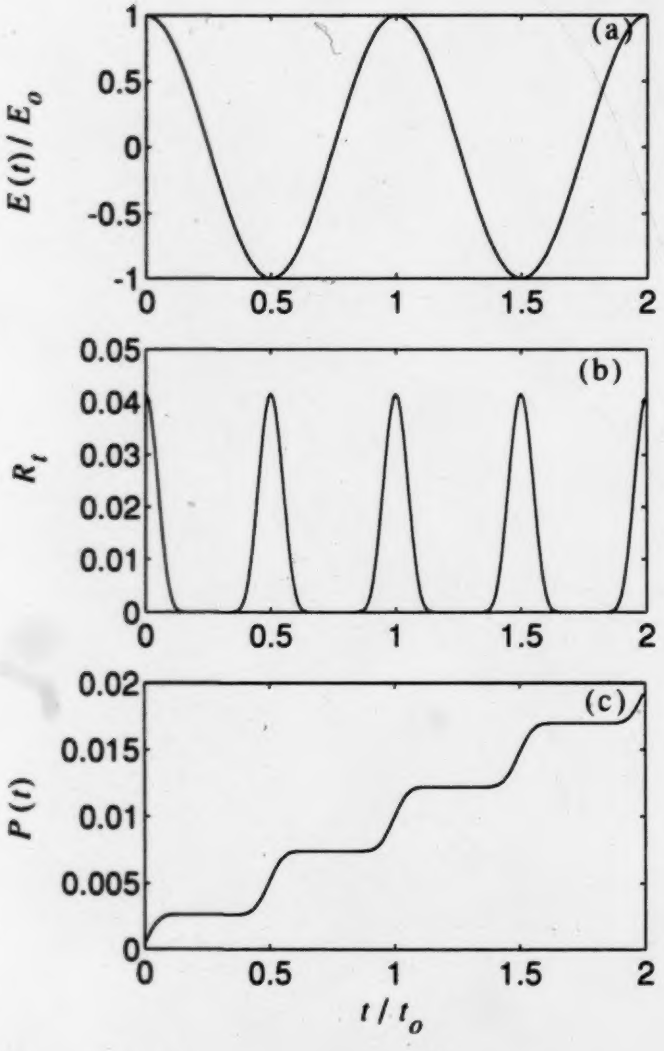

Figure 2.1: (a) The ionizing electric field corresponding to a peak intensity of 5×10^{14} W/cm^2. (b) The tunnel ionization rate for a neon atom in units of t_o^{-1} where the laser period t_o is equal to 2.5 fs. (c) The ionization probability.

absorbing a number of the incident laser's photons. In this thesis investigation, studies are conducted only in the regime where tunnel ionization is the dominant ionization mechanism.

2.1.2 Classical motion of tunnel ionized electrons

After electrons have been ionized in a laser field, they are free from the influence of the atomic potential and their motion is determined by the laser electric field [2]. In classical mechanics, the motion of a free electron in an electric field is determined by:

$$a(t) = \frac{-e}{m}E(t) \tag{2.9}$$

where a is the acceleration of the electron; e and m are respectively the electronic charge and mass; and E is the laser electric field strength which is assumed to be linearly polarized. If the initial velocity and position of the electron are known at the time of release or ionization from the atom, Eqn. (2.9) can be integrated to give the velocity and displacement of the electron at all later times.

The initial velocity of a tunnel ionized electron has been shown theoretically to be near zero [27] within a small uncertainty. This uncertainty is due to the fact that there is an uncertainty in time at which the bound electron tunnels through the effective potential barrier and becomes ionized. From the uncertainty principle, there is also an uncertainty in initial energy associated with the ionized electron. Using the energy-time uncertainty relation, it has been shown [43] that the uncertainty in the initial velocity is given by:

$$|\Delta v| = \sqrt{\frac{2\hbar}{m\frac{\sqrt{2mI_p}}{eE}}} \tag{2.10}$$

For strong laser fields (e.g. $I_o > 10^{15}$ W/cm^2), it can be shown that this small velocity uncertainty has little effect on the motion of the electron in the direction of the laser's electric field. However, in the direction perpendicular to the electric field, this uncertainty can cause a net drift in the electron trajectory. In quantum mechanical analysis, such a drift corresponds to spreading of the electron wavefunction. This will be further discussed below. By neglecting this small initial velocity uncertainty and assuming that $E(t) = E_o \cos(\omega_o t)$, the velocity of a tunnel ionized electron in the direction of the electric field can be calculated as:

---

[2] This is true provided that the electrons' velocities are much less than the speed of light, as they are in the cases studied here. Therefore, the magnetic component of the Lorentz force can therefore be neglected.

$$v(t) = \frac{-eE_o}{m\omega_o}\left[\sin(\omega_o t) - \sin(\omega_o t')\right] \tag{2.11}$$

where t' is the electron release time. The initial position of the tunnel ionized electron can be estimated from the width of the effective potential barrier due to the sum of the atomic Coulomb field and the external laser field [44] and is equal to a few Bohr radii ($a_B = 5.2918 \times 10^{-11}$ m) for the studies conducted in this thesis. For electron motion in the strong laser fields studied here, it can be shown that this small initial displacement has negligible effect on the electron trajectory. Consequently, the initial position of the electron can be assumed zero and the displacement of the tunnel ionized electron can be calculated as:

$$x(t) = \frac{-eE_o}{m\omega_o^2}\left[-\cos(\omega_o t) + \cos(\omega_o t') - \sin(\omega_o t')(\omega_o t - \omega_o t')\right] \tag{2.12}$$

The electron trajectories as obtained From Eqn. (2.12) for different release (ionization) times are shown in Figure 2.2. It is seen that an electron ionized during the time intervals $0.25 < t'/t_o < 0.5$ and $0.75 < t'/t_o < 1.0$ where t_o is the laser cycle cannot revisit or re-collide with the parent atom. An electron ionized during these intervals simply drifts away from the parent atom. However, an electron ionized between $0.5 < t'/t_o < 0.75$ will have its first re-collision with the parent atom between $0.75 < t/t_o < 1.5$ while an electron ionized between $1.0 < t'/t_o < 1.25$ will have its first re-collision between $1.25 < t/t_o < 2.0$. From Figure 2.2, it is also seen that there is also a chance that the electron can once again re-collide with the parent atom *after* the first re-collision.

Figure 2.3 shows the re-collision velocity and kinetic energy of the electron during its first re-encounter with the parent atom. In Figure 2.3(b), the negative re-collision

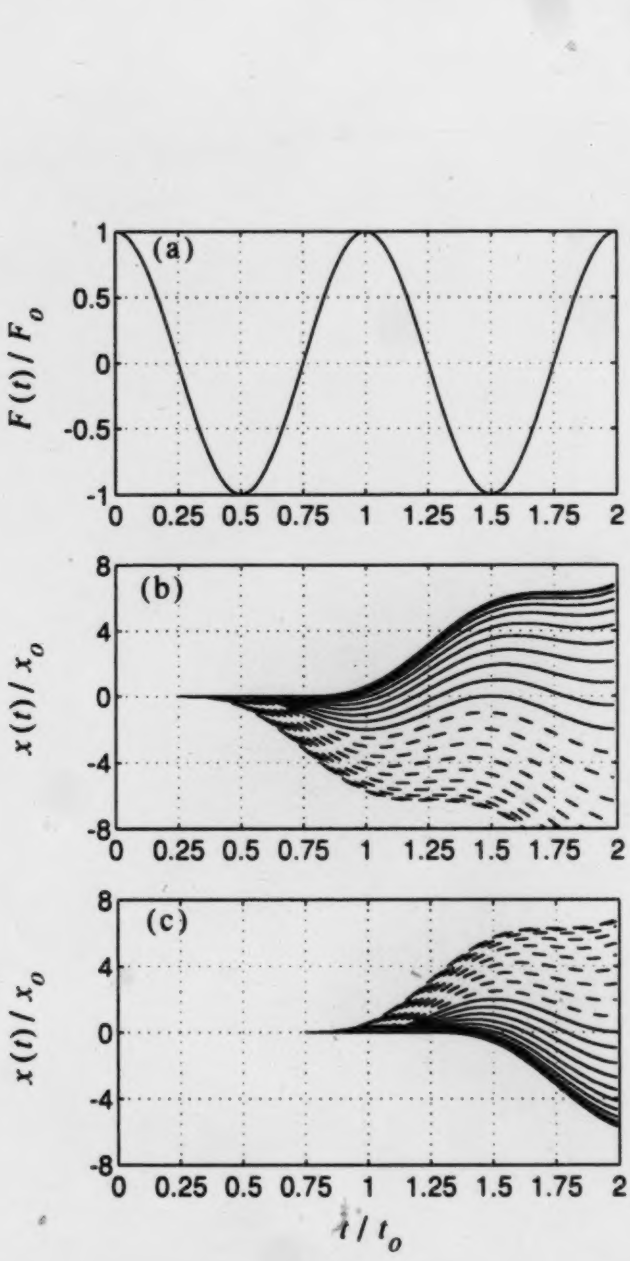

Figure 2.2: (a) The force acting on the electron due to E. (b) The electron trajectories which have negative initial displacements. (c) The electron trajectories which have positive initial displacements. The dashed lines denote those trajectories which will not cross the x-axis again. $F_o = -(e/m)E_o$ and $x_o = -(e/m)(E_o/\omega_o^2)$

velocity corresponds to an electron ionized between $0.5 < t'/t_o < 0.75$ (Figure 2.2(b)) while the positive re-collision velocity corresponds to an electron ionized between $1.0 < t'/t_o < 1.25$ (Figure 2.2(b)). The corresponding re-collision kinetic energy is shown in Figure 2.3(c). As mentioned in Chapter 1, the maximum kinetic energy attainable by such an electron is about 3.17 U_p where $U_p = (1/4)(e^2E^2)/(m\omega_o^2)$ is the driving laser field's ponderomotive energy. It is seen that for an energy below this maximum, there can be four times at which an electron can have the same re-collision energy.

2.1.3 The semi-classical dipole model

This model is based on the dipole model developed by Corkum [25] who proposes that HHG is a result of the spontaneous recombination to the ground state of the tunnel ionized electrons which have been accelerated by the laser's electric field and are now re-colliding with the parent atom. In the following discussion, the original model is described first. This is followed by a description of the extended model which is used in this investigation.

The Corkum model

In Ref. [25], the dipole moment is obtained by assuming that the wavefunction of the atomic system in the presence of an external electric field can be written as:

$$\psi = \psi_g + \psi_c \tag{2.13}$$

where ψ_g represents the ground state wavefunction of the atom and ψ_c is the continuum wavefunction representing the recombining electrons. The dipole expectation is then given by:

$$\begin{aligned} d &= <\psi|ex|\psi> \\ &= <\psi_g|ex|\psi_g> + <\psi_g|ex|\psi_c> + <\psi_c|ex|\psi_g> + <\psi_c|ex|\psi_c> \end{aligned} \tag{2.14}$$

In order to evaluate the dipole moment, a number of considerations and assumptions are made. Firstly, it is assumed that ionization is small and depletion of the

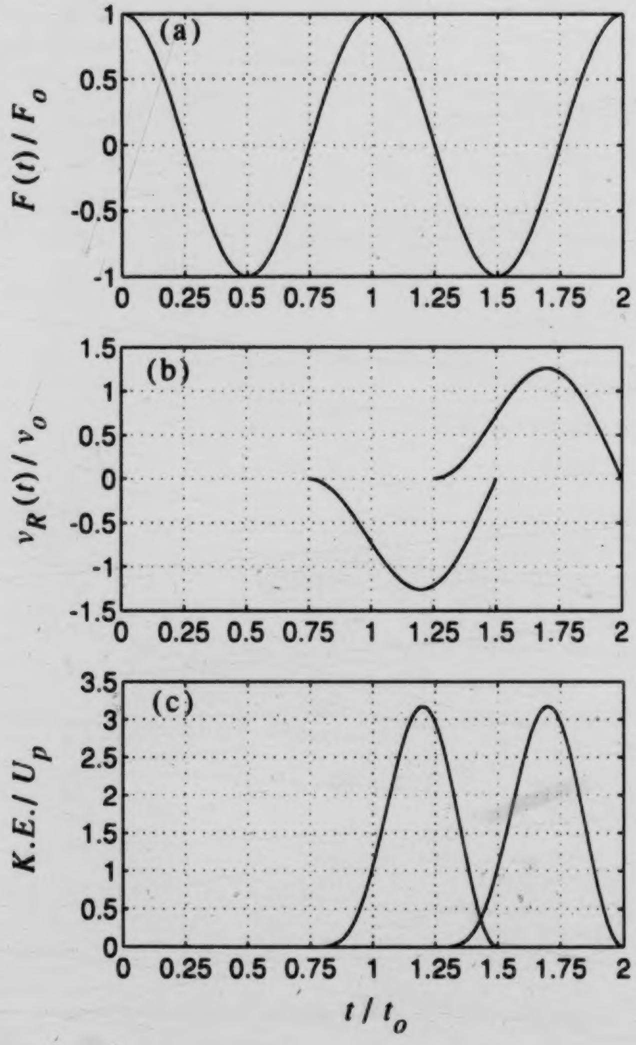

Figure 2.3: (a) The force acting on the electron due to E. (b) The velocity of the electron during its first re-collision with the parent atom. (c) The kinetic energy of the electron during its first re-collision with the parent atom. $F_o = -(e/m)E_o$, $v_o = -(e/m)(E_o/\omega_o)$ and $U_p = (1/4)(e^2E^2)/(m\omega_o^2)$

ground state wavefunction can be neglected. Therefore, the ground state wavefunction can be modeled as the steady state ground state wavefunction of the atomic system. Furthermore, it is assumed that this wavefunction can be approximated by a hydrogen-like ground state wavefunction which is symmetric in space. Therefore, $<\psi_g|ex|\psi_g>=0$. Secondly, it is assumed that the contribution from $<\psi_c|ex|\psi_c>$ is small compared with that from $<\psi_g|ex|\psi_c>$. This assumption has been discussed elsewhere [47] in which it is concluded that the contribution from the term $<\psi_c|ex|\psi_c>$ is indeed an unlikely source of HHG. As a result, the dipole moment is calculated as:

$$d=<\psi_g|ex|\psi_c>+c.c. \tag{2.15}$$

Thirdly, by arguing that harmonic radiation of a given harmonic frequency ($q\omega_o, q=$ odd) must come from the recombining electrons having total energy in the range $q\hbar\omega_o-\hbar\omega_o<E_t<q\hbar\omega_o+\hbar\omega_o$, the continuum wavefunction is expressed as a series of free electron wavefunctions having harmonic frequencies of the incident field frequency. That is,

$$\psi_c=\sum\psi_q=\sum A_q e^{ip_qx/\hbar}e^{-iq\omega_o t} \tag{2.16}$$

where p_q is the re-collision momentum of the tunnel ionized electrons that satisfies the energy conservation equation:

$$\hbar q\omega_o=\frac{p_q^2}{2m}+I_p \tag{2.17}$$

The left hand side of the equation is simply the harmonic photon energy whereas the right hand side is the *total* energy which the electrons will give up by recombining to the atomic ground state with a potential energy I_p. It should be noted that for a given peak electric field strength E_o, the maximum re-collision kinetic energy an electron can have is about 3.2 U_p (see Section 2.1.2). Consequently, harmonic photon energy should be limited to $q\hbar\omega_o\leq 3.2\,U_p+I_p$ which is just the cut-off law described in Chapter 1. The amplitude A_q is obtained from the consideration that each of the wave components in Eqn. (2.16) should represent the tunnel ionized electrons having total re-collision energy in the range $\hbar\omega_h - \hbar\omega_o < E_e < \hbar\omega_h + \hbar\omega_o$ where $E_e = p^2/2m + I_p$. Therefore, by assuming a spatial extent V_q (see discussion below) for the qth wavefunction component, ψ_q, at re-collision, A_q can be determined by the following normalization condition:

$$|A_q|^2 V_q = \int_{q\hbar\omega_o - \hbar\omega_o}^{q\hbar\omega_o + \hbar\omega_o} \left(\frac{dP(E_e)}{dE_e} \right) dE_e \tag{2.18}$$

Here, $P(E_e)$ is just the tunnel ionization probability expressed in terms of the total re-collision kinetic energy E_e of the tunnel ionized electrons. The left side of Eqn. (2.18) simply denotes the number of electrons represented by ψ_q whereas the right side of the equation represents the number of electrons having re-collision energy between $q\hbar\omega_o - \hbar\omega_o$ and $q\hbar\omega_o + \hbar\omega_o$. The spatial extent at re-collision, V_q, is assumed to consist of two terms. The first is the extent of the electron wavefunction in the directions perpendicular to the electric field and is assumed to be caused by spreading of the wavefunction resulting from the uncertainty in the initial transverse electron momentum at the time of ionization (see Section. 2.1.2). In Ref. [25], this spread is assumed to vary linearly in time and has a value obtained from experimental considerations [3]. The second is the extent of the qth wavefunction component in the direction of the electric field or the longitudinal spread. This is taken as the re-collision velocity $v_q = p_q/m$ multiplied by the time difference, δt, between the times when the electron having energy $\hbar\omega_h - \hbar\omega_o < E_e < \hbar\omega_h + \hbar\omega_o$ passes the parent atom. Therefore the wavefunction extent is given by $V_q = (\pi r_s^2)[(p_q/m)\delta t]$ where r_s is the transverse wavefunction spread.

Two important effects have been neglected in this model. The first is the depletion of the ground state wavefunction and the second is the phase relation between the continuum wavefunction components representing the electrons recombining at different times and having the same re-collision energy. These two effects will be incorporated in the extended model described below and their importance will also be discussed.

---

[3] In the extended model discussed below, however, this spreading is obtained from the uncertainty in initial velocity of the tunnel ionized electrons.

The extended model

The extended model developed here follows the same general principle as the Corkum model discussed above. The dipole moment is calculated as:

$$d(t) = \langle \Psi_g | ex | \Psi_c \rangle \tag{2.19}$$

However, the forms of the ground state and continuum wavefunctions have been modified. These modifications have been made to account for the depletion of the ground state wavefunction and the phase of the continuum wavefunction.

For ultra-high intensity laser pulses, ionization and therefore ground state depletion proceed very rapidly, on the time scale of a fraction of the pulse duration. Therefore, since HHG ceases when no more electrons can be ionized, the temporal durations of the generated harmonics will depend to a large extent on the depletion of the ground state. In this extended model, the ground state wavefunction is now calculated as the steady state ground state wavefunction, ψ_g, multiplied by a time-dependent amplitude $a(t)$:

$$\Psi_g = a(t)\psi_g \tag{2.20}$$

To determine $a(t)$, it is assumed that recombination is small and the ground state population is therefore equal to one minus the tunnel ionization probability $P(t)$:

$$|\Psi_g|^2 = |a(t)|^2 = 1 - P(t) \tag{2.21}$$

Hence,

$$a(t) = \sqrt{1 - P(t)} \tag{2.22}$$

The second modification involved in this extended model is concerned with the phase of the continuum wavefunction. As can been seen from the description of the original model, there is no phase relationship between the various electron trajectories which contribute to the same harmonic emission. In this extended model, this phase relationship is accounted for by assuming that the recombining wavefunction takes the following form:

$$\Psi_c = A(t)e^{i\left[\frac{p_R(t)}{\hbar}x - S(t)\right]} \tag{2.23}$$

where $p_R(t)$ is the re-collision momentum of the tunnel ionized electrons and $S(t)$ is the accumulated phase of the electron wave function given by:

$$S(t) = \frac{1}{\hbar}\int_{t'}^{t} dt'' \left(\frac{p^2(t'')}{2m} + I_p\right) \tag{2.24}$$

Here, $p(t'')$ is the momentum of the tunnel ionized electron as a function time from its birth at t' to its re-collision with the parent atom at t. It should be noted that when A is constant and $p^2/2m \gg I_p$, the wavefunction (Eqn. 2.23) is a solution to the time dependent Schrödinger equation for a free electron in an electric field. The atomic ionization potential I_p is included to account for the effect of the atomic potential on the recombining electrons. As will be shown later, by assuming the wave function in the above form, the phase relationship between the harmonic emission generated at different times in a laser cycle agree very well with the more rigorous quantum model described below.

The time-dependent amplitude $A(t)$ is determined as follows. From Figure 2.4, it is seen that the electrons ionized between t' and $t' + \delta t$ will be in the vicinity, δx, of the parent atom at t. Therefore for small $\delta t'$ and δx and assuming a transverse spread r_s for the electron wavefunction, the electron probability conservation condition is given by:

$$|A|^2(\pi r_s^2)\delta x = \frac{dP(t')}{dt'}\delta t' \tag{2.25}$$

The right side of Eqn. (2.25) simply represents the number of electrons ionized between t' and $t' + \delta t$ while the left side denotes the number of electrons in the vicinity of the parent atom within the volume defined by δx and the transverse spread r_s. In this extended model, the transverse spread of the electron wavefunction r_s is calculated from the uncertainty in the transverse velocity of the tunnel ionized electrons by using Eqn. (2.10) for $|\Delta v|$,

$$r_s = |\Delta v(t - t')| = \sqrt{\frac{2\hbar}{m\frac{\sqrt{2mI_p}}{eE}}(t - t')} \tag{2.26}$$

That is, the transverse spread is interpreted here as the net drift of the classical electron trajectories in the direction perpendicular to the external electric field. By noting that $\delta x/\delta t'$ is just the change of electron displacement at time t (at which $x \approx 0$) due to a change in the ionization time t' and can be approximated by $|\partial x\ /\partial t'|$, the time dependent amplitude of the electron wavefunction is then given by:

$$A(t) = \sqrt{\frac{\frac{dP(t')}{dt'}}{\pi r_s^2(t)\left|\frac{\partial x}{\partial t'}\right|}} \tag{2.27}$$

Physically, $|\partial x\ /\partial t'|$ is evaluated at $x = 0$ and can be interpreted as the longitudinal spread of the electron wavefunction [4].

2.1.4 The quantum dipole model

This model has been developed by Lewenstein and co-workers [32] and is obtained by a more mathematically and quantum mechanically rigorous analysis. A summary of this analysis is given below and a complete description of the model can be found in Ref.[32].

Similar to the semi-classical model, the quantum model starts with an expansion of the time-dependent wavefunction of the atomic system into a time dependent ground state wavefunction $\Psi_g(t)$ and a time-dependent continuum state wavefunction $\Psi_c(t)$:

$$\begin{aligned}\Psi(t) &= \Psi_g(t) + \Psi_c(t) \\ &= a(t)\psi_g e^{iI_pt} + \int d^3v\, b(\vec{v}, t)\psi_{\vec{v}} e^{iI_pt}\end{aligned} \tag{2.28}$$

where ψ_g and and $\psi_{\vec{v}}$ are the wavefunctions representing the field-free ground state and continuum states of the atomic system, and $a(t)$ and $b(\vec{v}, t)$ are the corresponding time dependent amplitudes to be determined.

---

[4] The absolute sign is used to ensure the longitudinal spread calculated is a positive quantity.

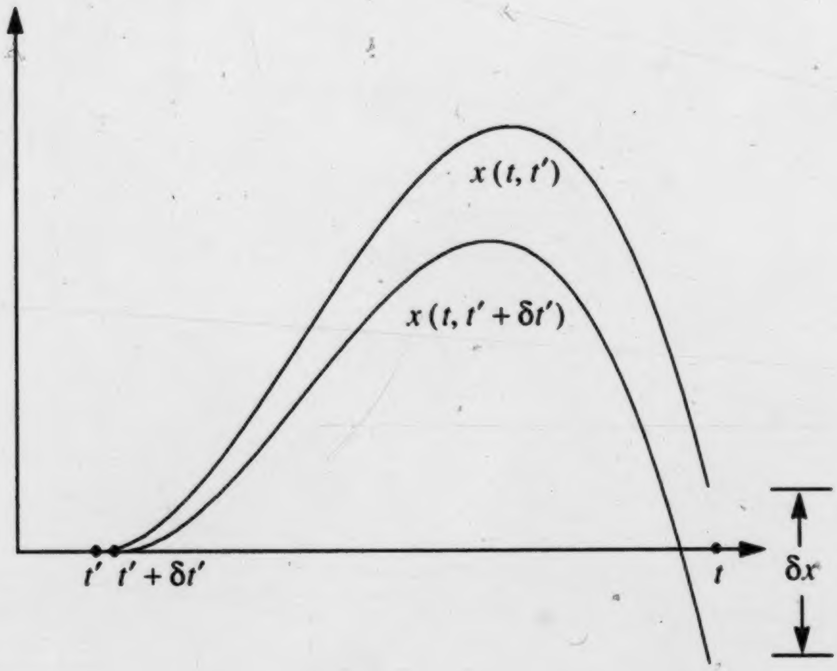

Figure 2.4: The electron trajectories calculated from two slightly different ionization times. The difference in displacement between these two trajectories at the re-collision time t is denoted by δx.

By substituting $\Psi(t)$ into the time-dependent Schrödinger equation (Eqn. 1.3) for a linearly polarized electric field and neglecting the effects of the atomic potential on the continuum states ψ_c, a differential equation for $b(\vec{v},t)$ is obtained :

$$i\hbar\frac{\partial b}{\partial t} = \left(\frac{mv^2}{2} + I_p\right) b(\vec{v},t) - ieE(t)\frac{\hbar}{m}\frac{\partial b}{\partial v_x} + a(t)eE(t)d_x(\vec{v}) \qquad (2.29)$$

where $d_x(\vec{v})$ is the bound-free dipole transition element defined as:

$$d_x(\vec{v}) = \langle\psi_{\vec{v}}|x|\psi_g\rangle \qquad (2.30)$$

From Eqn. (2.29), a closed form solution of $b(\vec{v},t)$ can be obtained [5]:

$$\begin{aligned} b(\vec{v},t) &= -\frac{i}{\hbar}e\int^t dt' a(t')E(t')d_x\left(\vec{v} + \vec{A}(t) - \vec{A}(t')\right) \\ &\quad \times \exp\left\{-\int_{t'}^t dt''\frac{i}{\hbar}\left[\frac{m}{2}\left(\vec{v} + \vec{A}(t) - \vec{A}(t'')\right)^2 + I_p\right]\right\} \qquad (2.31) \end{aligned}$$

where $\vec{A}(t)$ is the vector potential given by:

$$\vec{A}(t) = A(t)\hat{x} = \frac{e}{m}\int^t dt' E(t')\hat{x} \qquad (2.32)$$

By considering only the transitions from the continuum states back to the ground state, i.e. $d(t) = <\Psi_g|ex|\Psi_c>$, the dipole moment can be obtained as:

$$\begin{aligned} d(t) = \quad & -\frac{i}{\hbar}e^2\int^t dt'\int d^3v\, a^*(t)a(t')E(t')d_x\left(\vec{v} + \vec{A}(t) - \vec{A}(t')\right) \\ & \times d_x^*(\vec{v})\exp\left[-iS(\vec{v},t,t')\right] \qquad (2.33) \end{aligned}$$

where

$$S(\vec{v},t,t') = \int_{t'}^t dt''\frac{i}{\hbar}\left[\frac{m}{2}\left(\vec{v} + \vec{A}(t) - \vec{A}(t'')\right)^2 + I_p\right] \qquad (2.34)$$

is called the quasi-classical action.

As discussed in Ref. [32], the dipole expression as given by Eqn. (2.33) has the physical interpretation as a sum of probability amplitudes corresponding to the recombination process. The term $E(t)d_x\left(\vec{v} + \vec{A}(t) - \vec{A}(t')\right)$ is the probability amplitude for a bound electron to make the transition to the continuum at t' with velocity

---

[5] For a description of the analytical method involved, see for example Ref. [48] p442-443.

$\vec{v}$. The electron then propagates and acquires a phase equal to $\exp[-iS(\vec{v},t,t')]$. Finally, the electron recombines with the atom at t with a probability amplitude equal to $d_x^*(\vec{v})$.

By using stationary phase analysis, it is shown in Ref. [32] that the main contribution to the dipole integral (Eqn. (2.33)) comes from the electrons which are ionized from the atom with zero initial velocity and then return to the vicinity of the parent atom. Further analysis of the Fourier transform of the dipole moment indicates that the main contribution to the qth harmonic emission is due to the re-colliding electrons which have kinetic energy equal to $\hbar q\omega_o - I_p$. Hence, this quantum theory justifies the three-step description from the semi-classical analysis. A quantitative justification will be given in the next section.

2.1.5 The ionization model

In the tunnelling regime ($\gamma < 1$), a third model has been proposed by Brunel to describe HHG. In [42], it is shown that the time dependent tunnel ionization current can be a source of harmonic generation. Here, the rate of change of the tunnel ionization current is found to be:

$$\frac{\partial J}{\partial t} = \frac{e^2}{m} n_o P(t) E \tag{2.35}$$

where n_o is the background electron density and P(t) is the tunnel ionization probability. Using the correspondence relation:

$$\frac{\partial^2}{\partial t^2} n_o d(t) = \frac{\partial J}{\partial t} \tag{2.36}$$

the dipole acceleration can be found:

$$\frac{\partial^2}{\partial t^2} d(t) = \frac{e^2}{m} P(t) E \tag{2.37}$$

Since $P(t)$ is a highly nonlinear function of E, harmonic components can be generated by such a dipole acceleration

As will be shown later, for very high frequency harmonics, the harmonic emission as predicted by this model is negligible compared to that predicted by the semi-classical and quantum recombination dipole models. The major use of this dipole model in this investigation is to account for free electron induced dispersion in the propagation analysis (see Section 2.2).

2.1.6 Evaluation of the various dipole moments

Tunnel ionization and the ionization dipole moment

The tunnel ionization probability can be most easily evaluated from Eqn. (2.7):

$$P(t) = 1 - \exp\left(\int^{t} R_t(E(t''))dt''\right)$$

where the integration over the ionization rate R_t can be readily computed numerically. The ionization dipole acceleration (Eqn. (2.37) given by:

$$da(t) = \frac{e^2}{m} P(t) E$$

can then be readily obtained.

The semi-classical dipole moment

For a hydrogen-like ground state wave function [32]:

$$\psi_g = \left(\frac{\alpha^{3/4}}{\pi^{1/2}}\right) e^{-\sqrt{\alpha}|\vec{r}|} \tag{2.38}$$

where $\alpha = \frac{I_p}{I_h}/a_B^2$, I_p is the ionization potential of the atom, I_h is the ionization potential of the hydrogen atom, a_B is the Bohr radius. The semi-classical dipole moment can be obtained by substituting Eqn. (2.20) and Eqn. (2.23) into Eqn. (2.19) to give:

$$d(t) = (ea_B)(2\pi)^{3/2}\tilde{A}(t)\tilde{d}_x(\tilde{v}_R(t))e^{-iS(t,t')} + c.c. \tag{2.39}$$

where the normalized amplitude is given by:

$$\tilde{A}(t) = \sqrt{\frac{(1 - P(t))(1 - P(t'))(t_o R_t(t'))}{\left(\pi \frac{r_t^2}{a_B^2}\right) \frac{\partial(x/a_B)}{\partial(t'/t_o)}}} \tag{2.40}$$

Here t_o is the fundamental cycle of the driving laser and $\tilde{d}_x$ is the normalized free-bound transition element given by:

$$\tilde{d}_x(\tilde{v}_R(t)) = \left(\frac{1}{a_B/v_o^{3/2}}\right)(-i)2^4\frac{\left(\frac{U_p}{I_p}\right)^{1/2}}{\left(\frac{I_p}{I_h}\right)^{5/4}}\frac{\tilde{v}_R(t)}{\left(1+2\frac{U_p}{I_p}\tilde{v}_R(t)^2\right)^3} \tag{2.41}$$

where v_o is the atomic unit of velocity, $\tilde{v}_R(t) \equiv v(t)/(2\sqrt{U_p/m})$ is the normalized electron velocity at re-collision and $U_p = \frac{1}{4}(e^2E_o^2)/(m\omega^2)$ is the peak ponderomotive potential of the driving electric field. The normalized transverse spread can be expressed as:

$$\frac{r_s}{a_B} = 2\pi\frac{(U_p/2I_p)^{1/4}}{\sqrt{\hbar\omega/2I_h}}(\tilde{t}-\tilde{t}') \tag{2.42}$$

where $\tilde{t} = t/t_o$ is the normalized time.

Now, assuming that the driving electric field is given by:

$$E(t) = E_o g(t)\cos\omega t \tag{2.43}$$

where $g(t)$ is a slowly varying Gaussian envelope:

$$g(t) = e^{-2\ln 2(t/t_p)^2} \tag{2.44}$$

and t_p is the FWHM of the square of the envelope, the electron velocity at first re-collision with the parent atom is given by (See Eqn. (2.11)):

$$\tilde{v}_R(t) = -2g(t)(\sin\omega t - \sin\omega t') \tag{2.45}$$

where the release time t' is obtained from setting $x(t) = 0$ in the displacement equation (see Eqn. (2.12)):

$$x(t) = \frac{-eE_o}{m\omega_o^2}(-\cos\omega t + \cos\omega t' - \sin\omega t'(\omega t - \omega t')) \tag{2.46}$$

from which the longitudinal spread of the electron wavefunction $\partial x \,/\, \partial t'$ can be found:

$$\left.\frac{\partial x}{\partial t'}\right|_{x=0} = (a_B/t_o)2(2\pi)^2\frac{(U_p/\hbar\omega)}{(\hbar\omega/2I_h)}g(t)\cos\omega t'(\tilde{t}-\tilde{t}') \tag{2.47}$$

Finally, the accumulated phase is given by:

$$S(t,t') = \frac{I_p}{\hbar\omega}\left\{\begin{array}{l} \omega(t-t')\left[1+\frac{U_p}{I_p}g(t)(1+2\sin\omega t'^2)\right] \\ +\frac{U_p}{I_p}g(t)\left[4\sin\omega t'(\cos\omega t-\cos\omega t')-\frac{1}{2}(\sin 2\omega t - sin 2\omega t')\right] \end{array}\right\} \tag{2.48}$$

In order evaluate the dipole moment at time t, the ionization time t' is determined by numerically solving $x(t,t') = 0$ from Eqn. (2.46). Once t' is found, other quantities in Eqn. (2.39) can be easily calculated to give $d(t)$. In this study only the ionization times corresponding to the electron's first re-encounter with the parent atom are calculated. In other words, only the contribution to the dipole moment from electrons which are having their first re-collision with the parent atom is considered.

The quantum dipole moment

Following the suggestions in Ref. [32], the continuum wave functions $\psi_{\vec{v}}$ are assumed to be plane waves of the form

$$\left(\frac{m}{2\pi\hbar}\right)^{3/2} e^{i\frac{m}{\hbar}\vec{v}\cdot\vec{r}} \tag{2.49}$$

The integration over $\vec{v}$ in Eqn. 2.33 is performed analytically using the stationary phase approximation [6]. The dipole moment then becomes:

$$\begin{aligned} d(t) \;=\; & (ea_B)\frac{2(2\pi)^{3/2}}{\sqrt{i}}\sqrt{\frac{U_p}{2I_h}}\left(\frac{\hbar\omega}{2I_h}\right)^{3/2} \\ & \int_{t_a}^{t} d\tilde{t}'\left(\frac{1}{\tilde{t}-\tilde{t}'}\right)^{3/2} a^*(t)a(t')\tilde{E}(t')\tilde{d}_x\left(\tilde{v}_s(t,t')+\tilde{A}(t)-\tilde{A}(t')\right)\tilde{d}_x^*(\tilde{v}_s(t,t')) \\ & \times\exp\left[-iS_s(t,t')\right] \end{aligned} \tag{2.50}$$

Here $\tilde{t} = t/t_o$ is the normalized time; $\tilde{E}(t) = E(t)/E_o$ is the normalized electric field where E_o is the maximum field strength; $U_p = \frac{1}{4}(e^2E_o^2)/(m\omega^2)$ is the peak ponderomotive potential; $\tilde{d}_x(v)$ is the normalized transition element given by Eqn. (2.41) for a hydrogen-like ground state wave function; $\tilde{A} = 2\pi\int\tilde{E}d\tilde{t}$ is the normalized vector potential; and $\tilde{v}_s$ is the normalized stationary velocity given by:

$$\tilde{v}_s(t,t') = -\frac{1}{\tilde{t}-\tilde{t}'}\int_{\tilde{t}'}^{\tilde{t}} d\tilde{t}''\left[\tilde{A}(t)-\tilde{A}(t'')\right] \tag{2.51}$$

---

[6] A discussion of this method can be found in Ref. [49] p316-p317.

Lastly, the stationary value of the classical action is given by:

$$S_s(t,t') = \int_{\tilde{t}'}^{\tilde{t}} d\tilde{t}''2\pi \left[2\frac{U_p}{\hbar\omega_o}\left(\tilde{v}_s(t,t') + \tilde{A}(t) - \tilde{A}(t'')\right)^2 + \frac{I_p}{\hbar\omega_o}\right] \tag{2.52}$$

The remaining quantity that is required in order to evaluate the dipole moment is the time-dependent ground state amplitude $a(t)$ which, as is shown in Ref. [32], can also be consistently determined by the rigorous analysis described therein. However, an analysis which neglects the effects of the atomic potential on the continuum states has been shown to give inaccurate ionization rates [27]. This in turn will lead to an inaccurate determination of the ground state amplitude. Therefore, in this study, the ground state amplitude in the rigorous model is calculated as $a(t) = \sqrt{1 - P(t)}$ where $P(t)$ is the ionization probability (Eqn. 2.7) obtained from the Ammosov-Delone-Krainov (ADK) ionization rate (Eqn.2.4). This rate has been obtained from analysis which does take into account the effects of the atomic potential on the ionizing electrons [29].

Numerical evaluation of the dipole moment can be more easily implemented by defining the following quantiles:

$$\tilde{B}(t) = 2\pi \int^{\tilde{t}} \tilde{A}(\tilde{t}'')d\tilde{t}'' \tag{2.53}$$

$$\tilde{C}(t) = 2\pi \int^{\tilde{t}} \tilde{A}^2(\tilde{t}'')d\tilde{t}'' \tag{2.54}$$

Then

$$\tilde{v}_s(t,t') = -\tilde{A}(t) + \frac{1}{2\pi(\tilde{t} - \tilde{t}')}(\tilde{B}(t) - \tilde{B}(t')) \tag{2.55}$$

and

$$S_s(t,t') = 2\frac{U_p}{\hbar\omega_o}\left[\tilde{C}(t) - \tilde{C}(t') - \frac{(\tilde{B}(t) - \tilde{B}(t'))^2}{2\pi(\tilde{t} - \tilde{t}')}\right] + \frac{I_p}{\hbar\omega_o}2\pi(\tilde{t} - \tilde{t}') \tag{2.56}$$

It should be noted that, unlike the evaluation of the extended semi-classical dipole moment, no slowly varying envelope approximation is used to calculate the dipole moment here. The driving electric field can be an arbitrary function of time. The vector potential A (Eqn. 2.32), the stationary value of the classical action S_s(Eqn. 2.52), the stationary value of the velocity v_s (Eqn. 2.51) and the dipole moment (Eqn. 2.50) are all calculated numerically from the corresponding integral equations.

2.1.7 Results and discussion

Calculations have been done to obtain the dipole acceleration induced by a 150 fs (FWHM) laser pulse interacting with a neon atom. The laser is assumed to have a wavelength of 750 nm and a peak intensity of 10^{15} W/cm^2. These parameters are chosen to model typical HHG experimental conditions in the long-wavelength regime. The dipole acceleration for the semi-classical and quantum models is obtained numerically from the corresponding dipole moment using the central difference formula for second derivatives. Harmonic spectra are obtained by taking the square modulus of the fast Fourier transform of the corresponding dipole accelerations.

Shown in Figure 2.5 are the dipole acceleration power spectra obtained from the quantum and semi-classical models. It is seen that both spectra exhibit a harmonic plateau with a sharp cut-off near the 109th harmonic. The cut-off photon energy from either spectrum agrees well with that predicted by the cut-off law: $\hbar\omega_{max} = I_p + 3.17\ U_p = 21.5\text{ eV} + 3.17(52.5\text{ eV}) = 188.0\text{ eV} = 109\ \text{h}\omega_0$. It is also seen that the magnitude of the plateau harmonics in the two spectra agree very well with one another. The first noticeable difference between the two spectra is that the magnitude of the first few harmonics in the semi-classical spectrum is very small compared to that in the quantum spectrum. The vanishing first harmonics in the semi-classical model is consistent with the fact that the *minimum* re-collision kinetic energy of the electrons is zero. Therefore, the minimum energy of the harmonic photons should be equal to I_p. Consequently, harmonics with photon energy less than I_p cannot be generated by the recombination process described by the semi-classical model. The reason for the non-vanishing low harmonics in the quantum model is not clear. Further investigation may be needed.

Shown in Figure 2.6 is the dipole acceleration power spectrum as obtained from the ionization model. Although the first few harmonics are much larger than the those observed from the quantum and semi-classical spectra, the magnitude of the high harmonics is negligibly small compared to that observed from the quantum or semi-classical results. As discussed in Ref. [34], this generation mechanism may only

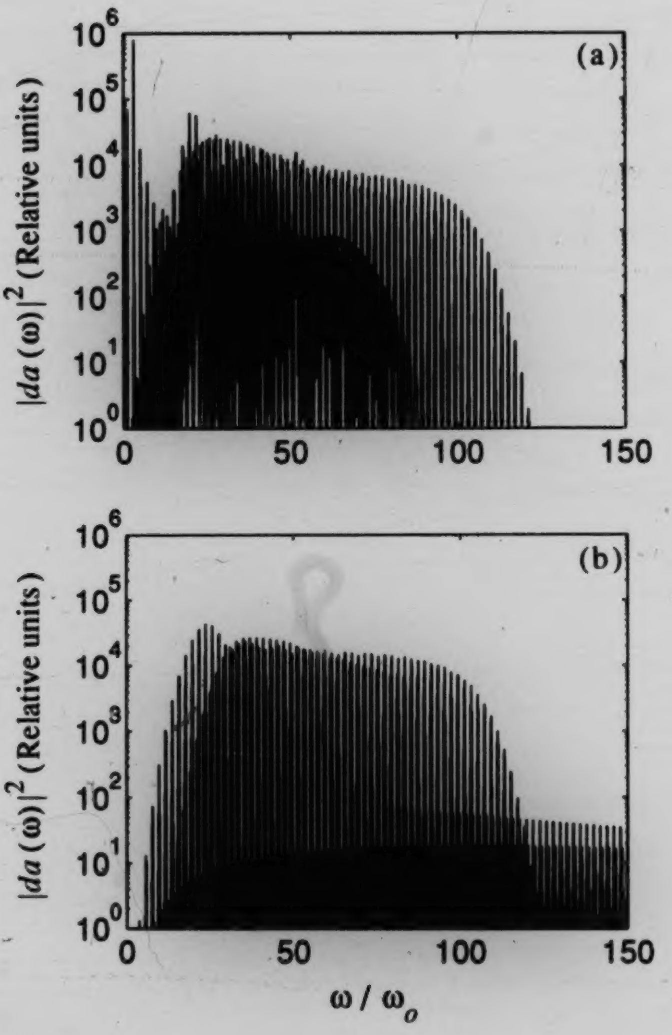

Figure 2.5: Dipole acceleration power spectra obtained from (a) the quantum model and (b) the semi-classical model.

be responsible for the generation of low order harmonics.

A closer examination of the quantum and semi-classical harmonic spectra can be found in Figure 2.7 and Figure 2.8 which show the harmonic spectral regions near the 55th and 85th harmonics. Here, it is seen that all spectra show interesting spectral structure. Specifically, assuming that these are actually odd harmonics, all the harmonic lines are blue shifted from the respective odd harmonic frequencies and they all have large linewidths. These results also show that harmonics in the mid-plateau region seem to have a broader line width than those near the cut-off region. The spectra obtained from the rigorous model appear to have an even larger blue shifted component for the mid-plateau harmonics.

The temporal profile of an individual harmonic can be obtained by using a spectral filter to isolate a particular harmonic line in the *complex* Fourier spectrum and then performing an inverse Fourier transform. The temporal profiles for the 55th and 85th harmonics obtained from the quantum and semi-classical models are shown in Figure 2.9 and Figure 2.10. An ideal (or square) band-pass filter has been used to isolate the spectral regions from h54.8 to h55.8 for the 55th harmonic and from h84.8 to h85.8 for the 85th harmonic. It is seen that the magnitude of the semi-classical harmonics agrees very well with that of the quantum harmonics. Furthermore, harmonics calculated from both models exhibit a general temporal structure. First, all harmonics start to appear at a threshold intensity $I(t)$ corresponding to a ponderomotive potential $U_p(t) = (\hbar\omega_q - I_p)/3.2$. This is consistent with the fact that harmonics can only be generated when the field is high enough to accelerate the electrons to have the necessary re-collision energy. The harmonics then seem to exhibit an interference pattern. Finally, the harmonics vanish when the ground state is depleted due to ionization. For the 55th harmonic, the quantum model predicts a more complicated interference structure than the semi-classical model. For the 85th harmonic, on the other hand, the interference structure is rather similar.

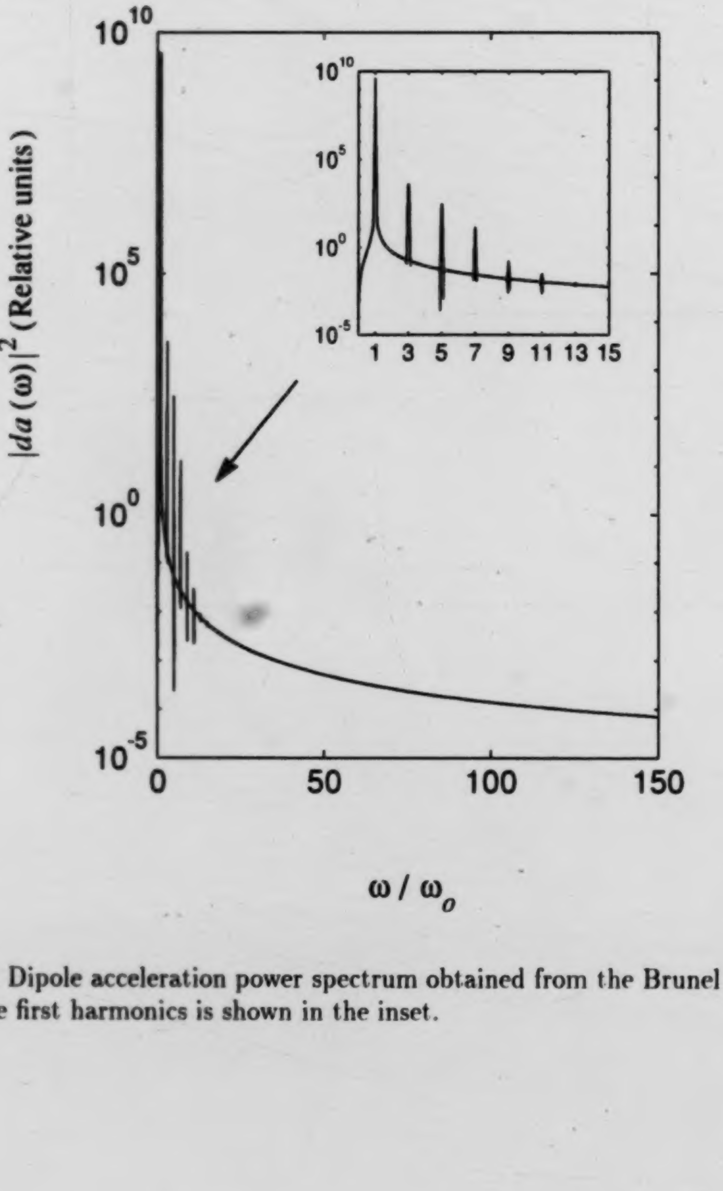

Figure 2.6: Dipole acceleration power spectrum obtained from the Brunel model. A zoom of the first harmonics is shown in the inset.

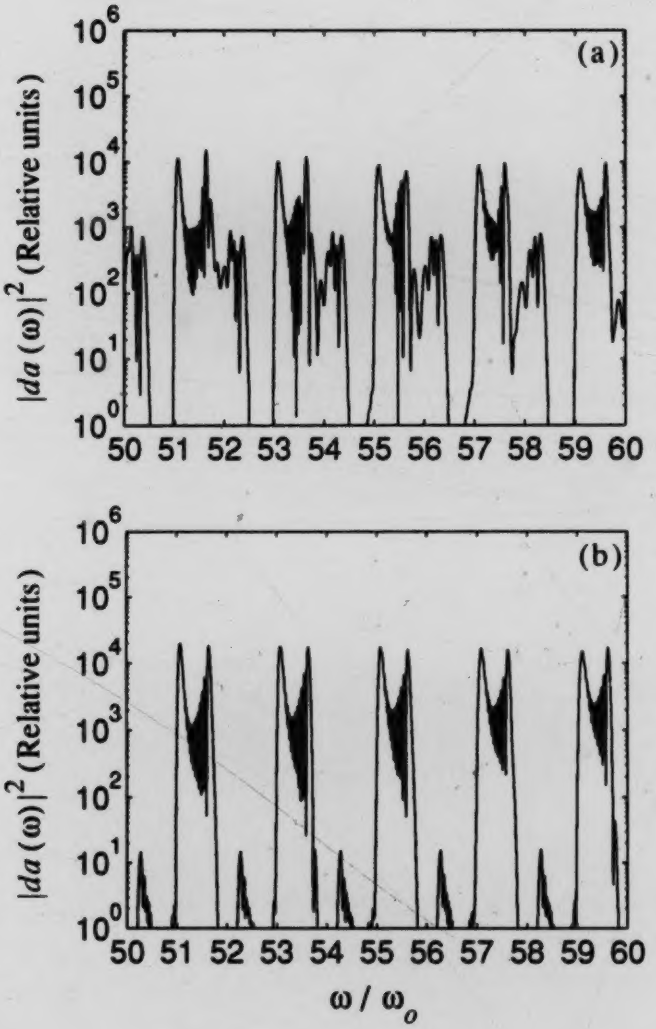

Figure 2.7: Zoom of the dipole acceleration spectra near the 55th harmonic component for (a) the quantum model and (b) the semi-classical model.

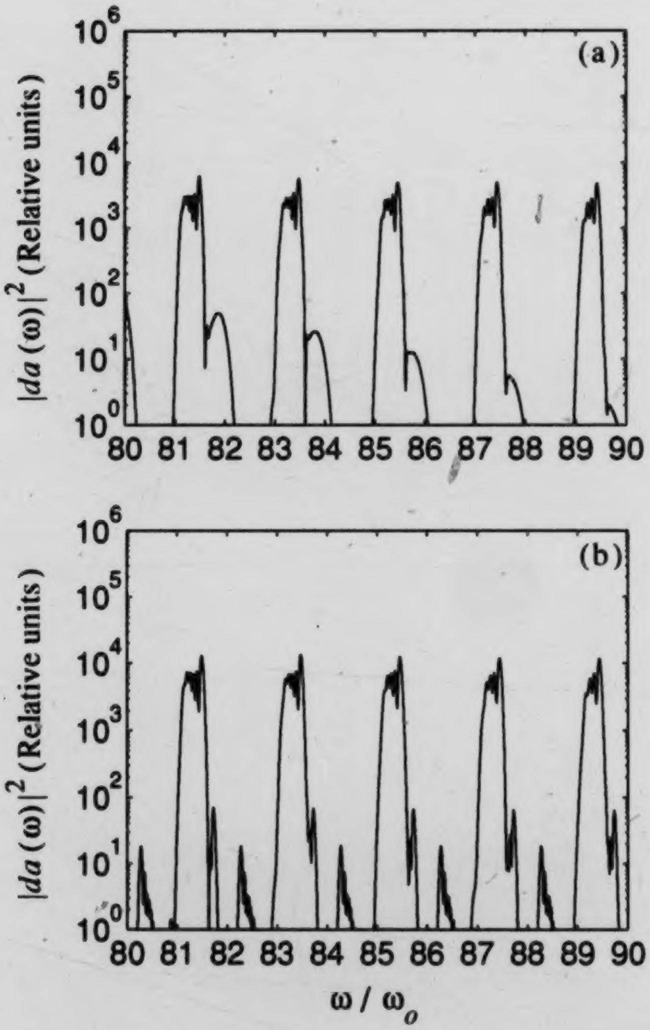

Figure 2.8: Zoom of the dipole acceleration spectra near the 85th harmonic component for (a) the quantum model and (b) the semi-classical model.

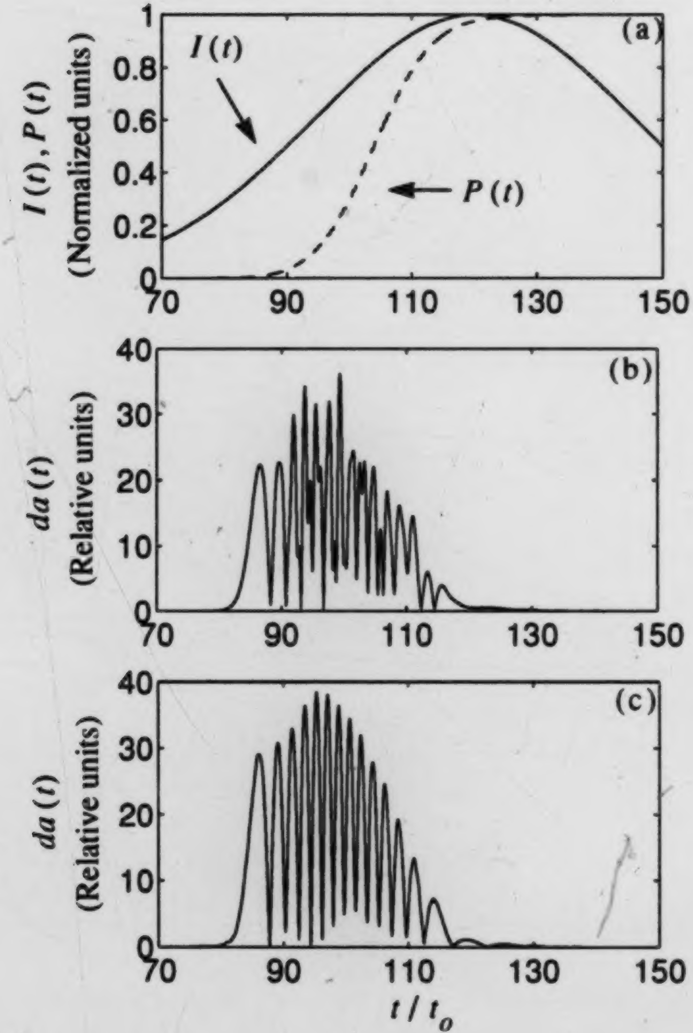

Figure 2.9: Temporal envelopes of the 55th harmonic dipole acceleration components obtained from (b) the quantum model and (c) the semi-classical model. Shown in (a) are the temporal profiles of the driving laser intensity $I(t)$ and the ionization probability $P(t)$.

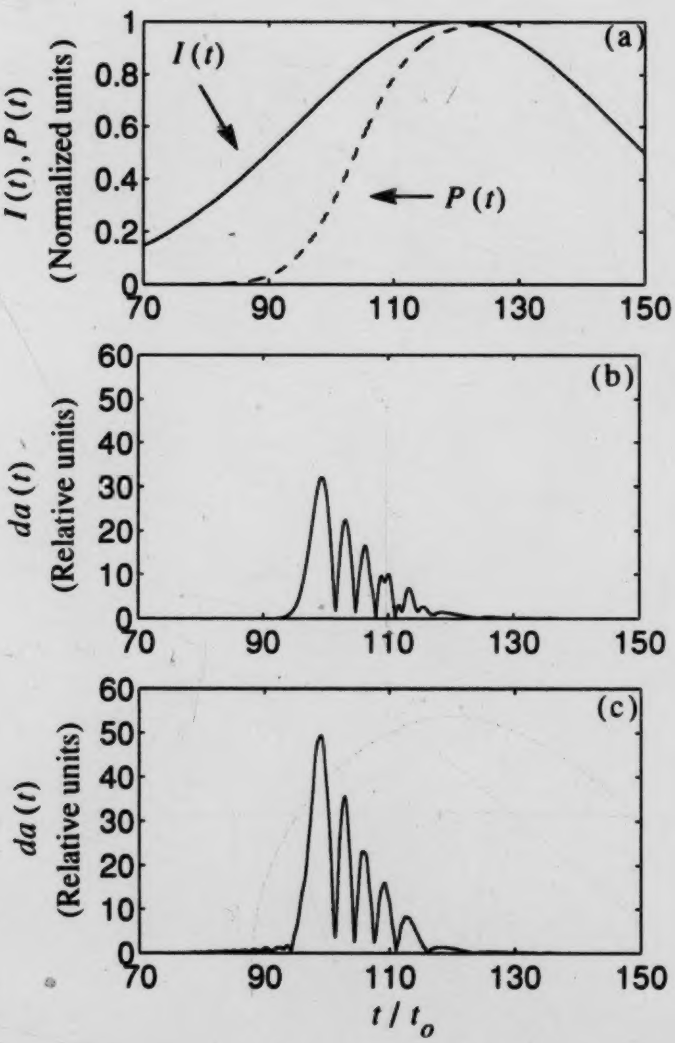

Figure 2.10: Temporal envelopes of the 85th harmonic dipole acceleration components obtained from (b) the quantum model and (c) the semi-classical model. Shown in (a) are the temporal profiles of the driving laser intensity $I(t)$ and the ionization probability $P(t)$.

Explanation of the spectral structure

From Figure 2.7, it is seen that each mid-plateau harmonic line consists of two components separated by a fraction of the fundamental frequency. The corresponding temporal structure of these harmonics may be due to the coherent beating of these two components. As will be shown below, these components correspond to different electron trajectories having the same re-collision energy.

As shown in Section 2.1.6, the semi-classical dipole moment can be written as (see Eqn.(2.39)):

$$d(t) = D(t)e^{-iS(t)} + D^*(t)e^{iS(t)} \tag{2.57}$$

where

$$D(t) = (ea_B)(2\pi)^{3/2}\tilde{A}(t)\tilde{d}(\tilde{v}_R(t)) \tag{2.58}$$

$\tilde{A}(t)$ is the normalized wavefunction amplitude; and $\tilde{d}$ is the normalized dipole transition element and is a function only of the re-collision velocity $v_R(t)$. Now, assuming the dipole moment can be expanded into a sum of harmonic components, $d(t) = \sum_q d_q e^{iq\omega_o t}$, Appendix A shows that using a stationary phase approximation, the qth harmonic dipole component can be approximated as:

$$\begin{aligned} d_q = \quad & \frac{D^*(t_{q1})}{2t_o}\sqrt{\frac{2\pi i}{\dot{KE}_r(t_{q1})}}e^{i[S(t_{q1})-q\omega_o t_{q1}]} \\ + \quad & \frac{D^*(t_{q2})}{2t_o}\sqrt{\frac{2\pi i}{\dot{KE}_r(t_{q2})}}e^{i[S(t_{q2})-q\omega_o t_{q2}]} \\ + \quad & \frac{D^*(t^*_{q1})}{2t_o}\sqrt{\frac{2\pi i}{\dot{KE}_r(t^*_{q1})}}e^{i[S(t^*_{q1})-q\omega_o t^*_{q1}]} \\ + \quad & \frac{D^*(t^*_{q2})}{2t_o}\sqrt{\frac{2\pi i}{\dot{KE}_r(t^*_{q2})}}e^{i[S(t^*_{q2})-q\omega_o t^*_{q2}]} \end{aligned} \tag{2.59}$$

where the t_q's are the four re-collision times at which the electrons have the same re-collision energy (see Figure 2.11), and $\dot{KE}_r$ is the change in the re-collision kinetic energy with respect to the re-collision time. By using a number of considerations, Eqn. (2.59) can be simplified as follows. First, due to the anti-symmetry of the electric field within one laser cycle, i.e. $E(t) = -E(t + t_o/2)$, an electron ionized at $t' + t_o/2$ will follow a trajectory which is just the negative of the trajectory followed by an electron ionized at t'. That is, $x(t, t' + t_o/2) = -x(t - t_o/2, t')$. Therefore, the re-collision velocity corresponding to one of these trajectories should be negative of the other trajectory. The re-collision times are then separated by $t_o/2$, since the two trajectories should occupy the same time duration between ionization and the first re-collision. Consequently, $t_q^* = t_q + t_o/2$. Secondly, since the electrons re-colliding at t_q and t_q^* are ionized at the same electric field *intensity*, the ionization rates at these two times should be also the same. Now further assuming that the electric field envelope and ground state amplitude do not change very much in one laser cycle, it is seen from Eqn. (2.40), $\tilde{A}(t_q) = \tilde{A}(t_{q1}^*)$. Now, since $\tilde{d}_x(v) = -\tilde{d}_x(-v)$ (see Eqn. (2.41), then $D^*(t_q) = -D^*(t_q^*)$. Finally, it can be seen from the symmetry in the electron trajectories that $S(t_{q1}) = S(t_{q1}^*)$ and $K\dot{E}_r(t_{q1}) = K\dot{E}_r(t_{q1}^*)$. Therefore, Eqn. (2.59) becomes:

$$\begin{aligned} d_q = \left(1 - e^{iq\pi}\right) \Bigg\{ & \frac{D^*(t_{q1})}{2t_o} \sqrt{\frac{2\pi i}{K\dot{E}_r(t_{q1})}}\, e^{i[S(t_{q1}) - q\omega_o t_{q1}]} \\ & + \frac{D^*(t_{q2})}{2t_o} \sqrt{\frac{2\pi i}{K\dot{E}_r(t_{q2})}}\, e^{i[S(t_{q2}) - q\omega_o t_{q2}]} \Bigg\} \end{aligned} \tag{2.60}$$

From Eqn. (2.60), it is seen that for $q =$ even, the dipole components vanish. Therefore, only odd harmonics are possible. More important, it is seen that there are two distinct contributions for each harmonic line. One of these contributions comes from the electrons re-colliding at a time before the 3.17 U_p kinetic energy peak whereas the other comes from the electrons re-colliding at a time after the 3.17 U_p kinetic energy peak.

Shown in Figure 2.12 is the dipole acceleration spectrum obtained from the semi-classical model zoomed near the 55th and 85th harmonics. The contributions from the two re-collision times have been explicitly separated. The contribution from the collision time before the 3.17 U_p peak will be referred to as the pre-3.17 component and the contribution from the collision time after the 3.17 U_p peak will be referred to

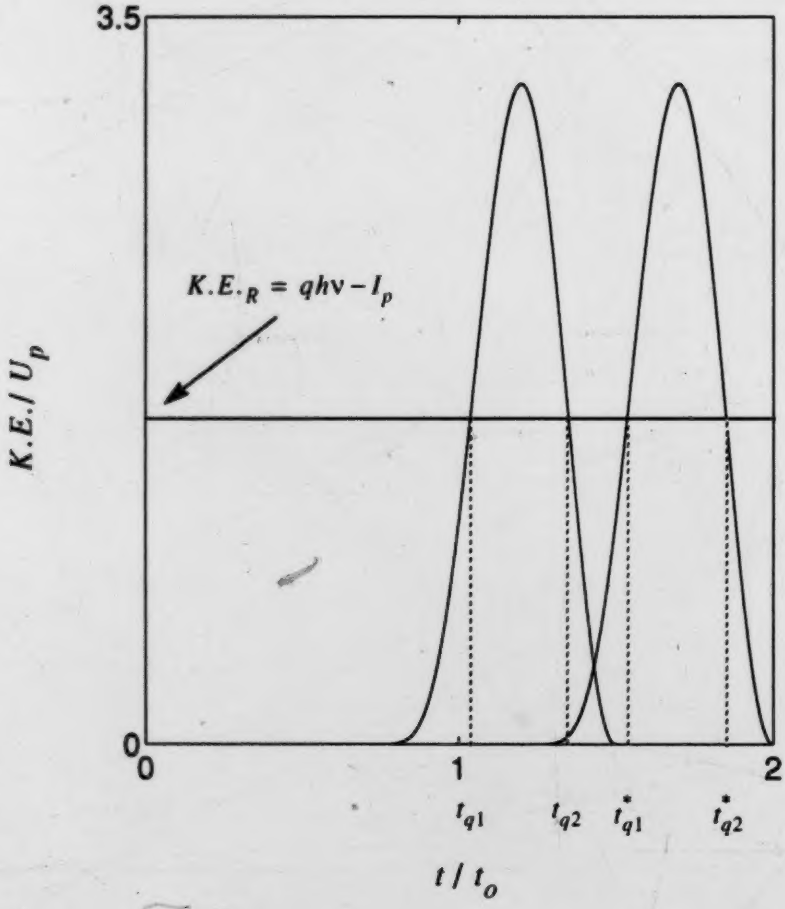

Figure 2.11: The re-collision times at which the electrons have the same re-collision energy.

as the post-3.17 component. The separation is done by setting the dipole moment to zero at time intervals in each laser cycle corresponding to before or after the 3.17 U_p peak. It is seen that both of these components are blue shifted with the post-3.17 component having a larger blue shift. It is also seen that the difference in blue shift between the two components is larger for the lower harmonics than for the higher harmonics.

Before an explanation of the harmonic blue shift is given, it is useful to understand why a larger blue shifted spectral structure is obtained when the quantum model is used. It has been found that such a spectral structure is due to the electrons which are having their second or more re-collision with the parent atom with the same re-collision energy. In the quantum model, the inclusion of these trajectories can be achieved through setting the lower limit, t_a, in the time integration (see Eqn. (2.50)). By setting t_a to a time progressively earlier to the current time t, more and more trajectories are included. Shown in Figure 2.13 and Figure 2.14 is the quantum dipole spectrum zoomed near the 55th and 85th harmonics for different t_a. It is seen that when $t_a = t - t_o$, the quantum spectrum agree very well with the semi-classical spectrum. (The quantum spectrum as shown in Figure 2.7 and Figure 2.8 are obtained with $t_a = t - 2t_o$.)

The agreement between the two models can be more clearly seen in the temporal domain. In Figure 2.15, the magnitude and phase of the 55th harmonic as obtained from the two models are shown. For the quantum model, t_a has been set to $t - t_o$. The pre-3.17 and post-3.17 phases have been obtained using the technique described above. It is seen that aside from a small difference in dipole magnitude, the semi-classical results agree very well with the quantum results. Furthermore, it is seen that the phases of the two harmonic components both increase with time with the post-3.17 phase varying more rapidly than the pre-3.17 phase. In the spectral domain, these *degenerate* time dependent phases then result in the spectral blue shift and line splitting as evidenced from Figure 2.12.

The time dependent nature of the harmonic phase can be easily understood from

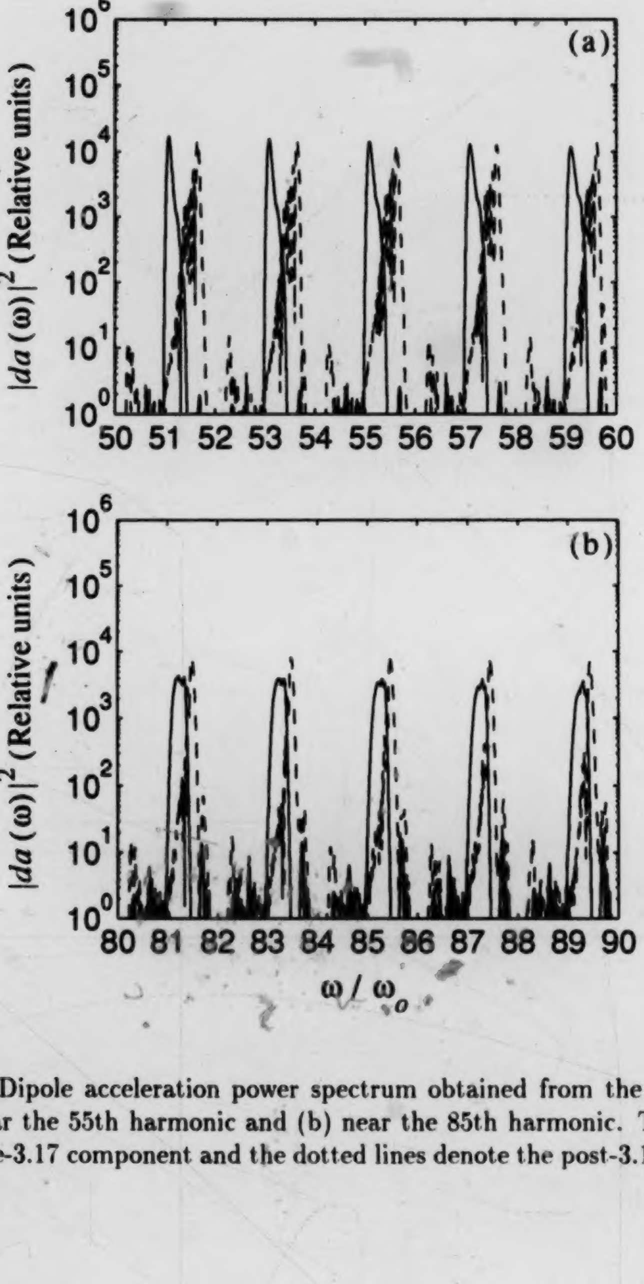

Figure 2.12: Dipole acceleration power spectrum obtained from the semi-classical model (a) near the 55th harmonic and (b) near the 85th harmonic. The solid lines denote the pre-3.17 component and the dotted lines denote the post-3.17 component.

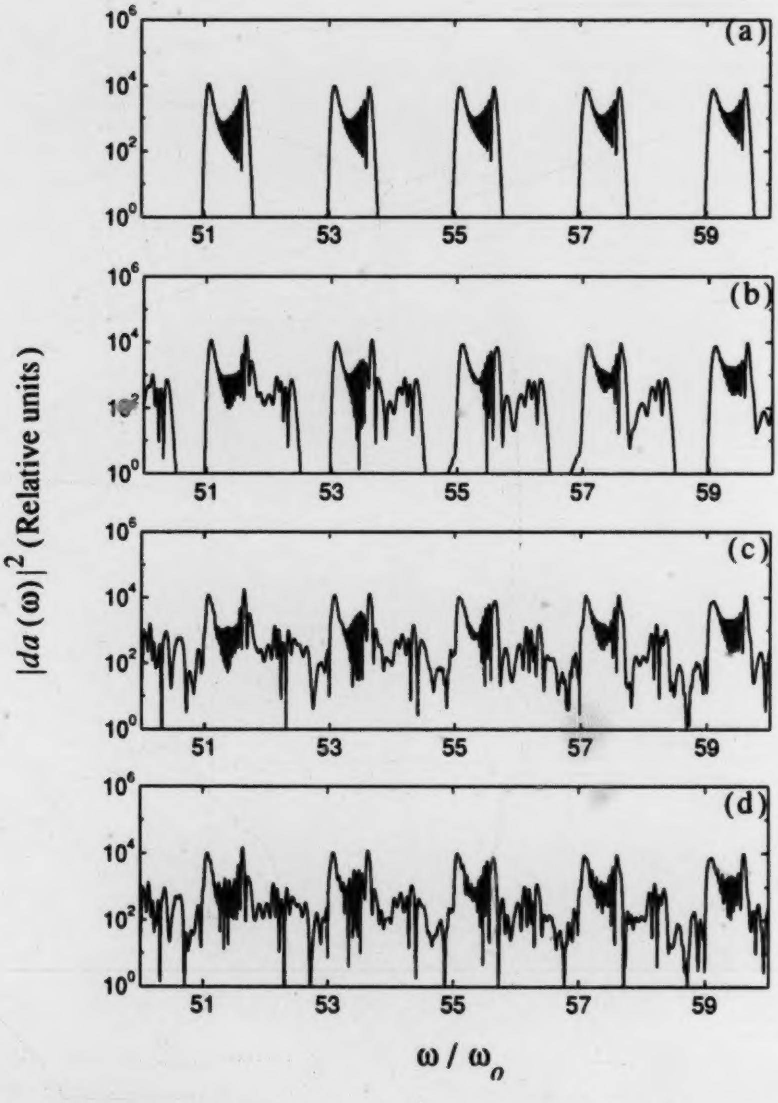

Figure 2.13: Dipole acceleration power spectrum near the 55th harmonic obtained from the quantum model with t_a set to $t - nt_o$ where $n = 1, 2, 3, 4$ in (a), (b), (c), (d), respectively.

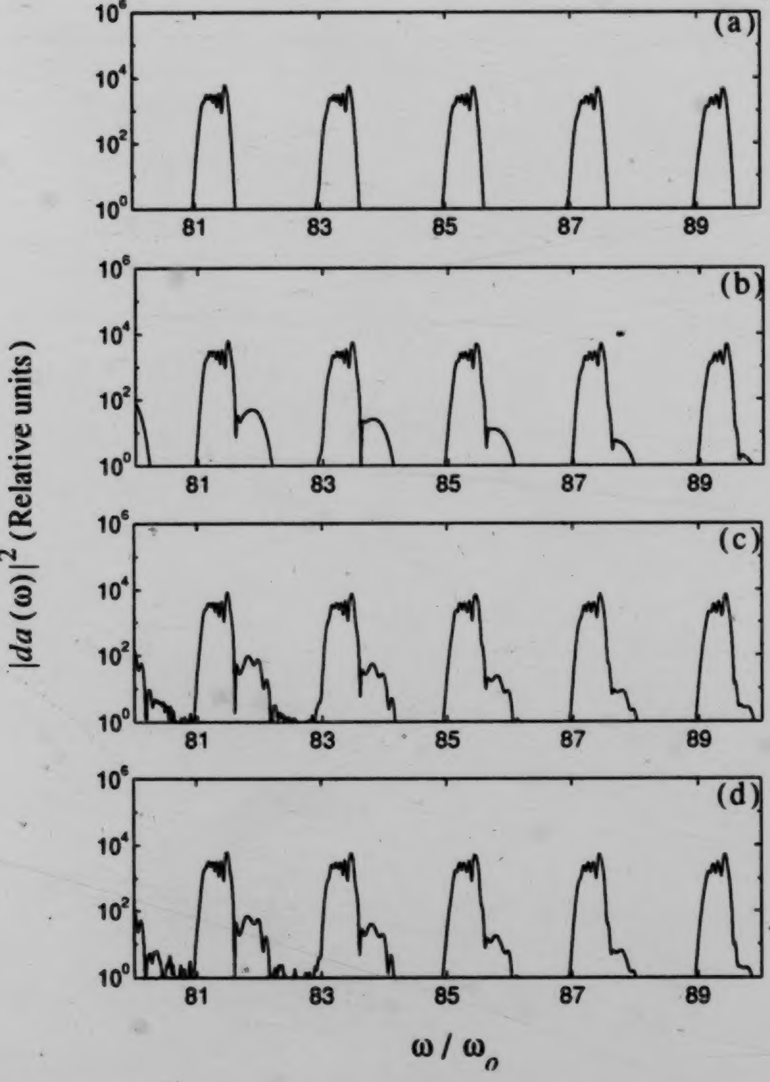

Figure 2.14: Dipole acceleration power spectrum near the 85th harmonic obtained from the quantum model with t' set to nt_o where $n = 1, 2, 3, 4$ in (a), (b), (c), (d), respectively.

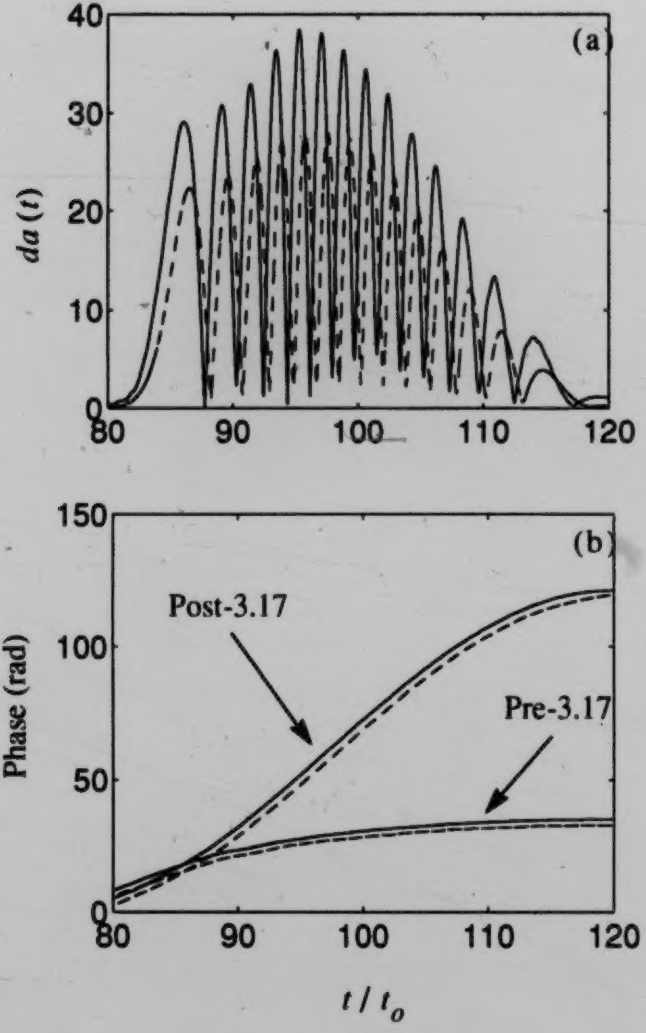

Figure 2.15: Shown in (a) is the amplitude of the 55th harmonic dipole acceleration component. Shown in (b) are the phases of the corresponding Pre-3.17 and Post-3.17 components. The solid lines denote results from the semi-classical model and the dashed lines denote the results from the quantum model.

Eqn. (2.60) where the phase of each harmonic component is explicitly given by:

$$\theta_q = S(t_q) - q\omega_o t_q \tag{2.61}$$

Since both the accumulated phase S and the re-collision time t_q depend on the incident intensity, if the incident intensity is time varying, the harmonic phase should also be time varying. Figure 2.16 shows these quantities for the 55th harmonic as function of fundamental intensities. It is seen that for the pre-3.17 component, both $S(t_q)$ and $q\omega t_q$ decreases with increasing intensity, with the largest change occuring in $q\omega t_q$. This will then lead to an increasing phase dependence on intensity. For the post-3.17 component, both $S(t_q)$ and $q\omega t_q$ increase with intensity with the largest change in $S(t_q)$. This will also result in an increasing phase dependence on intensity. Now since harmonics are generated in the rising edge of the laser pulse where the ground state is still not depleted, the phase of the harmonic components, which is an increasing function of intensity, should also increase with time. This is in agreement with the numerical results seen in Figure 2.15. Figure 2.17 quantifies such an agreement. Shown here are the phases of the pre-3.17 and post-3.17 components of the 55th harmonic as calculated by Eqn. 2.61 as function of incident intensity. Superimposed are the results from Figure 2.15 which have been re-plotted as function of the rising fundamental intensity. It is seen that the phase as predicted by the stationary phase approximation agrees very well with that obtained by the fully time dependent calculation of the dipole moment.

Finally, it should be noted that the the temporal dependence of the real harmonic field is given by $q\omega_o t - \theta_q(t) = q\omega_o(t - t_q) + S(t_q)$. The physical implication is that the phase of the qth harmonic component is locked to the accumulated phase of the electron wavefunction at the time the electron has the required energy to generate the harmonic.

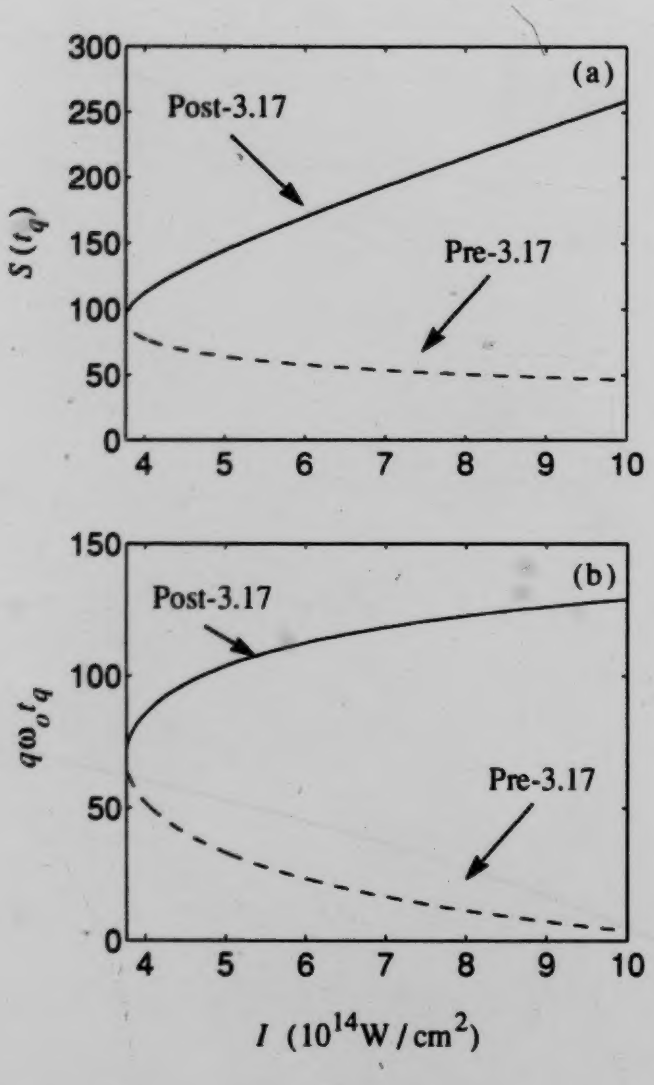

Figure 2.16: The accumulated phase $S(t_q)$ and the recombination phase $q\omega_o t_q$ for the 55th harmonic Pre-3.17 and Post-3.17 components.

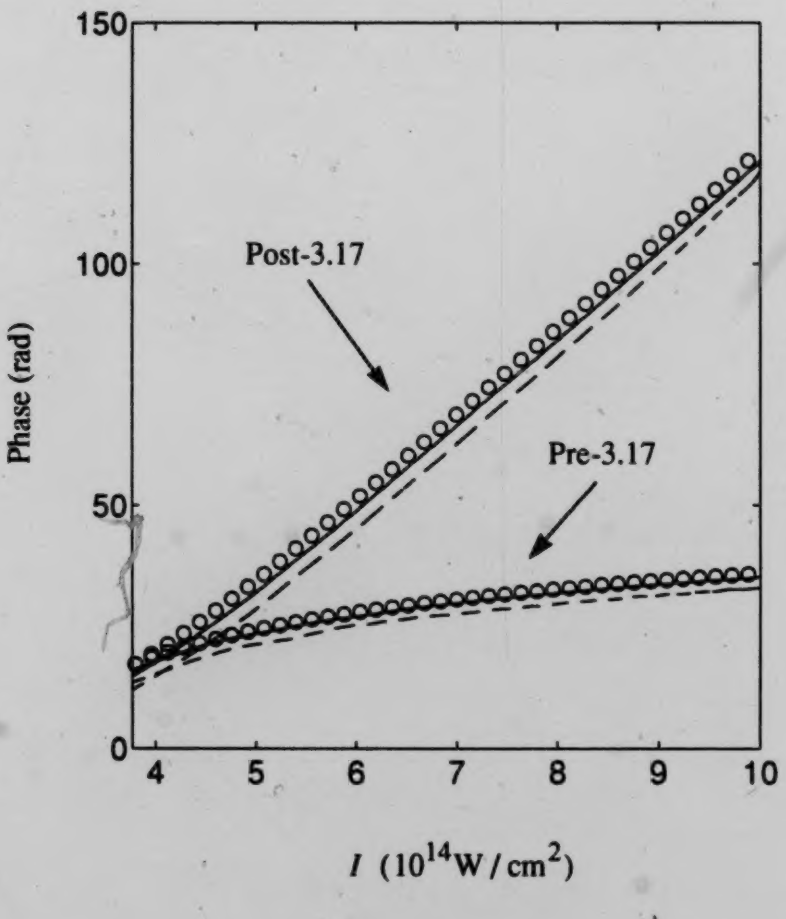

Figure 2.17: Phase of the Pre-3.17 and Post-3.17 55th harmonic dipole acceleration components. The circles, solid lines and dashed lines denote the results obtained respectively from Eqn. (2.61), the semi-classical model and the quantum model.

2.2 Propagation Analysis

In this study, harmonic temporal and spectral behavior is investigated in a one dimensional propagation analysis. Here, the dipole models discussed in Section 2.1 are coupled to a one dimensional wave propagation model. The use of one dimensional analysis neglects several important issues in HHG. These include geometric complications due to beam focussing [2] and free electron induced defocussing [41][7]. However, the use of a one dimensional model allows the efficient computation of the interacting waves and therefore makes the analysis computationally practical. In addition, such a one dimensional approximation is physically appropriate to situations where harmonics are generated by a loosely focussed laser beam interacting with a very thin gas target [8]. In this section, the one dimensional propagation model used in this investigation will be described first. This is followed by a presentation of the calculated results.

2.2.1 The one dimensional propagation model

In the one dimensional propagation model, the HHG process is described by numerical solutions to the the nonlinear wave equation (Eqn. (1.5)) in the one dimensional limit. The polarization source current is derived from the recombination and ionization models. By assuming that the polarization current is due to the driving fundamental alone, the nonlinear wave equation can be decomposed into a wave equation describing the propagation of the driving fundamental wave and a set of wave equations describing the generation and propagation of the harmonic waves. The derivation of these equations is given below.

The general one dimensional nonlinear wave equation is given by:

$$\frac{\partial^2 \underline{E}}{\partial z^2} - \frac{1}{c^2}\frac{\partial^2 \underline{E}}{\partial t^2} = \frac{4\pi}{c^2}\frac{\partial^2 \underline{P}}{\partial t^2} \tag{2.62}$$

---

[7] A more detailed discussion of these effects will be given in Chapter 5.

[8] This will also be discussed in Chapter 5

where $\underline{E}$ is the *total* electric field in the medium and $\underline{P}$ is the polarization induced by the *total* electric field $\underline{E}$. All fields are assumed to be linearly polarized[9] in a direction perpendicular to z. In general, the induced polarization $\underline{P}$ should consist of two terms [2]: $\underline{P} = \underline{P}_g + \underline{P}_d$ where $\underline{P}_g$ is responsible for the generation of the harmonic waves and $\underline{P}_d$ is responsible for the dispersion of these waves. As discussed in the Section 2.1 , in the high field regime considered here, the main contribution to HHG is from the recombination of tunnel ionized electrons. Therefore, $\underline{P}_g = \underline{P}_R = n_o d_R$ where n_o is the background gas density and d_R is the recombination dipole moment. From Section 2.1, it is also seen that harmonics are generated when the ground state is partially depleted. Hence, they are generated in a partially ionized plasma. In such a medium, the main source of dispersion is due to the free electrons. Therefore, $\underline{P}_d = n_o d_I = \frac{e^2}{m} n_e E$ (see Section 2.1.5) where d_I is the ionization dipole moment describing the tunnel ionizing electrons, $n_e = n_o P$ is the electron density in the medium and P is the ionization probability. Consequently, the wave equation becomes:

$$\frac{\partial^2 \underline{E}}{\partial z^2} - \frac{1}{c^2}\frac{\partial^2 \underline{E}}{\partial t^2} - \frac{\omega_{pe}^2(\underline{E},t)}{c^2}\underline{E} = \frac{4\pi}{c^2}\frac{\partial^2}{\partial t^2}\underline{P}_R(\underline{E},t) \tag{2.63}$$

where $\omega_{pe} = (4\pi n_e e^2/m)^{1/2}$ is the plasma frequency and $\omega_{pe}^2(\underline{E},t)$ denotes that the plasma frequency should be calculated from the *total* electric field $\underline{E}$.

Mathematically, the total electric field can be decomposed into two separate fields $\underline{E} = \underline{E}_1 + \underline{E}_h$ and Eqn. (2.63) can be rewritten as:

$$\frac{\partial^2 \underline{E}_1}{\partial z^2} - \frac{1}{c^2}\frac{\partial^2 \underline{E}_1}{\partial t^2} - \frac{\omega_{pe}^2(\underline{E}_1 + \underline{E}_h,t)}{c^2}\underline{E}_1 = 0 \tag{2.64}$$

$$\frac{\partial^2 \underline{E}_h}{\partial z^2} - \frac{1}{c^2}\frac{\partial^2 \underline{E}_h}{\partial t^2} - \frac{\omega_{pe}^2(\underline{E}_1 + \underline{E}_h,t)}{c^2}\underline{E}_h = \frac{4\pi}{c^2}\frac{\partial^2}{\partial t^2}P_R(\underline{E}_1 + \underline{E}_h,t) \tag{2.65}$$

where these two fields [10] are *defined* by the following conditions at $z = 0$:

$$\underline{E}_1(z=0,t) = \underline{E}_L(z=0,t) \tag{2.66}$$

---

[9] It should be noted that the underscored quantities do *not* denote vector fields but represent fast oscillating quantities as opposed to slowly varying envelopes

[10] Physical meanings of these two fields will be discussed shortly.

$$\underline{E}_h(z = 0, t) = 0 \tag{2.67}$$

Here, $\underline{E}_L(z = 0, t)$ is the incident laser's electric field at the medium boundary. It should be noted that since the boundary condition for Eqn. (2.63) is $\underline{E}(z = 0, t) = \underline{E}_L(z = 0, t)$, solving the coupled equations Eqn. (2.64) and Eqn. (2.65) with the specified boundary conditions is completely equivalent to solving Eqn. (2.63). It is now assumed that $\underline{E}_1 \gg \underline{E}_h$ so that the coupled equations may be decoupled as:

$$\frac{\partial^2 \underline{E}_1}{\partial z^2} - \frac{1}{c^2}\frac{\partial^2 \underline{E}_1}{\partial t^2} - \frac{\omega_{pe}^2(\underline{E}_1, t)}{c^2}\underline{E}_1 = 0 \tag{2.68}$$

$$\frac{\partial^2 \underline{E}_h}{\partial z^2} - \frac{1}{c^2}\frac{\partial^2 \underline{E}_h}{\partial t^2} - \frac{\omega_{pe}^2(\underline{E}_1, t)}{c^2}\underline{E}_h = \frac{4\pi}{c^2}\frac{\partial^2 \underline{P}_R(\underline{E}_1, t)}{\partial t^2} \tag{2.69}$$

Physically, Eqn. (2.68) describes the propagation of the driving laser field, $\underline{E}_1$, in the ionizing plasma induced by the driving field itself. Eqn. (2.69) describes the propagation of the harmonic waves generated by the driving field inside the ionizing plasma. In HHG, both experimental [9] and previous theoretical [35] studies have estimated the harmonic conversion efficiency to be very low ($< 10^{-6}$). Therefore the assumption that $\underline{E}_1 \gg \underline{E}_h$ is justified.

As shown in the Section 2.1, for the 150 fs laser pulse studied, the recombination dipole spectrum consists of *discrete* harmonic lines [11]. Consequently, the recombination polarization can be expand as: $\underline{P}_R = \sum_q \underline{P}_q$ where $\underline{P}_q$ oscillates at the qth harmonic frequency $q\omega_o$. By further assuming that $\underline{E}_h$ can also be expanded as $\underline{E}_h = \sum_q \underline{E}_q$, the harmonic wave equation can also be separated into a set of equations of the form:

$$\frac{\partial^2 \underline{E}_q}{\partial z^2} - \frac{1}{c^2}\frac{\partial^2 \underline{E}_q}{\partial t^2} - \frac{\omega_{pe}^2(\underline{E}_1, t)}{c^2}\underline{E}_q = \frac{4\pi}{c^2}\frac{\partial^2 \underline{P}_q(\underline{E}_1, t)}{\partial t^2} \tag{2.70}$$

Now, by imposing homogeneous boundary conditions on this set of equations and by noting that the boundary condition for Eqn. (2.69) is also homogeneous, it is seen that solving this set of equations is completely equivalent to solving Eqn. (2.69).

---

[11] However, for very short fundamental pulses, the spectrum will no longer consist of discrete lines. This will be discussed in detail in Chapter 4

Physically, Eqn. (2.70) describes the propagation of an individual harmonic wave generated by the qth harmonic component of the recombination dipole moment induced by the driving laser field $\underline{E}_1$.

As will be shown in the following subsection, the qth harmonic polarization $\underline{P}_q$ can be expressed as $P_q \exp[i(qk_oz - q\omega_ot)]$ where P_q is a slowly varying envelope in space and time. Then by also expressing the driving and harmonic fields as $\underline{E}_1 = E_1 \exp[i(k_oz - \omega_ot)]$ and $\underline{E}_q = E_q \exp[i(qk_oz - q\omega_ot)]$, a set of envelope equations is obtained:

$$\frac{\partial^2 E_1}{\partial z^2} - \frac{1}{c^2}\frac{\partial^2 E_1}{\partial t^2} + \frac{2i\omega_o}{c}\left(\frac{\partial E_1}{\partial z} + \frac{1}{c}\frac{\partial E_1}{\partial t}\right) - \frac{\omega_{po}^2(E_1,t)}{c^2}E_1 = 0 \qquad (2.71)$$

$$\frac{\partial^2 E_q}{\partial z^2} - \frac{1}{c^2}\frac{\partial^2 E_q}{\partial t^2} + \frac{2iq\omega_o}{c}\left(\frac{\partial E_q}{\partial z} + \frac{1}{c}\frac{\partial E_q}{\partial t}\right) - \frac{\omega_{po}^2(E_1,t)}{c^2}E_q$$
$$= \frac{4\pi}{c^2}\left(\frac{\partial^2 P_q}{\partial t^2} - 2iq\omega_o\frac{\partial P_q}{\partial t} - q^2\omega_o^2 P_q\right) \qquad (2.72)$$

Here the term $\omega_{pe}^2(\underline{E}_1, t)$ has been replaced by $\omega_{po}^2(E_1, t)$ which is just the plasma frequency calculated from the *average* tunnel ionization rate. The average ionization rate is obtained by averaging the static rate R_t (Eqn. (2.4)) for a driving field $|E_1|\cos\omega_o t$ over one laser cycle $2\pi\ /\ \omega_o$ and is given by [28]:

$$R_t^{a.c.}(|E_1|) = (3|E_1|/\pi E_A)^{1/2} R_t(|E_1|) \qquad (2.73)$$

For the driving field strengths studied here, the induced ionization rate is quite small and the ionization probability does not change by very much over many laser cycles. Consequently, the use of the average ionization rate is appropriate.

2.2.2 The qth harmonic polarization component

When the qth harmonic polarization is known, the set of envelope equations (Eqn. (2.71)) and Eqn. (2.72)) can be solved. As will be shown below, the qth harmonic polarization can be expressed as $\underline{P}_q(t) = P_q(t)\exp[i(qk_oz - q\omega_ot)]$ where the slowly varying envelope P_q is given by:

$$P_q(z,t) = n_o(1 - P(z,t))e^{iq\theta_1(z,t)} \int_0^{t_o} dt''\bar{d}(|E_1(z,t)|\cos(\omega_o t''). t'')e^{iq\omega_o t''} \qquad (2.74)$$

Here $\theta_1(t) = \arg(E_1)$ is the fundamental phase deviation from the vacuum phase and $\bar{d}(|E_1(t)|\cos(\omega_o t''), t'')$ is the *steady state* dipole moment [12] calculated for an electric field $|E_1(z,t)|\cos(\omega_o t)$ assuming $|E_1(z,t)|$ is constant over a laser period.

The derivation of Eqn. (2.74) is as follows. From Section 2.1.7, it is seen that the dipole spectrum consists of discrete harmonic lines. Therefore the dipole moment can be expanded as:

$$d(t) = \sum_q d_q(t) e^{-iq\omega_o t} \tag{2.75}$$

where $d_q(t)$ is a slowly varying envelope. Assuming $d_q(t)$ does not change very much in one fundamental cycle t_o, it can be obtained as:

$$d_q(t) = \int_t^{t+t_o} d(t'') e^{iq\omega_o t''} dt'' \quad . \tag{2.76}$$

If the ionization probability is slowly time varying, $P(t'') \approx P(t)$ between t and $t+t_o$. Then,

$$d_q(t) = (1 - P(t)) \int_t^{t+t_o} \bar{d}(t'') e^{iq\omega_o t''} dt'' \tag{2.77}$$

where $\bar{d}$ is the steady state dipole moment calculated by setting $P = 0$ in the dipole expression for a depleting ground state (Eqn. (2.50) and Eqn. (2.39)). By using the stationary phase approximation (See Appendix A) and the semi-classical dipole moment (see Section 2.1.6), $d_q(t)$ is given by:

$$d_q(t) = \epsilon a_B (2\pi)^{3/2} (1 - P(t)) \sum_{t_q} \sqrt{\frac{t_o R_t(t')}{\pi \frac{r_t^2(t_q)}{a_B^2} \left. \frac{\partial(x/a_B)}{\partial(t'/t_o)} \right|_{t_q}}} \tilde{d}_x(\tilde{V}_R(t_q)) e^{-i[S(t_q) - q\omega_o t_q]} \tag{2.78}$$

Here, t_q corresponds to the various re-collision times between t and $t+t_o$ at which the tunnel ionized electrons have the necessary energy to produce the qth harmonic. The ionization probability is assumed to be slowly varying and remains at the value $P(t)$ between t and $t+t_o$. Now, if d_q in Eqn. (2.78) has been obtained for a fundamental field $E_1(t)\cos(\omega_o t)$, a change in the fundamental phase, $E_1(t)\cos(\omega_o t - \theta_1(t))$, will affect d_q as follows. First, assuming $E_1(t)$ and $\theta_1(t)$ do not change significantly during one laser cycle, the phase shift of the driving field near t means that the real oscillating field near t is shifted forward in time by an amount $\delta t = \theta_1(t)/\omega_o$. Therefore, *both* the ionization time $t'(t_q)$ and recombination time t_q are shifted by the same amount. Hence, quantities in Eqn. (2.78) which do not depend explicitly on these times or depend only on the condition *between* these times will not be affected. For example, the ionization rate is dependent on the *electric field strength* at t'. Since both the field and the ionization time are shifted by the same amount, the ionization rate at t' remains the same. A second example is the re-collision velocity v_R and the accumulated phase S which depend on the electric field between t' and t_q. Since the electric field profile remains the same between these two times, these quantities will also not be affected. The only quantity in Eqn. (2.78) which depends explicitly on the recombination time is the recombination phase in the exponential which will be changed to $e^{i(q\omega_o t_q + q\theta_1(t))}$. Consequently, $d_q(|E_1(t)|\cos(\omega_o t - \theta_1(t)), t) = e^{iq\theta_1(t)} d_q(|E_1|(t)\cos(\omega_o t), t)$. Therefore, $d_q(|E_1(t)|\cos(\omega_o t - \theta_1(t)), t)$ can be evaluated as:

---

[12] That is, the ionization probability $P(t)$ is artificially set to zero in the dipole expression.

$$d_q(t) = (1 - P(t))e^{iq\theta_1(t)} \int_0^{t_o} dt'' \bar{d}(|E_1|(t)\cos(\omega_o t''), t'')e^{iq\omega_o t''} \tag{2.79}$$

Here the limits of integration have been changed to 0 and t_o. This is justified because due to the periodicity of $\bar{d}(t)$ near t, the re-collision phases $\omega_o t_q$ between the phase $\omega_o t$ and $\omega_o(t + t_o)$ will be the same as those between the phase $\omega_o(t + \delta t)$ and $\omega_o(t + t_o + \delta t)$ where $|\delta t| < t_o$. Therefore a convenient interval to carry out the Fourier integration will be between 0 and t_o. Finally, by noting that the real electric field is given by $\underline{E}_1 = |E_1|\cos(\omega_o t - k_o z - \arg(E_1))$ and that the polarization is related to the dipole moment by $P_R = n_o d$, Eqn. (2.74) results.

2.2.3 Simulation results and discussions

The 1-D model has been incorporated into an efficient numerical scheme (see Appendix B) to study the effects of propagation on the spectral and temporal characteristics of high harmonics. This model has also been used to examine the HHG conversion efficiency in the 1-D limit. Results have been obtained for a 150 fs laser pulse propagating in 500 torr of neon. The wavelength of the laser is 750 nm and the peak temporal intensity of the laser pulse at the entrance to the medium ($z = 0$) is 10^{15}W/cm^2. These parameters correspond to the conditions typical of current HHG experiments. The quantum dipole model which includes the HHG contributions from secondary-return electrons has been used to calculate the nonlinear polarization.

Figure 2.18 shows the spatial profiles of the 55th harmonic intensity obtained at four different times near $z = 20$, 100, 200 and 400 μm. Also shown are the corresponding spatial profiles of the driving intensity and the electron density at these times. For $z < 200$ μm, it is seen that as the the harmonic field propagates, its leading edge keeps growing while the trailing edge saturates. This results in the harmonic field having a very narrow spatial extent at $z = 200$ μm, implying a single ultra-short XUV pulse. However, at $z > 200$ μm, even the leading edge of the harmonic pulse saturates and the ultra-short harmonic pulse appears to break up into even finer structures.

The shortening of the harmonic pulse can be more clearly seen from Figure 2.19 which shows the temporal and spectral profiles of the harmonic field obtained at four different locations ($z = 5$, 100, 200 and 400 μm). At $z = 5$ μm, the harmonic temporal profile resembles that obtained in single-atom analysis, showing the interference pattern caused by harmonic contributions from different electron trajectories. At larger distances, the interference pattern disappears. At $z = 200$ μm, the 55th harmonic is a single pulse with a temporal duration of about 5 fs. At still larger distance, the harmonic pulse breaks up into sub-pulses again. From the spectral profiles, it is seen that the HHG contribution from the secondary-return electrons seems to saturate very early compared to the contribution from the first-return pre-3.17 and post-3.17 electrons. This is evidenced by the disappearance of the more blue shifted structure to the right of the two main pre-3.17 and post-3.17 peaks. Furthermore, it is seen that the pre-3.17 and post-3.17 lines seem to "collapse" into one single line

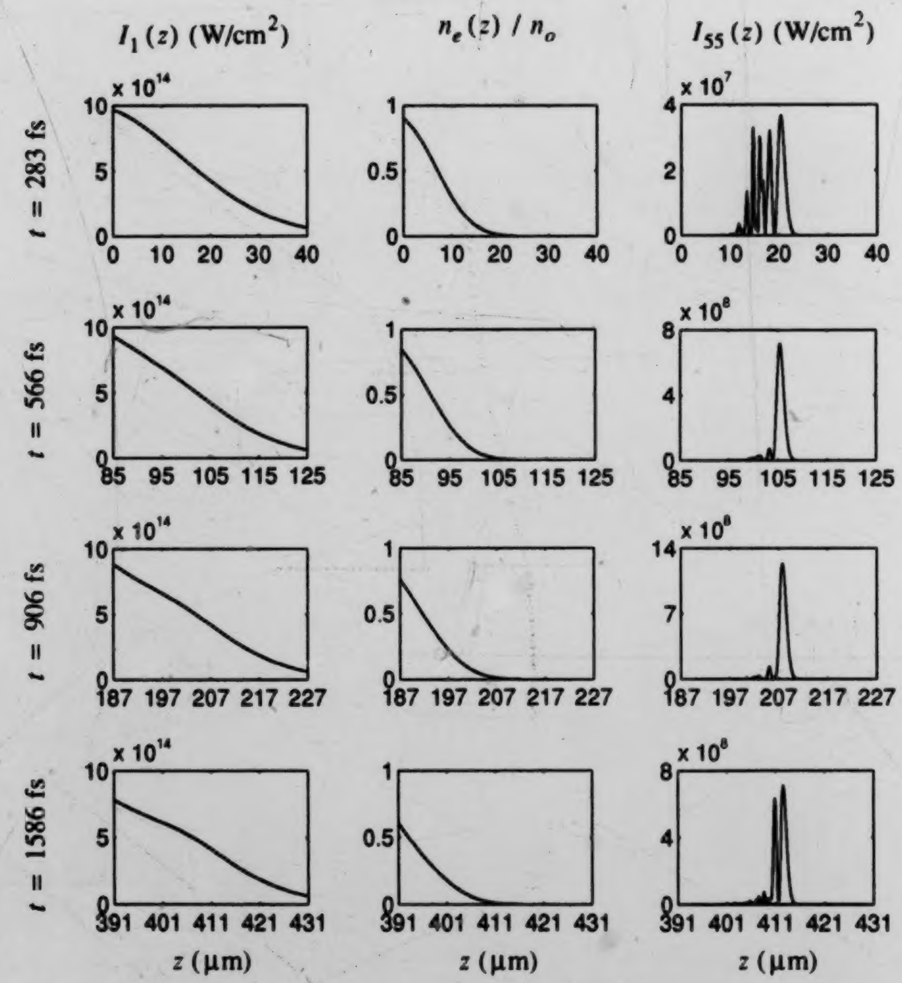

Figure 2.18: Spatial profiles of the driving intensity, I_1, the electron density, n_e, and the 55th harmonic intensity, I_{55}, recorded at t = 283 fs, 566 fs, 906 fs and 1586 fs. Direction of propagation is in the positive z direction. The medium has a background density of n_o = 500 torr.

centered at a frequency midway between the original pre-3.17 and post-3.17 lines. By comparing the temporal and the corresponding spectral profiles at $z = 200\ \mu m$, it is seen that the harmonic pulse is a transform-limited pulse. At $z > 200\ \mu m$, the spectral line starts to split again.

Shown in Figure 2.20 are the temporal and spectral profiles of the 85th harmonic. Similar to the 55th harmonic, the 85th harmonic field becomes a single ultra-short pulse at some distance and breaks up afterwards. From the spectral profiles, it is seen that the 85th harmonic saturates at about $z = 5\ \mu m$, a much smaller saturation distance than for the 55th harmonic. However, similar to the 55th harmonic, the harmonic pulse becomes transform-limited at the saturation distance and the spectral line starts to split again after the saturation distance.

A comparison of the 55th and 85th harmonic conversion efficiency is shown in Figure 2.21. The harmonic energy is obtained by integrating the harmonic intensity temporal profile at the specific locations. Here it is seen that, as compared to the 55th harmonic, the 85th harmonic saturates at a much smaller propagation distance with a much lower peak conversion efficiency.

Explanation of pulse shortening and saturation

The shortening and saturation of the harmonic wave can be explained by the phase difference or phase mismatch between the harmonic wave generated in one region and that generated in another region in the medium. In a 1-D geometry, such a phenomenon is well understood for harmonic conversion from a steady state, low intensity driving field propagating in a medium with constant dispersion [13]. The phase mismatch is due to the phase velocity mismatch between the driving and harmonic waves in the dispersive medium. In the case of a plasma with constant density n_e, the phase mismatch for the qth harmonic is given by:

$$\Delta\theta_q(z) = \frac{qk_o z}{2}\left(1 - \frac{1}{q}\right)\frac{n_e}{n_c} \tag{2.80}$$

---

[13] For example, see [17].

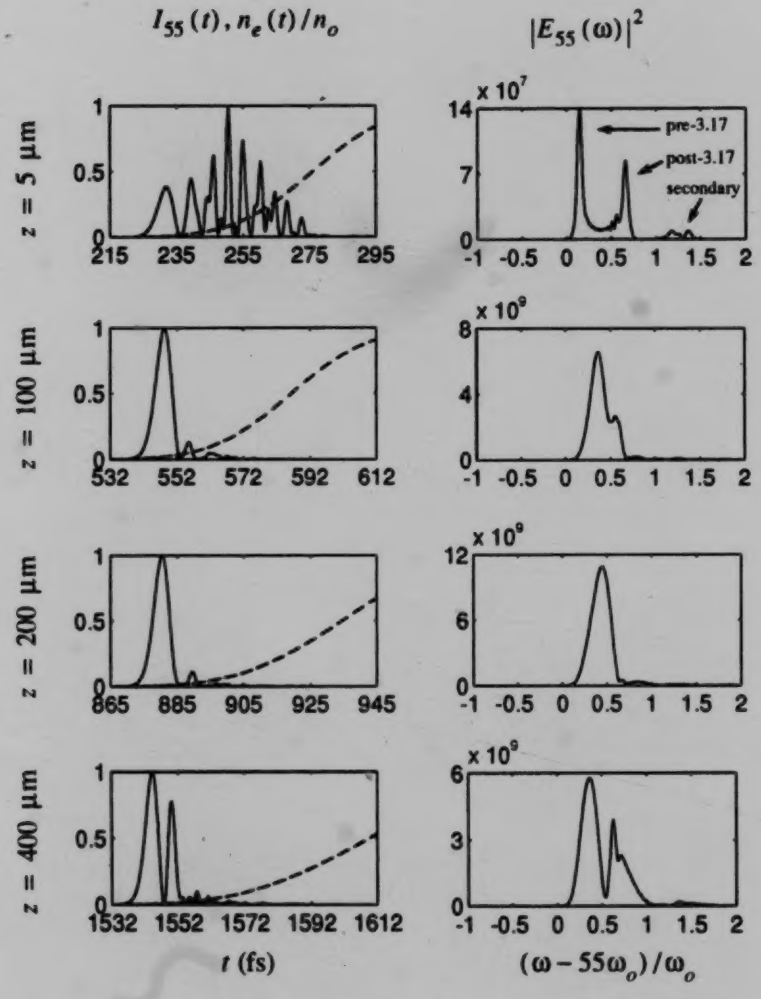

Figure 2.19: Temporal and spectral profiles of the 55th harmonic intensity recorded at $z = 5$ μm, 100 μm, 200 μm, and 400 μm. The dashed lines denote the temporal electron density profiles recorded at these locations.

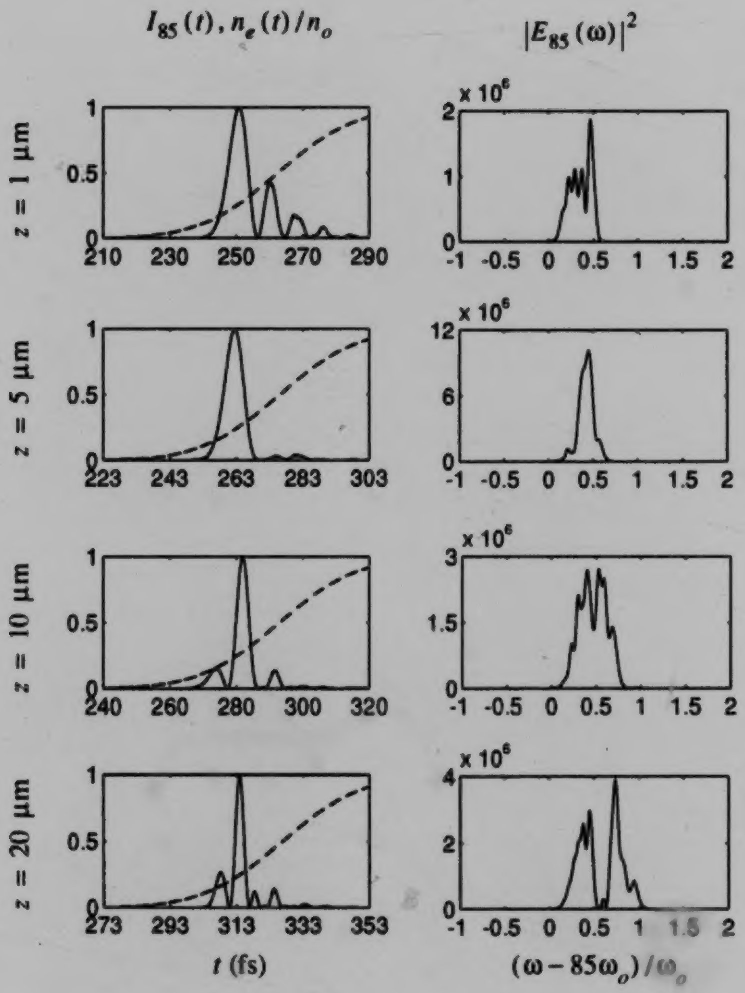

Figure 2.20: Temporal and spectral profiles of the 85th harmonic intensity recorded at $z = 1$ μm, 5 μm, 10 μm, and 20 μm. The dashed lines denote the temporal electron density profiles recorded at these locations

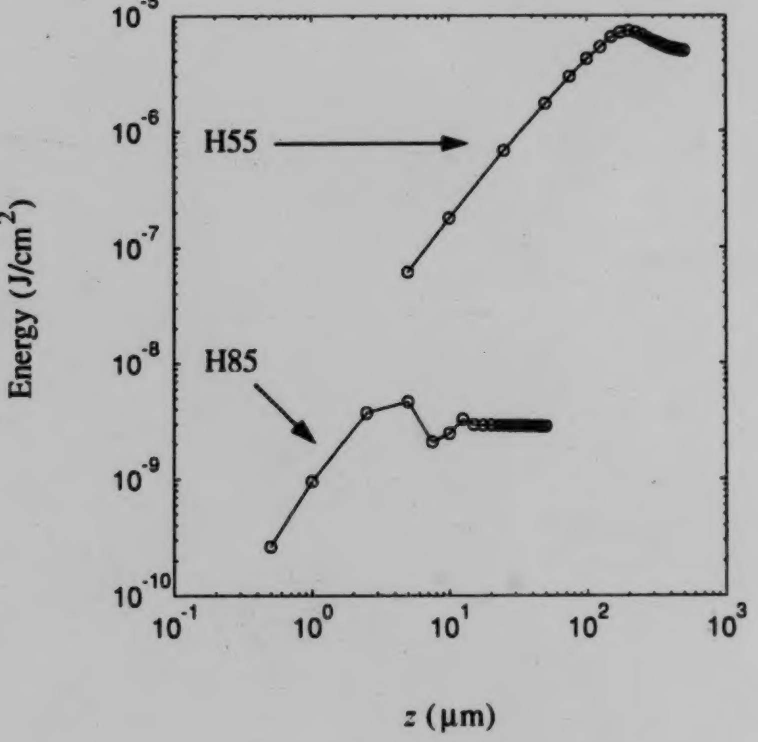

Figure 2.21: The energy of the 55th and 5th harmonics. The circles denote the discrete locations at which the harmonic energy is calculated.

and the intensity of the qth harmonic is given by:

$$I_q = 16\pi^2 q^2 (k_o z)^2 P_q^2 \mathrm{sinc}^2\left(\frac{\Delta\theta_q}{2}\right) \tag{2.81}$$

where P_q in this case is the steady state or constant nonlinear polarization induced by the steady state driving field. From Eqn. (2.81) and the property of the sinc^2() function, it is seen that due to phase mismatch, the harmonic wave generated by P_q can only grow up to a distance z_s at which $\Delta\theta_q(z_s) = \pi$. For $z > z_s$, the harmonic saturates. It is also seen that the larger the phase mismatch, the shorter the saturation distance z_s is and the smaller is the maximum achievable harmonic intensity $I_q(z_s)$.

In the present case of a high intensity, pulsed driving field traveling in a medium with spatially and temporally varying dispersion (which is due to the spatially and temporally dependent ionization), effects of phase mismatch can be understood as follows. First, if group velocity and higher order dispersion of the driving and harmonic fields are small, the second derivatives in the the coupled wave equations, Eqn. (2.71) and Eqn. (2.72), can be neglected:

$$\frac{\partial E_1}{\partial z} + \frac{1}{c}\frac{\partial E_1}{\partial t} + i\frac{k_o}{2}\frac{n_e}{n_c}E_1 = 0 \tag{2.82}$$

$$\frac{\partial E_q}{\partial z} + \frac{1}{c}\frac{\partial E_q}{\partial t} + i\frac{k_o}{2q}\frac{n_e}{n_c}E_1 = i2\pi q k_o P_q \tag{2.83}$$

Now, further assuming the ionization front is propagating approximately undistorted at the speed of light:

$$n_e(z,t) \approx n_e(z-ct) \tag{2.84}$$

the solutions to Eqn. (2.82) and Eqn. (2.83) can be obtained in the retarded frame ($z' = z$ and $t' = t - z/c$) as:

$$E_1(z',t') = E_o(t')\exp\left[-i\frac{k_o}{2}\frac{n_e(t')}{n_c}z'\right] \tag{2.85}$$

$$E_q(z',t') = i2\pi q k_o \exp\left[-i\frac{k_o}{2q}\frac{n_e(t')}{n_c}z'\right]\int_o^{z'} d\xi' P_q(\xi',t')\exp\left[i\frac{k_o}{2q}\frac{n_e(t')}{n_c}\xi'\right] \tag{2.86}$$

where $E_o(t')$ and $n_e(t')$ are the laser envelope and electron density profile at $z' = 0$. From Eqn. (2.74), Eqn. (2.84) and Eqn. (2.85), it is seen that the qth harmonic polarization P_q can be written as:

$$\begin{aligned} P_q(z',t') &= \exp\left[-i\frac{k_o}{2}\frac{n_e(t')}{n_c}z'\right](1-P(t'))\int_o^{2\pi} dt''d(|E_1(t')|cos(\omega_o t''),t'')e^{iq\omega_o t''} \\ &= \exp\left[-i\frac{k_o}{2}\frac{n_e(t')}{n_c}z'\right]P_q(z'=0,t') \end{aligned} \tag{2.87}$$

Hence, the $P_q(z',t')$ here is just equal to the qth harmonic polarization at $z' = 0$ times a phase factor. Finally from Eqn. (2.87) and Eqn. (2.86), the qth harmonic intensity is given by:

$$I_q(z',t') = 16\pi^2 q^2 (k_o z')^2 P_q^2(z'=0,t')\mathrm{sinc}^2\left(\frac{\Delta\theta_q(z',t')}{2}\right) \tag{2.88}$$

where the qth harmonic phase mismatch is now given by:

$$\Delta\theta_q(z',t') = \frac{qk_o z'}{2}\left(1-\frac{1}{q}\right)\frac{n_e(t')}{n_c} \tag{2.89}$$

By comparing Eqn. (2.88) and Eqn. (2.89) with Eqn. 2.81) and Eqn. 2.80), it is seen that the only difference in the dynamic case is that P_q, n_e and therefore $\Delta\theta_q$ are now a function of the retarded time t'. Consequently, the harmonic wave generated at a different portion of $P_q(t')$ will experience difference phase mismatch. Specifically, the portion of the harmonic wave that is generated at a low electron density will see a very small phase mismatch and can therefore grow over a very long distance. On the other hand, the portion of the harmonic wave that is generated at a high electron density will see a very large phase mismatch and therefore saturates in a very short distance. This is consistent with the simulation results which show that the leading edge of the harmonic wave, which is generated at a lower electron density, grows over a longer distance than the trailing edge of the harmonic wave which is generated at a high electron density and which saturates very early. A quantitative comparison is given in Figure 2.22 and Figure 2.23. Here, the analytical results are obtained from Eqn. (2.88) with P_q calculated for the incident laser pulse at the entrance to the medium. It is seen that the analytical results agree very well with the simulation results. Consequently, the initial shortening of the harmonic pulse is due to the larger free electron induced phase mismatch experienced by the trailing portion of the harmonic pulse as compared to that experienced by the leading portion of the harmonic pulse.

Now, since even the leading edge of the harmonic pulse is generated at non-zero electron density, it will also eventually saturate due to non-zero phase mismatch. For very large distances, the phase mismatch which is proportional to $n_e(t')z'$ can vary quite significantly for only a very small change in electron density. Therefore, even the leading edge of the harmonic pulse which is generated in slightly different electron densities can experience large differences in phase mismatch. As a result, the portion which experiences $\Delta\theta_q = 2\pi$ will vanish while other portions will remain. This is then manifested as pulse break up. When the leading edge of the harmonic pulse saturates, the overall harmonic energy conversion also saturates. This has been verified by simulation results which show that breaking up of the ultra short harmonic pulse indeed starts to occur when the overall energy conversion starts to decrease.

The different saturation lengths for the 55th and 85th harmonics can be explained as follows. A particular harmonic can only be generated when the intensity is high enough such that the re-collision electrons can provide the necessary recombination energy. Therefore the leading edge of a harmonic pulse should be located near the driving intensity where $q\hbar\omega_o = I_p + 3.17\ U_p(I_1)$. As a result, the leading edge of lower order harmonics is located at a lower driving intensity while that of the higher order harmonics is located at a higher driving intensity. Now, since higher driving intensity implies higher ionization level and higher electron density, the leading edge of the 85th harmonic sees a larger free electron induced phase mismatch than the 55th harmonic. Therefore the 85th harmonic should saturate much earlier. From Figure 2.19 and Figure 2.20, it is clearly seen that the leading edge of the 85th harmonic is generated at a much higher ionization level than that of the 55th harmonic.

The collapse of the pre-3.17 and post-3.17 harmonic lines can be understood as follows. For small distances, the harmonic wave is just proportional to the polariza-

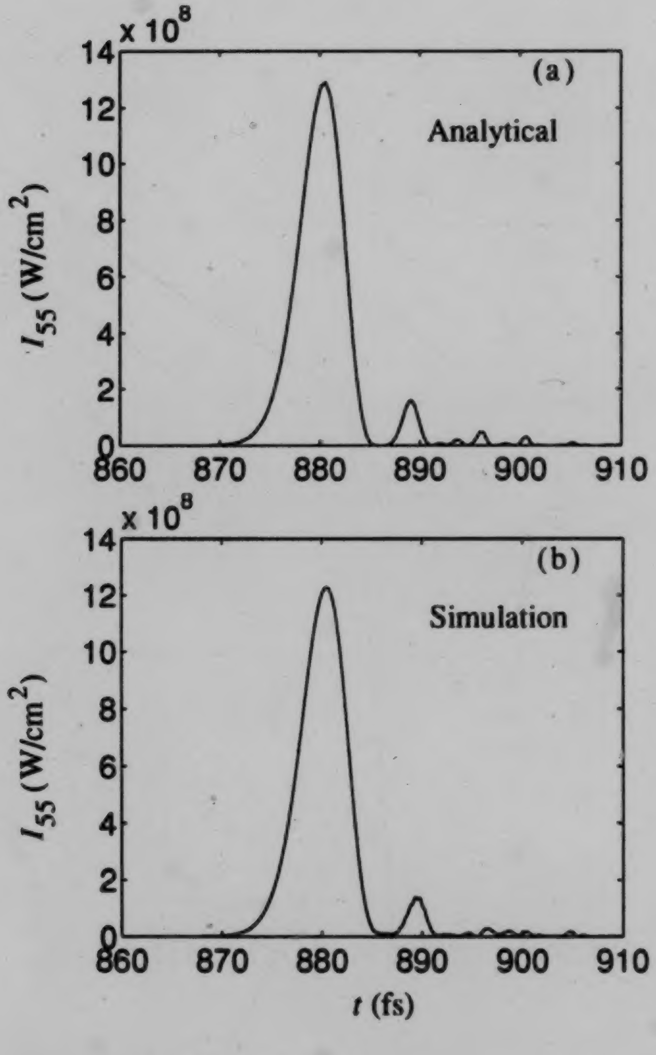

Figure 2.22: Temporal profiles of the 55th harmonic intensity at $z = 200$ μm as obtained by (a) analytical and (b) simulation calculations.

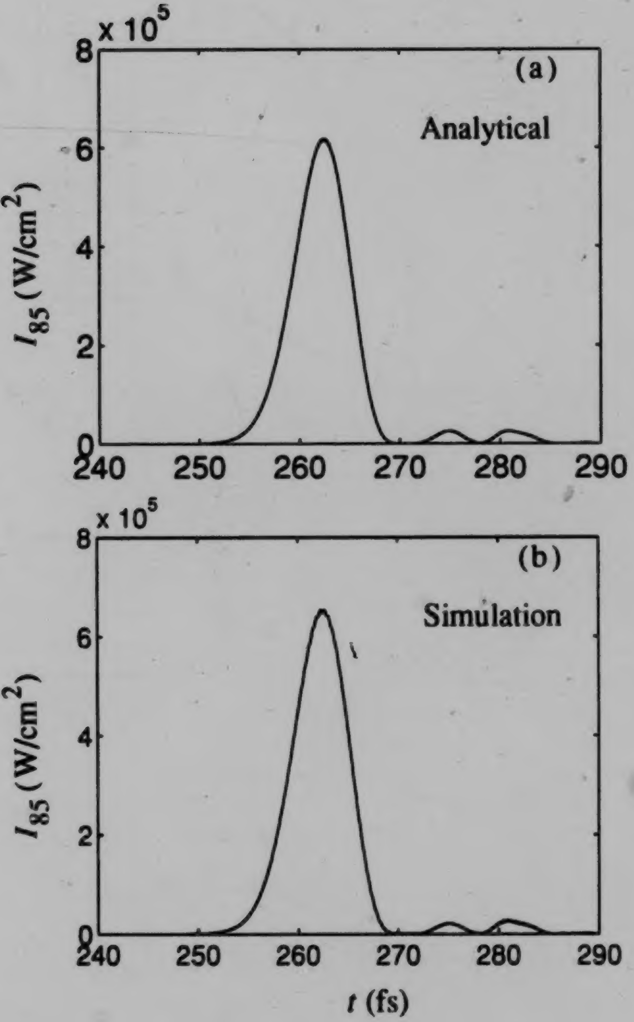

Figure 2.23: Temporal profiles of the 85th harmonic intensity at $z = 200\ \mu$m as obtained by (a) analytical and (b) simulation calculations.

tion current $P_q = n_o d_q$. Hence, the harmonic spectrum should resemble that of the single atom spectrum. As the harmonic propagates, only the leading edge which is generated near the cutoff driving intensity at which $q\hbar\omega_o = I_p + 3.17\ U_p(I_1)$ survives. At this intensity, the phase dependence of the pre-3.17 and post-3.17 components on the driving intensity becomes the same (see Figure 2.17). Physically, this is due to the fact that at the cutoff intensity, electrons which have the required energy to generate the harmonic originate from a single trajectory. As a result, the splitting of the harmonic line due to the degenerate harmonic phase disappears. Now, since the harmonic phase at the cutoff intensity is still an increasing function of driving intensity, the spectral profile of the phase-matched harmonic wave will appear as a single blue-shifted line.

Finally, the early saturation of the harmonic contribution from the secondary-return electrons can be explained as follows. It can be shown by numerically solving the equations of motion (see Section 2.1.2) that the cutoff law for these electrons is $q\hbar\omega_o \approx I_p + 2\ U_p$. Therefore, the harmonic contribution from these electrons will be generated at a higher driving intensity and therefore higher electron density. Hence, the harmonic contribution from secondary-return electrons sees a larger phase mismatch than the that from first-return electrons and therefore saturates earlier.

2.3 Summary and Conclusions

In this study, a number of important characteristics of HHG have been found. First, it has been found that harmonic spectral lines are intrinsically blue shifted and can have very large line width under current experimental conditions. The origin of the blue shifting and line broadening has also been identified. They are due to a degenerate intensity dependent phase arising from harmonic contribution from different electron trajectories. In addition, it has been found that mid-plateau harmonics can be generated rather efficiently at very low ionization levels and can have a temporal duration of only a few femtoseconds.

Chapter 3

High Order Difference Frequency Mixing

As was shown in the last chapter, because HHG occurs only in a relativistic ionization front, the conversion efficiency is severely limited by free electron induced phase mismatch which prevents the growth of the high frequency fields over an extended distance. Recently, it has been proposed that high order difference frequency mixing (HDM) of the type $\omega_{ql} = q\omega_o - l\omega_c$ ($\omega_o \gg \omega_c$, $q \gg l \geq 1$) may be a more attractive means of producing very high frequency fields in a low density plasma [38, 39]. In Refs.[38, 39], it is shown under a number of general considerations [1] that phase matching may be achieved for the high frequency mixed field (ω_{ql}) by choosing appropriate frequencies for the two incident fields (ω_o and ω_c). The phase matching condition is shown to be independent of electron density which implies that even if the high frequency mixed field were produced in an ionizing environment (as in the case of HHG), it could be equally phase-matched across the ionization front.

In this chapter, a specific investigation [2] has been carried out to examine HDM in the strong field regime [3] where HHG can also take place. As in Chapter 2, the present analysis is divided into two parts. The first is concerned with the atomic dipole response to the incident driving field which now consists of two frequency components (ω_o and ω_c) . The second is concerned with the propagation of all the participating waves including the high frequency mixed field and the two incident fields. In this study, the mixed field atomic response is obtained from an extension of the the recombination dipole model discussed in Chapter 1 and propagation effects are studied by using a one dimensional propagation model similar to that used in Chapter 1. The remainder of this chapter is organized as follows: Section 3.1 describes the proposed HDM phase matching condition; Section 3.2 describes the mixed field dipole response; Section 3.3 describes the one dimensional propagation model and presents the calculated results; and Section 3.4 summarizes the findings and conclusions of this study.

---

[1] These will be discussed in the next section.

[2] A version of this study has been published in "Phase-matched frequency conversion in ionizing atomic gases", Physical Review A54, R1026 (1996), by C. Kan, C. E. Capjack, R. Rankin, T. Brabec and N. H. Burnett.

[3] That is, when the driving field strength is comparable to the intra-atomic field strength.

3.1 The HDM Phase Matching Condition

In Refs.[38, 39], the phase matching condition is obtained under the following assumptions. First, it is assumed that the nonlinear polarization induced by the two incident fields can be expanded as $\underline{P}(\underline{E}_1, \underline{E}_c, t) = \sum_{q,l} \tilde{P}_{ql} \exp[-i(q\omega_o - l\omega_c)t]$ where $\underline{E}_1 = E_1 \cos(\omega_o t - \theta_1)$ and $\underline{E}_c = E_c \cos(\omega_o t - \theta_c)$ are the incident fields with phases θ_1 and θ_c. Secondly, it is assumed that phase of the ql nonlinear polarization is related to the phases of the two incident fields by $\theta_{ql} = q\theta_1 - l\theta_c$ such that $\tilde{P}_{ql} = P_{ql} \exp[i(q\theta_1 - l\theta_c)]$ where P_{ql} is real. This second assumption has been shown to be valid in the weak field regime [38] or in the strong field regime if the polarization is a local function of the total incident fields, i.e., $\underline{P}(z,t) = f[\underline{E}_1(z,t) + \underline{E}_c(z,t)]$ [39]. Finally, it is assumed that the high frequency mixed field is generated in a plasma with a *constant* electron density n_e that is much smaller than the critical densities of the participating fields such that the phases of the these fields can be given by:

$$\theta_1(z) = k_1 z = \frac{\omega_1}{c}\left(1 - \frac{1}{2}\frac{n_e}{n_c^1}\right) z \qquad (3.1)$$

$$\theta_c(z) = k_c z = \frac{\omega_c}{c}\left(1 - \frac{1}{2}\frac{n_e}{n_c^c}\right) z \tag{3.2}$$

where $n_c^{1,c}$ are the critical densities of the incident waves. From these considerations, and assuming the ql mixed field component is given by $\underline{E}_{ql} = E_{ql}\exp[i(k_{ql}z - \omega_{ql}t)]$ where $k_{ql} = (\omega_{ql}/c)[1 - (1/2)(n_e/n_c^{ql})]$ and n_c^{ql} is the critical density of the mixed wave, the mixed field envelope in the 1-D limit can be obtained as [17]:

$$E_{ql} = i2\pi\frac{\omega_{ql}}{c}\int dz P_{ql} e^{-i\Delta\theta_{ql}(z)} \tag{3.3}$$

where the phase mismatch is given by:

$$\Delta\theta_{ql} = \theta_{ql} - (q\theta_1(z) - l\theta_c(z)) \tag{3.4}$$

and

$$\theta_{ql} = k_{ql}z = \frac{\omega_{ql}}{c}\left(1 - \frac{1}{2}\frac{n_e}{n_c^{ql}}\right) z \tag{3.5}$$

is just the phase of the high frequency mixed wave. Substituting Eqn. (3.1), Eqn. (3.2) and Eqn. (3.5) into Eqn. (3.4), the phase mismatch becomes:

$$\Delta\theta_{ql} = \frac{\omega_{pe}^2}{4\pi c^2} z\,(q\lambda_o - l\lambda_c - \lambda_{ql}) \tag{3.6}$$

where

$$\lambda_{ql} = \frac{\lambda_o\lambda_c}{q\lambda_c - l\lambda_o} \tag{3.7}$$

Here ω_{pe} is the plasma frequency and λ_{ql} is the wavelength of the mixed wave. Eqn (3.6) then suggests a way of phase-matching the mixed field (ω_{ql}) by choosing appropriate frequencies or wavelengths for the incident fields. For the phase matching of very high frequency mixed field such that $\omega_{ql} = q\omega_o - l\omega_c$, $\omega_o > \omega_c$, $q \gg l$, the phase matching condition becomes

$$\lambda_c = \frac{q}{l}\lambda_o \ (q \gg l) \tag{3.8}$$

This implies that the HDM scheme can be implemented with a high frequency field ω_o and a much lower frequency control field ω_c such that $\omega_o \;/\; \omega_c = q \;/\; l \ (q \gg l)$

A nice feature of this phase matching condition is that it does not depend on the electron density. Therefore, if the high frequency mixed field is generated in an ionizing front (as in the case of HHG) and if the phase matching condition is still valid in such an environment, the mixed field can conceivably be phase-matched across the entire ionization front.

3.2 The Mixed field Atomic Response

The first step in examining the HDM scheme is to understand the behavior of the mixed field nonlinear polarization or, equivalently, the mixed field atomic dipole moment. In this investigation, the recombination dipole model (see Section 2.1) which has been used to study HHG is used to study the HDM atomic response.

3.2.1 Preliminary analysis

A preliminary understanding of the mixed field dipole moment can be obtained from the following analysis using the semi-classical dipole model. Here, it is assumed that the amplitude and frequency of the control field, $\underline{E}_c$, are much lower than those of the high frequency field, $\underline{E}_1$, such that (1) the induced dipole moment is mainly due to the high frequency field, (2) the role of the control field is only to perturb the accumulated phase of the electron wavefunction, (3) the real amplitude of the control field can be considered constant in one laser cycle of the high frequency field, and (4) the control field does not affect the recombination time of the re-colliding electrons.

From these assumptions, the mixed field dipole moment can be written as:

$$d(t) = d_o(t)e^{-i(S_1+S_2)} \tag{3.9}$$

where d_o is the semi-classical dipole moment obtained for the high frequency field alone and the perturbed accumulated phases are given by:

$$S_1 = -16\pi^2\left(\frac{U_p}{\hbar\omega_o}\right)\left(\frac{E_c}{E_o}\right)\int_{t'/t_o}^{t/t_o} d(t''/t_o)\left(\sin(\omega_o t'') - \sin(\omega_o t')\right)\omega_o(t''-t') \tag{3.10}$$

$$S_2 = 16\pi^3 \left(\frac{U_p}{\hbar\omega_o}\right)\left(\frac{\underline{E}_c}{E_o}\right)^2 \int_{t'/t_o}^{t/t_o} d(t''/t_o)\omega_o(t''-t') \tag{3.11}$$

Here U_p is the ponderomotive potential in the high frequency field, $\underline{E}_c$ is the real amplitude of the control field, and E_o is the envelope of the high frequency field. Eqn. (3.10) and Eqn. (3.11) are obtained by calculating the accumulated phase (Eqn. (2.24)) for a field $\underline{E} = E_o\cos(\omega_o t) + \underline{E}_c(t)$ and using assumption (3) discussed above.

By using the stationary phase approximation and by ignoring the higher order perturbed phase S_2 which is proportional to $(\underline{E}_c/E_o)^2$, the envelope of the qth harmonic dipole moment is given by:

$$d_q = \frac{1}{2}d_{qo}(t_q)\left[e^{iS_1(t_q)} - e^{iq\pi}e^{-iS_1(t_q)}\right] \tag{3.12}$$

where d_{qo} and t_q are respectively the envelope of the qth (q = odd) harmonic dipole component and the recombination time when there is no control field. It is seen from Eqn. (3.12) that unlike harmonic generation where only odd harmonic components exist, the mixed field dipole moment can contain even harmonic components. By substituting $\underline{E}_c = E_c\cos\omega_c t$ into Eqn. (3.12) and using the relation [48] $\exp(ix\cos\theta) = \sum_l (i)^l J_l(x)\exp(-il\theta)$ where J_l is the the l-order Bessel function, the dipole envelope becomes:

$$d_q = \frac{1}{2}d_{qo}(t_q)\sum_{l=-\infty}^{l=\infty}(i)^l\left[J_l(\alpha) + J_l(-\alpha)\right]e^{-il\omega_c} \tag{3.13}$$

where

$$\alpha = -16\pi^2\left(\frac{U_p}{\hbar\omega_o}\right)\left(\frac{E_c}{E_o}\right)\int_{t'/t_o}^{t/t_o} d(t''/t_o)\left(\sin(\omega_o t'') - \sin(\omega_o t')\right)\omega_o(t''-t') \tag{3.14}$$

Therefore, it is seen that there exist sub-band components with frequencies $l\omega_c$ associated with each harmonic components. Moreover, from the symmetry of the Bessel functions [48]:

$$\begin{aligned} J_l(\alpha) &= J_l(-\alpha), \quad (l = \text{even}) \\ J_l(\alpha) &= -J_l(-\alpha), \quad (l = \text{odd}) \end{aligned} \tag{3.15}$$

it is seen that only $l =$ even sub-band components exist for $q =$ odd and only $l =$ odd sub-band components exist for $q =$ even.

The saturation of the mixed field components can be estimated by examining the first maxima of the Bessel functions. For the l order Bessel function, the first maximum occurs at approximately $\alpha_{max} \approx l(\pi/2)$. Therefore, the mixed field components will saturate when

$$\frac{E_c}{E_o} \approx l\frac{\pi}{2}\left(-16\pi^2\left(\frac{U_p}{\hbar\omega_o}\right)\int_{t'/t_o}^{t/t_o} d(t''/t_o)\left(\sin(\omega_o t'') - \sin(\omega_o t')\right)\omega_o(t'' - t')\right)^{-1} \tag{3.16}$$

and the saturated amplitude of a $q\omega_o - l\omega_c$ component will be:

$$d_{ql}^{max} \approx d_{qo}(t_q)J_l(\alpha_{max}) \tag{3.17}$$

For example, for a high frequency field with a wavelength equal to 400 nm and an intensity equal to 1.5×10^{15} W/cm^2, Eqn. (3.16) and Eqn. (3.17) predict that the saturation amplitudes for the "near" even mixed field components $q\omega_o - l\omega_c$ where $q =$ even are $\approx 0.5d_{qo}$ for $l = 1$ and $\approx 0.4d_{qo}$ for $l = 3$. The saturation occurs at $E_c/E_o \approx 0.02$ for $l = 1$ and $E_c/E_o \approx 0.06$ for $l = 3$. Therefore, this justifies the assumption that $E_c/E_o \ll 1$. In addition, even for such a weak control field, the saturated amplitudes of the mixed field components can be as high as 50% of the amplitude of the nearby odd harmonic component when no control field is present.

3.2.2 Numerical results

Results from numerical evaluation of the recombination dipole moment have been obtained to examine the simple analysis discussed above. Here, the quantum dipole moment (see Section 2.1.4) which makes no specific assumptions regarding the form of the incident field is used to calculate the mixed field dipole moment. Figure 3.1(a) shows the dipole acceleration power spectrum for a 150 fs fundamental pulse interacting with neon. The pulse has a peak intensity of 1.5×10^{15} W/cm^2 and a wavelength of 400 nm. This field can be realized by the second harmonic of a Ti:Sapphire laser. It is seen that under these conditions, the harmonic plateau extends to about the 27th harmonic which has a wavelength of 15 nm. With the addition of a CW control field with a wavelength of 10.4 μm and an amplitude equal to 0.070 of the fundamental field's peak amplitude, many mixed field components appear (see Figure 3.1(b)). The control field wavelength used here is chosen to satisfy the proposed phase matching condition (Eqn. 3.8) for the $26\omega_o - \omega_c$ mixed field and can be realized by a CO2 laser. It should be noted that unlike HHG where only $q =$ odd spectral lines are possible, $q =$ even components can also be seen in the HDM spectrum. This is in agreement with the simple analysis discussed above.

The growth of the mixed field components near the $26\omega_o - \omega_c$ line as function of control field amplitude is shown in Figure 3.2. Here, it is seen that as the control field amplitude is increased, more and more sub-band components ($l\omega_c$) appear. Specifically, for $q =$ odd, only $l =$ even sub-band components exist whereas for $q =$ even, only $l =$ odd sub-band components exist. This again is consistent with the simple analysis discussed above. However, the sub-band components are apparently all blue shifted as is the 25th harmonic in the absence of the control field. As will be discussed below, this is again due to an intensity dependent phase. For $E_{co} = 0.06E_{1o}$, it is seen that the mixed field components $26\omega_o - l\omega_c, l = 1, 3$ have both saturated to a level within an order of magnitude of the 25th harmonic that is generated by the fundamental field alone. This is more clearly shown in Figure 3.3 where the energy of the $25\omega_o$, $26\omega_o - \omega_c$ and $26\omega_o - 3\omega_c$ lines is plotted as function of the control field amplitude. The energy for each component is obtained by integrating the power spectrum in the corresponding spectral range and is normalized with respect to the energy of the 25th harmonic when $E_{co} = 0$. Here, it is seen that the saturated $26\omega_o - \omega_c$ and $26\omega_o - 3\omega_c$ sub-band energies are about 10 % of that of the 25th harmonic produced by the fundamental field alone. Assuming the mixed field energy is proportional to the square of the mixed field amplitude, these results are also in agreement with the results obtained in the simple analysis discussed above.

The temporal profiles of the $q = 26, l = 1, 3$ components at saturation are shown in Figure 3.4. These profiles are obtained by applying an ideal band-pass filter

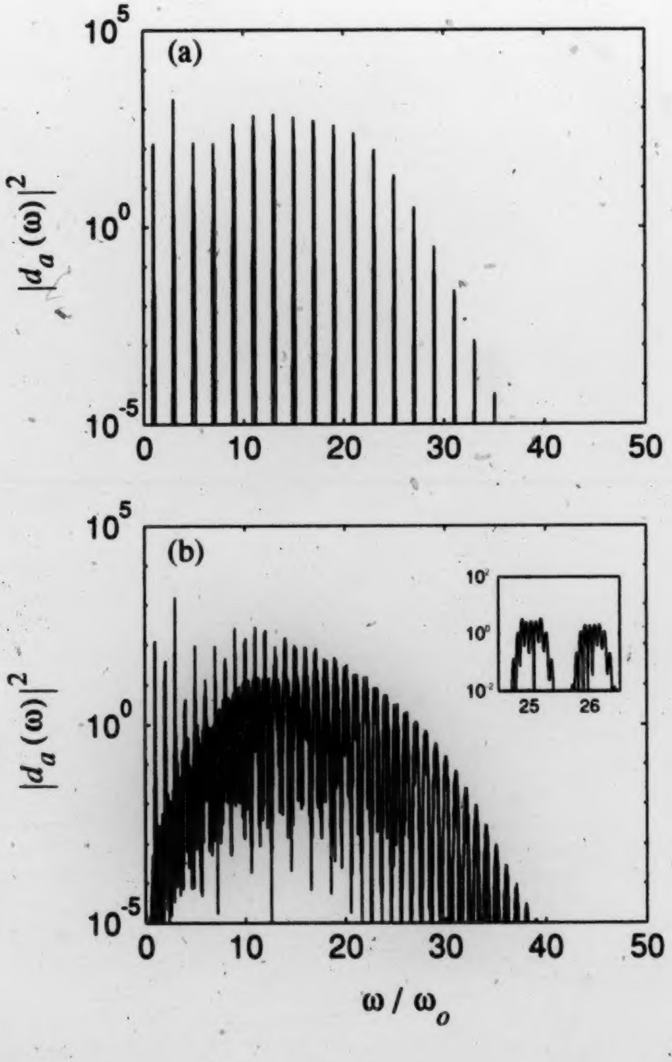

Figure 3.1: (a) Dipole acceleration power spectrum obtained for a 150 fs fundamental pulse interacting with neon. The fundamental pulse has a peak intensity of 1.5×10^{15} W/cm^2 and a wavelength of 400 nm. (b) Dipole acceleration power spectrum obtained for the mixing of a CW control field with the same fundamental pulse used in (a). The control field has a wavelength of 10400 nm and an amplitude equal to 0.070 of the fundamental pulse peak amplitude.

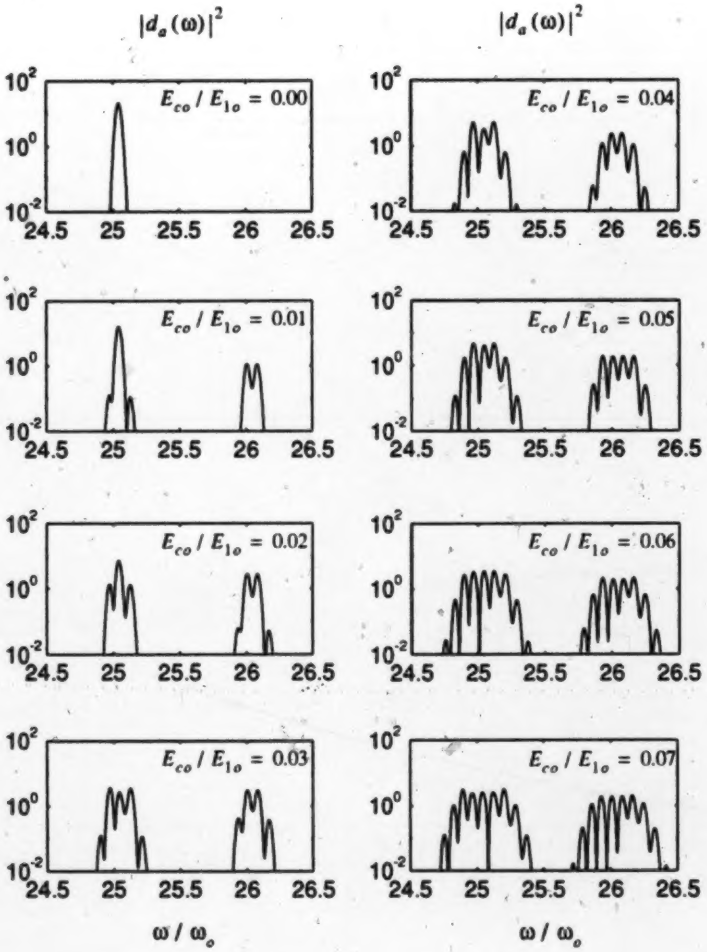

Figure 3.2: Dipole acceleration power spectra near the $26\omega_o - \omega_c$ mixed line obtained for the mixing of the same fundamental pulse used in Figure 3.1 and a CW control field with different amplitudes. E_{co} is the amplitude of the control field and E_{1o} is the peak amplitude of the fundamental pulse.

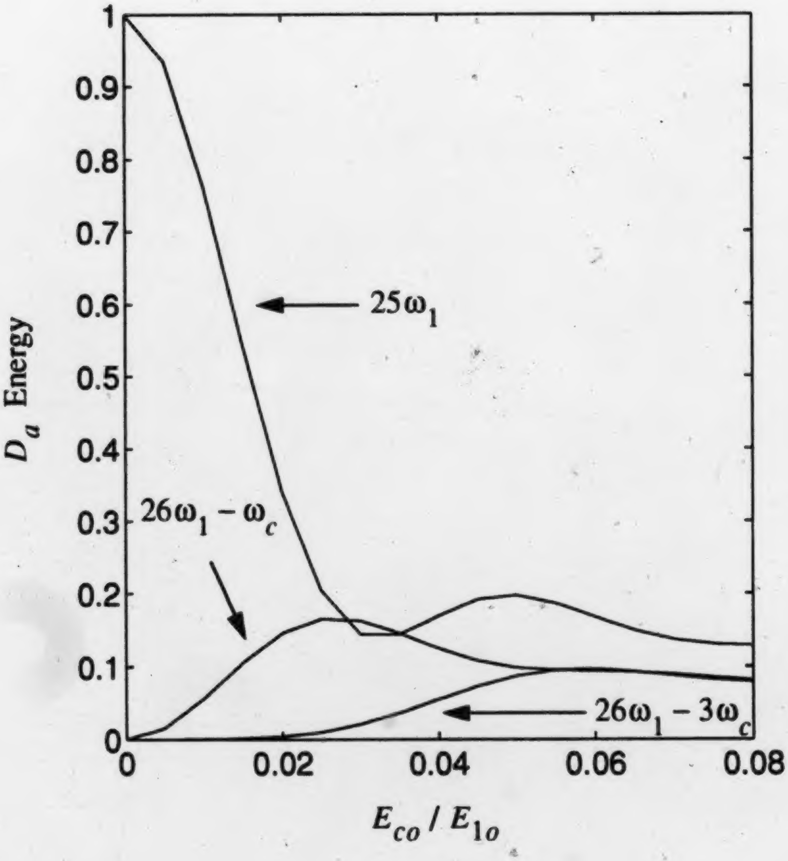

Figure 3.3: Energy of the $25\omega_o$, $26\omega_o - \omega_c$ and $26\omega_o - 3\omega_c$ dipole acceleration components.

to the spectral region corresponding to the mixed lines and performing an inverse Fourier transform. For example, the $26\omega_o - 3\omega_c$ temporal profile has been obtained by isolating the spectral region in the frequency range between $\omega = 25.89\omega_o$ to $\omega = 25.97\omega_o$ in the complex spectrum followed by an inverse Fourier transform. The specific range is obtained by a visual inspection of the spectrum. Also shown are the normalized profiles of the control field amplitude and fundamental intensity and the temporal profile of the ionization probability calculated at $E_{co} = 0$. The ionization probability has been found to change little for the control field amplitude, E_{co}, studied here. From Figure 3.4 , it is seen that the temporal profiles of the mixed fields very closely follow that of the 25th harmonic.

As is evidenced from the spectral blue shifts of the mixed lines, the dipole phase must also have a temporal dependence. This is shown in Figure 3.5. The phase of the mixed field component, $\theta^I_{ql}(t)$, is obtained by assuming that the component varies as $\exp[i(q\omega t - l\omega_c t + \theta^I_{ql}(t))]$. Figure 3.5a shows the phase of the 25th harmonic in the absence of the control field. It is seen that this phase increases with time, thus resulting in a blue shift in the spectral domain. Again, this time dependent phase is due to the dependence of the harmonic phase on the fundamental intensity which is in turn varying in time (see Section 2.1.7). Figure 3.5b and Figure 3.5c show respectively the phases of $26\omega_o - \omega_c$ and $26\omega_o - 3\omega_c$ components at two different values of E_c. It is seen that the temporal dependence very closely follows that of the 25th harmonic and that a change of the amplitude of the control field only causes a small constant phase shift of the mixed field components. This shows that the mixed field dipole phase is a strong function of the fundamental intensity but a rather weak function of the control field amplitude.

Finally, of particular importance in the HDM scheme is the dependence of the dipole moment on the *phases* of the incident fields. By varying the phases of the fundamental (θ_1) and the control field (θ_c), it has been found that for the case studied here the dipole phase is indeed given by $\theta_{ql} = \theta^I_{ql} + q\theta_1 - l\theta_c$ where θ^I_{ql} is the intensity dependence phase discussed above. The magnitudes of the mixed field components,

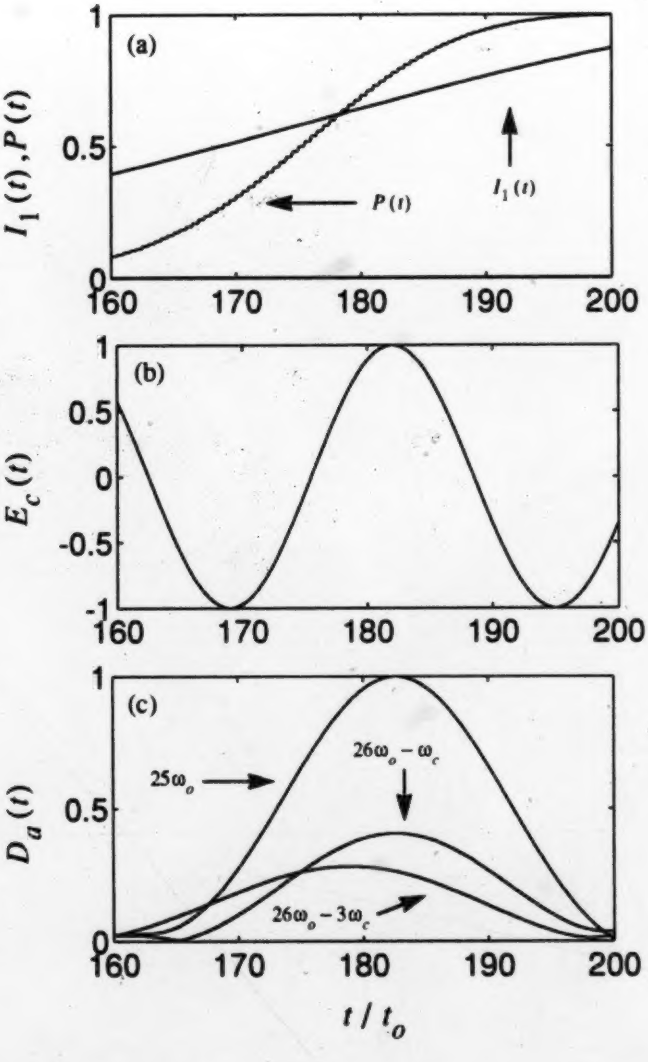

Figure 3.4: (a) The normalized fundamental intensity and the ionization probability calculated in the absence of the control field. (b) The normalized control field profile. (c) Temporal profiles of the 25th harmonic at $E_{co} = 0$, the $26\omega_o - \omega_c$ component at $E_{co} = 0.025\ E_{1o}$ and the the $26\omega_o - 3\omega_c$ component at $E_{co} = 0.065\ E_{1o}$. These fields are normalized with respect to the peak 25th harmonic amplitude.

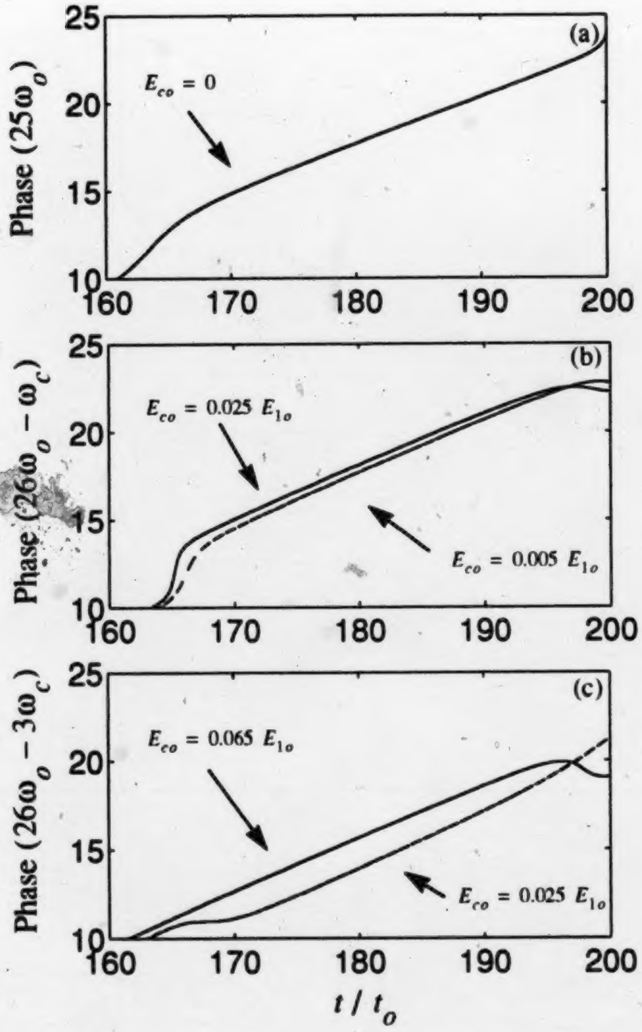

Figure 3.5: (a) Phase (in rad) of the 25th harmonic dipole component in the absence of the control field. (b) and (c) Phases of the $26\omega_o - \omega_c$ and $26\omega_o - 3\omega_c$ components at two different values of E_c.

on the other hand, depend little on the incident phases.

3.3 One Dimension Propagation Study

The 1-D propagation model described in Chapter 2 has been extended to study the proposed HDM scheme. Similar to the HHG model, it is assumed here that the total field inside the medium consists of three fields, i.e. $\underline{E} = \underline{E}_1 + \underline{E}_c + \underline{E}_m$ where $\underline{E}_1$ is the high intensity, high frequency fundamental field, $\underline{E}_c$ is the low intensity, low frequency control field and $\underline{E}_m$ is the mixed field generated by the induced mixed field nonlinear polarization. It is further assumed that $\underline{E}_1 \gg \underline{E}_c, \underline{E}_m$. Then the 1-D nonlinear wave equation (Eqn. (2.62)) can be partially decoupled into a set of wave equations:

$$\frac{\partial^2 E_1}{\partial z^2} - \frac{1}{c^2}\frac{\partial^2 E_1}{\partial t^2} + \frac{2i\omega_o}{c}\left(\frac{\partial E_1}{\partial z} + \frac{1}{c}\frac{\partial E_1}{\partial t}\right) - \frac{\omega_{pe}^2}{c^2}E_1 = 0 \tag{3.18}$$

$$\frac{\partial^2 E_c}{\partial z^2} - \frac{1}{c^2}\frac{\partial^2 E_c}{\partial t^2} + \frac{2i\omega_c}{c}\left(\frac{\partial E_c}{\partial z} + \frac{1}{c}\frac{\partial E_c}{\partial t}\right) - \frac{\omega_{pe}^2}{c^2}E_c = 0 \tag{3.19}$$

$$\frac{\partial^2 E_q}{\partial z^2} - \frac{1}{c^2}\frac{\partial^2 E_q}{\partial t^2} + \frac{2i\omega_q}{c}\left(\frac{\partial E_q}{\partial z} + \frac{1}{c}\frac{\partial E_q}{\partial t}\right) - \frac{\omega_{pe}^2}{c^2}E_q = -\frac{4\pi\omega_q^2}{c^2}P_q \tag{3.20}$$

where the envelope fields are related to the real fields by:

$$\underline{E}_1(z,t) = |E_1(z,t)|\cos\left(\frac{\omega_o}{c}(z-ct) + \arg(E_1(z,t))\right) \tag{3.21}$$

$$\underline{E}_c(z,t) = |E_c(z,t)|\cos\left(\frac{\omega_c}{c}(z-ct) + \arg(E_c(z,t))\right) \tag{3.22}$$

$$\underline{E}_q(z,t) = |E_q(z,t)|\cos\left(\frac{\omega_q}{c}(z-ct) + \arg(E_q(z,t))\right) \tag{3.23}$$

and the plasma frequency ω_{pe} is calculated from the tunnel ionization equation, taking into account the fundamental field only. In Eqn. (3.20), E_q is the envelope of a *near*-qth mixed field generated by the *near*-qth mixed field nonlinear polarization P_q defined below.

As is seen from the single-atom analysis, since the mixed field dipole spectrum consists of discrete spectral lines, the mixed field nonlinear polarization can be expanded as $P_T(t) = \sum_q \sum_l \tilde{P}_{ql}(t)\exp[i(q\omega_o - l\omega_c)t] = \sum_q \tilde{P}_q(t)\exp[iq\omega_o t]$ where $\tilde{P}_q(t) = \sum_l \tilde{P}_{ql}(t)e^{-il\omega_c t}$. From the single-atom analysis, it is also seen that for the control field strengths studied here, $\tilde{P}_{ql}$ is only significant for small l. Therefore, since $\omega_c \ll \omega_o$, $\tilde{P}_q(t)$ is slowly varying compared to $e^{i\omega_o t}$ and can then be obtained approximately by:

$$\tilde{P}_q(t) = \frac{n_o}{t_o}\int_t^{t+t_o} dt'' e^{-iq\omega_o t''} d(\underline{E}_1(t''), \underline{E}_c(t''), t'') \tag{3.24}$$

where d is the recombination dipole moment induced by the two incident fields. Similar to the HHG model, it is now assumed that the fundamental field envelope and ionization probability do not vary significantly over one fundamental laser cycle t_o. Here it is also assumed that the magnitude of the low frequency control field does not vary significantly in one t_o. Then $\tilde{P}_q$ can be evaluated as:

$$\begin{aligned}\tilde{P}_q(t) &= \frac{n_o}{t_o}(1 - P(t)) \\ &\int_t^{t+t_o} dt'' e^{-iq\omega_o t''} \bar{d}(|E_1(t)|\cos(\omega_o t'' + \arg(E_1)(t)), \underline{E}_c(t), t'')\end{aligned} \tag{3.25}$$

where $\bar{d}$ is the steady state dipole moment obtained by setting $P(t) = 0$ in the dipole expression. Also, as was discussed in Section 2.2.2, the effect of a phase shift in the fundamental field, θ_1, will only change the phase of the qth harmonic components by $q\theta_1$, hence:

$$\tilde{P}_q(t) = \frac{e^{iq\arg E_1(t)}}{t}\int_0^{t_o} dt' e^{-iq\omega_o t''} d(|E_1(t)|\cos(\omega_o t''), \underline{E}_c(t)) \tag{3.26}$$

where the change of the integration limits also follows from the same arguments discussed in Section 2.2.2. Finally, it should be noted that since $P_q = \sum_l P_{ql}e^{-il\omega_c t}$, $E_q = \sum_l E_{ql}e^{-il\omega_c t}$ should also contain the various subband components.

3.3.1 Results and Discussion

The propagation model has been incorporated into a computer simulation code using a similar numerical method as that for the HHG model. The numerical scheme is described in Appendix C. Calculations have been carried out to study the propagation of a 400 nm, 150 fs, ionizing laser pulse with a peak intensity of 1.5×10^{15}W/cm^2 and a much weaker control laser whose amplitude at the entrance to the medium is constant and whose frequency satisfies the HDM phase matching condition for a particular high frequency mixed field with frequency $\omega_{ql} = 26\omega_o - l\omega_c$. The nonlinear medium is 50 torr of neon. Calculations have also been done to obtain results for the neighboring 25th harmonic when there is no control field. These results are used to examine the possible conversion improvement due to HDM.

With no control field, the energy conversion of the 25th harmonic is shown in Figure 3.6. Here, the harmonic energy is obtained by integrating over time the harmonic intensity recorded at specific locations in the medium and is normalized with respect to the maximum energy reached. It is seen that the conversion efficiency saturates at about 100 μm. As expected, the saturation is due to free electron induced phase mismatch. This can be seen from Figure 3.7 where the 25th harmonic temporal profiles recorded at different locations are shown. At $z = 1$ μm, the harmonic profile resembles that from the single atom response (see Figure 3.4). At $z = 100$ μm, the phase mismatch due to free electrons ($\Delta\theta = 0.5q\pi(z/\lambda_o)(n_e/n_c)$) is greater than π for an ionization fraction greater than 60%. Hence a large portion of the harmonic pulse generated at higher ionization saturates and the peak of the harmonic pulse is now "pushed" toward lower electron density. This also results in the overall energy saturation as is indicated from Figure 3.6. At $z = 200$ μm, the phase mismatch at 60% ionization becomes 2π, resulting in zero conversion efficiency in this portion of the harmonic pulse.

The growth of the near-26th ($26\omega_o - \sum_l l\omega_c$) mixed field is shown in Figure 3.8. Plotted are the spectral profiles of the mixed field recorded at various locations in the medium. Here, the control field wavelength has been set to 10.4 μm to phase match the $l = 1$ sub-band component. The control field amplitude at the entrance to the medium has been set to 0.037 of that of the peak fundamental amplitude in order to saturate the atomic response (see Figure 3.3). In Figure 3.8, it is seen that as the

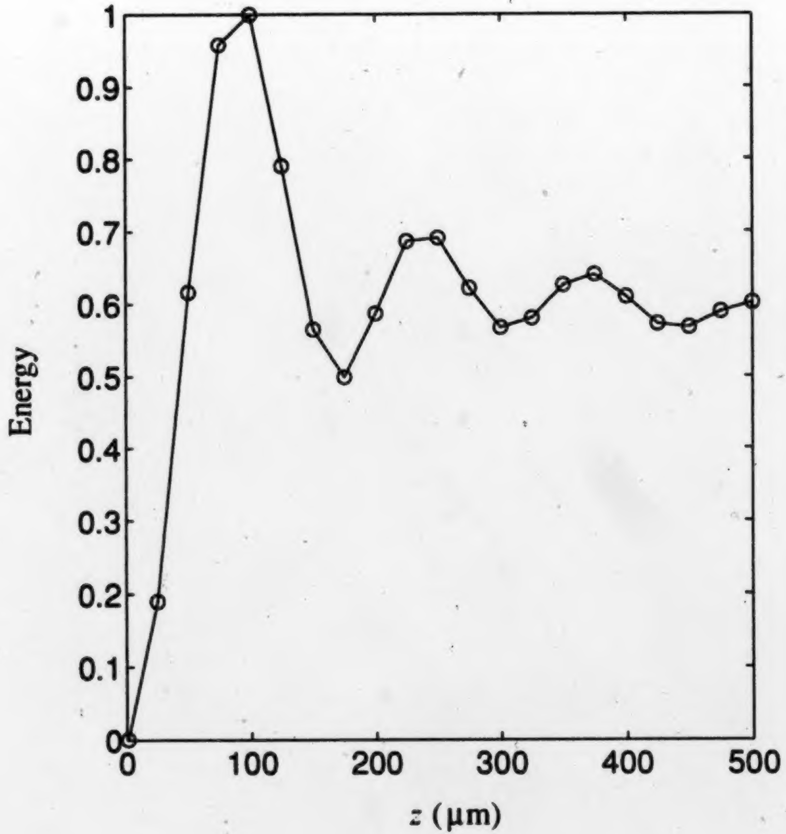

Figure 3.6: The time-integrated energy of the 25th harmonic pulse. The values of the harmonic energy have been calculated at discrete locations as indicated by the circles.

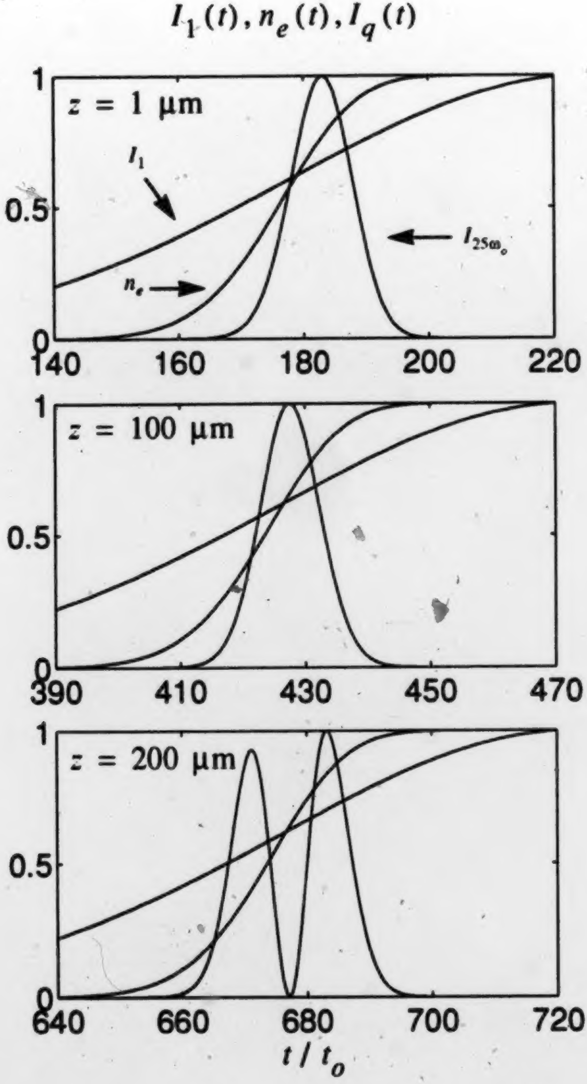

Figure 3.7: The temporal profiles of the 25th harmonic recorded at different locations. Also plotted are the normalized fundamental intensity and the electron density. The electron density has a maximum value of 50 torr corresponding to 100% ionization of the gas.

mixed field propagates, the growth of the non-phase-matched sub-band components saturates rather rapidly. At $z = 100\ \mu m$, the mixed field is composed primarily of the phase-matched $l = 1$ sub-band components. However, at $z = 200\ \mu m$, even the $l = 1$ sub-band ceases to grow. The energy saturation is more clearly seen in Figure 3.9 where the time integrated energy of the near-26th mixed field (including all sub-bands) is plotted as function of propagation distance. Also shown for comparison is the energy of the 25th harmonic when there is no control field (i.e. Figure 3.6). The energy is normalized with respect to the maximum 25th harmonic energy. It is seen that although the near-26th mixed field has a longer saturation length, due to its smaller nonlinear polarizablity (see Figure 3.3) which is responsible for a more gradual growth, the maximum energy obtainable is only 80% that of the 25th harmonic. Hence, no improvement in conversion efficiency has been achieved.

Now since the saturation of the 25th harmonic can be accurately explained by the free electron induced phase mismatch predicted by $\Delta\theta = 0.5k_{1o}zq(n_e/n_c)$, the phase of the fundamental field should well be described by $\theta_1 = k_{1o}(1 - 0.5n_e/n_c)z$. Furthermore, since the electron density in the HDM case is also due to the fundamental intensity alone, the phase of the fundamental field should be the same as that in the HHG case. This implies that the propagated low frequency control field is responsible for the saturation of the mixed field.

Figure 3.10 and Figure 3.11 show respectively the amplitude of the control field near the ionization front at different locations and the temporal profiles of the $l = 3$ sub-band component at the same locations. Also shown in Figure 3.11 are the fundamental and electron density profiles. From these figures, it is seen that the control field has experienced an upshift of its frequency and a reduction in its amplitude. Both the frequency upshift and amplitude reduction are more pronounced in the middle of the ionization front where the high frequency mixed field peaks.

Frequency upshifts of laser pulses co-propagating with a relativistic ionization front have been examined many studies [4]. Physically, the frequency upshifting is a

---

[4] See Ref. [51] and references therein.

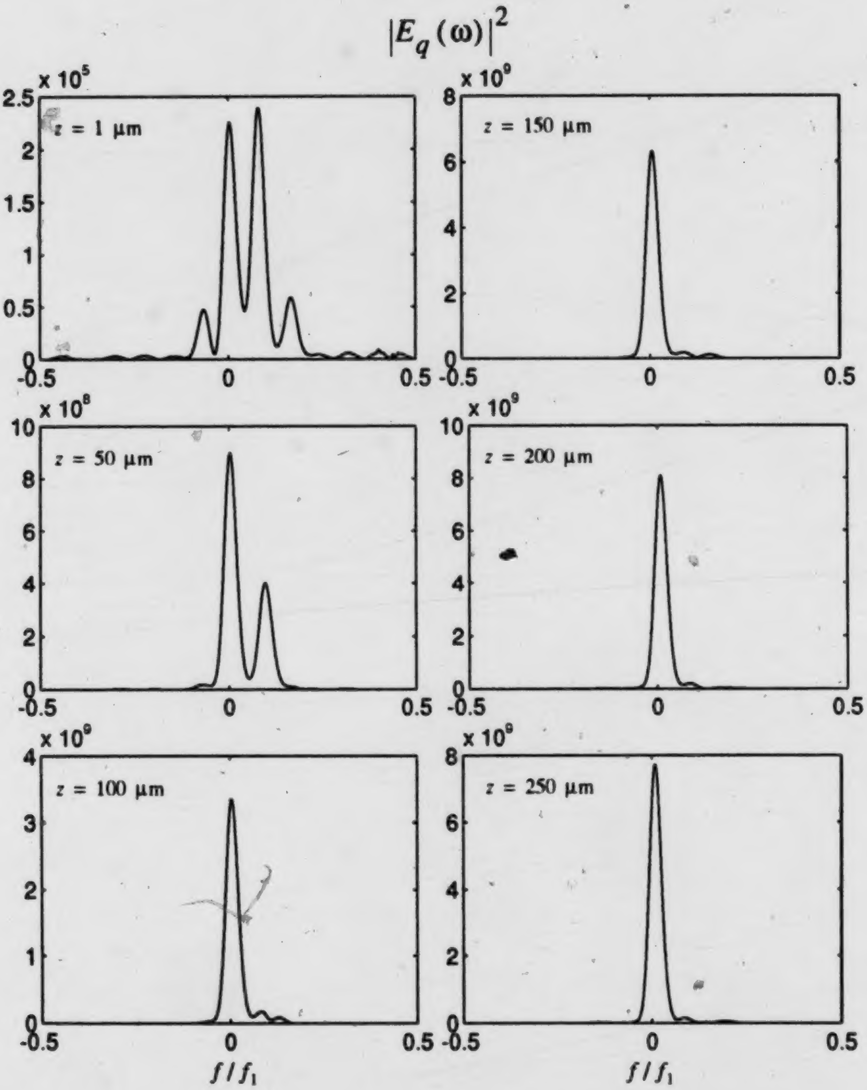

Figure 3.8: Spectral profiles of the near-26 mixed field recorded at different locations in the medium.

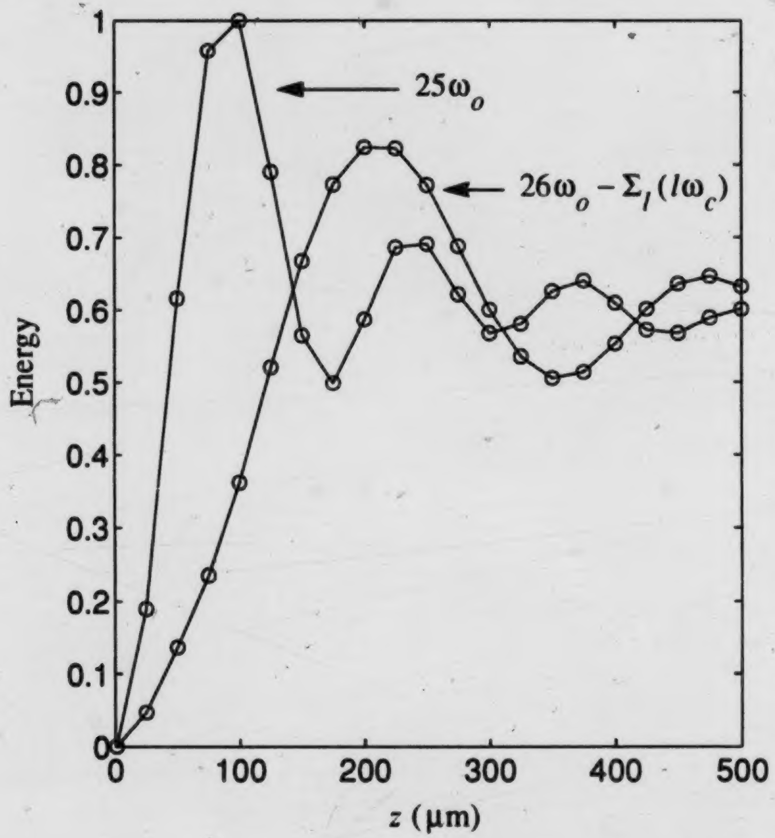

Figure 3.9: Time integrated energy of the near-26th mixed field and the 25th harmonic when there is no control field. The energy is normalized with respect to the maximum 25th harmonic energy.

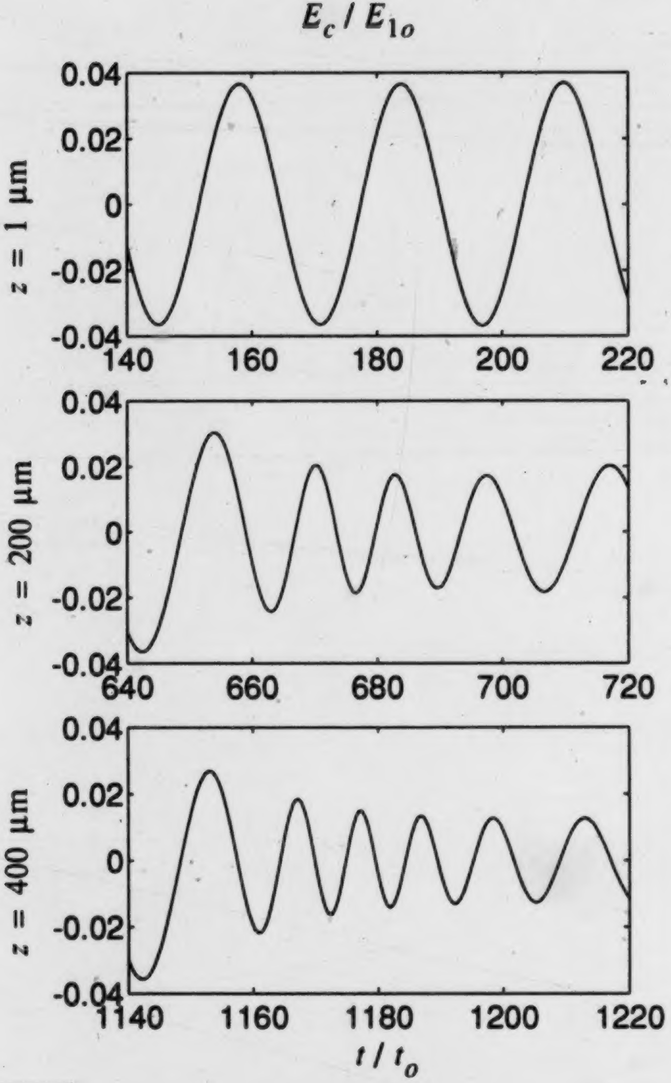

Figure 3.10: Temporal profiles of the low frequency control field near the ionization front recorded at different locations in the medium.

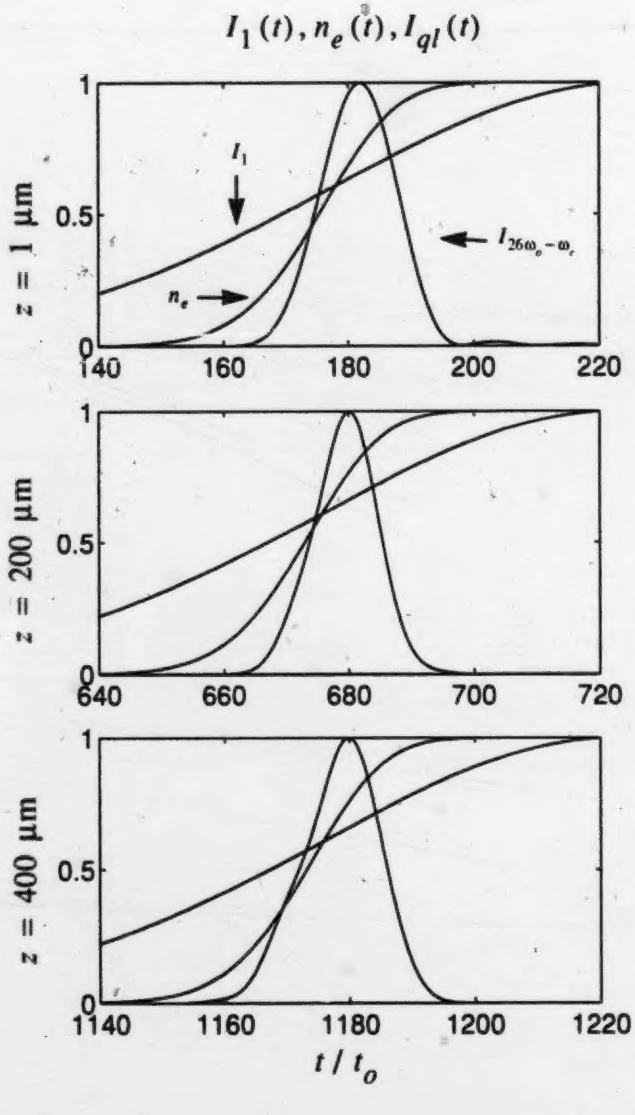

Figure 3.11: Temporal profiles of the $26\omega_o - \omega_c$ sub-band component recorded at different locations in the medium. Also shown are the normalized fundamental intensity and electron density.

result of different parts of the laser pulse propagating at different phase velocities due to the spatially and temporally varying electron density. As can be inferred from the analysis given in Section 2.2.3, the shifts are directly proportional to the slope of the ionization front times the propagation distance in the SVE approximation. It is obtained from the fact that the phase of a laser field with a vacuum wave vector and frequency, $\bar{k}, \bar{\omega}$, co-propagating with a relativistic ionization front in the SVE approximation is given by $\bar{k}[1-(1/2)n_e(z-ct)/n_c]z-\bar{\omega}t = \bar{k}z-\bar{\omega}t-(1/2)\bar{k}zn_e(z-ct)/n_c = \bar{k}z-\bar{\omega}[1+(z/2c)d(n_e(z-ct)/n_c)/dt]t$ where k_o is the vacuum wave vector of the laser field. This then shows a frequency shift of $\Delta\omega = \bar{\omega}(z/2c)d(n_e(z,t)/n_c)/dt$. From this analysis, the phases of the participating waves in the HDM scheme still follow that given by Eqns (3.1,3.2,3.5), but with n_e now replaced by $n_e(z-ct)$. Consequently, the phase matching condition given by Eqn (3.8) should still be valid.

However, when the frequency shift is large, it has been shown that the SVE approximation is no longer valid and the shifts become a nonlinear function of the density slope and propagation distance. Furthermore, the amplitude of the propagating field is also distorted and becomes a function of the upshifting laser frequency. From Ref. [51], the frequency of the laser field as seen in the retarded time frame ($z' = z$, $t' = t - z/c$) for a linear density ramp $n_e(t') = n_{eo}(t'/\tau)$ increases as:

$$\omega(z') = \bar{\omega}\left(1+\frac{z'}{c\tau}\frac{n_{eo}}{n_c}\right)^{1/2} \tag{3.27}$$

and the amplitude of the laser field is reduced by:

$$E(z') = E_o\frac{\bar{\omega}}{\omega(z')} \tag{3.28}$$

It should be noted that for small distances or frequency shifts, Eqn (3.28) reduces to that predicted by SVE analysis. Then, the phase of the laser field should be given by:

$$\theta(z',t') = \omega(z',t')t' - \bar{\omega}t' = \bar{\omega}\left[\left(1+\frac{z'}{c\tau}\frac{n_{eo}}{n_c}\right)^{1/2} - 1\right]t' \tag{3.29}$$

Again, for small frequency shifts, this formula reduces to that given by the SVE approximation: $\theta(z',t') \approx (1/2)(\bar{\omega}/c)z'(n_{eo}/n_c)(t'/\tau) = (1/2)\bar{k}z'(n_e(t')/n_c)$.

In the HDM process, the deviation from the SVE or ideal phase will result in a non-zero phase mismatch for the high frequency mixed field. In this case the phase match becomes:

$$\Delta\theta = -(\delta\theta_{ql} - q\delta\theta_1 + l\delta\theta_c) \approx l\delta\theta_c \tag{3.30}$$

where $\delta\theta \equiv \theta^{actual} - \theta^{ideal}$ is just the deviation from the SVE or ideal phase. In Eqn (3.30), the contributions from the corrections to the fundamental and mixed field phases should be small due to their much larger critical densities and can therefore be neglected.

Figure 3.12 shows the instantaneous frequency shift of the control field as calculated from the simulation near the ionization front. Also shown is the ideal frequency shift obtained from the SVE analysis. The control frequency shift is obtained from the simulation by differentiating the phase of the complex control field envelope with respect to time. Here, it is seen that at $z = 50$ μm, the actual frequency shift agrees quite well with the ideal shift up to the maximum shift at $t/t_1 \approx 300$ where the actual shift starts to deviate from the ideal case. As the control field propagates, the actual frequency shift deviates more and more from the ideal case. The frequency shift obtained from the simulation seems to agree very well with that predicted by Eqn (3.27). From Figure 3.11, it is seen that the slope of the ionization front near $n_e^{max}/2$ is about $(n_{eo}/n_c^c)/(25t_1)$ where $n_{eo}/n_c^c = 0.17$ for the 50 torr of gas and n_c^c is the critical density of the control field. Hence, the frequency shifts at the center of the ionization front as predicted from Eqn (3.27) will be $\Delta\omega_c/\omega_{co} = 1.1$ and 1.8 for $z = 200$ and 400 μm respectively. These values agree very well as those observed in Figure 3.12. One unexpected feature of the actual frequency shift is the apparent "spread" of the shift to the trailing edge of the ionization front. According to the Eqn (3.27), the frequency should be zero when the $dn_e/d_t = 0$ corresponding to $\tau = \infty$. However, from Figure 3.12, it is seen that at the trailing edge of the ionization front, even though the electron density is constant, there is a still a significant shift of the control field frequency. The cause of this effect is group velocity dispersion of the control field which is not taken into account in deriving Eqn (3.27). The phase of the control field is shown in Figure 3.13. Also shown is the phase as calculated from the SVE analysis and deviation from the SVE ideal phase. The phase deviation at the center of the ionization front is about π at $z = 200$ μm leading to a phase mismatch of $l\delta\theta_c = \pi$. Hence the mixed field, which peaks at the center of the ionization front, should saturate here. This indeed has been observed (see Figure 3.9).

A competing mechanism which can also cause saturation of the mixed field is the reduction of the control field amplitude. When this quantity is reduced below a certain threshold, the mixed atomic response becomes very small (see Figure 3.3). This will then prevent further growth of the mixed field. However, this problem can be easily solved by setting the initial control field amplitude to a value much higher than the threshold so that the amplitude remains above the threshold value in the region where saturation is caused by the nonlinear frequency shift. For example, in the present simulation, the initial amplitude of the control field has been set to $E_{co} = 0.037E_{1o}$ which is considerably above the threshold amplitude of $0.02E_{1o}$ (see Figure 3.3). Consequently, the reduced amplitude of the control field at the observed saturation of the mixed field is about $E_c(z = 200\ \mu\mathrm{m}) = 0.02\mathrm{E}_{1o}$ (see Figure 3.10) which can still support a significant magnitude of the mixed field nonlinear polarization.

From the above analysis, is is seen that the saturation of the mixed field is due to the nonlinear frequency shift of the long wavelength control laser and the nonlinear shift is more serious for longer wavelength fields. It may be possible to reduce the effects of the nonlinear frequency shift by reducing the wavelength of the control laser field. For example, a 3500 nm field can be used instead of the 10400 nm field to phase match the $26\omega_o - 3\omega_c$ mixed field. The energy conversion from this scheme is shown in Figure 3.14. Also shown for comparison is the conversion efficiency of the non-phase-matched 25th harmonic. Here, the initial amplitude of the control field is set to $E_{co} = 0.07E_{1o}$ which is needed to saturate the atomic response. It is seen that by using a shorter wavelength control field to phase-match a higher l-order mixed field, the phase matching length and therefore the maximum obtainable conversion

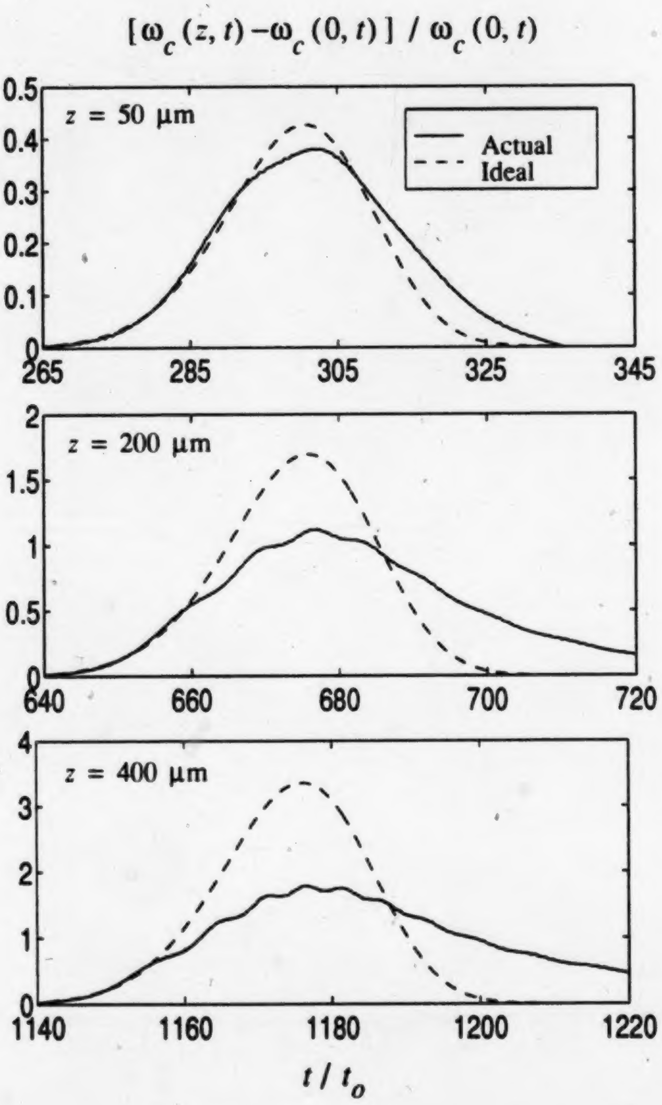

Figure 3.12: The control field frequency shift at different locations in the medium as obtained from the numerical simulation (solid lines) and from the SVE analysis (dashed lines)

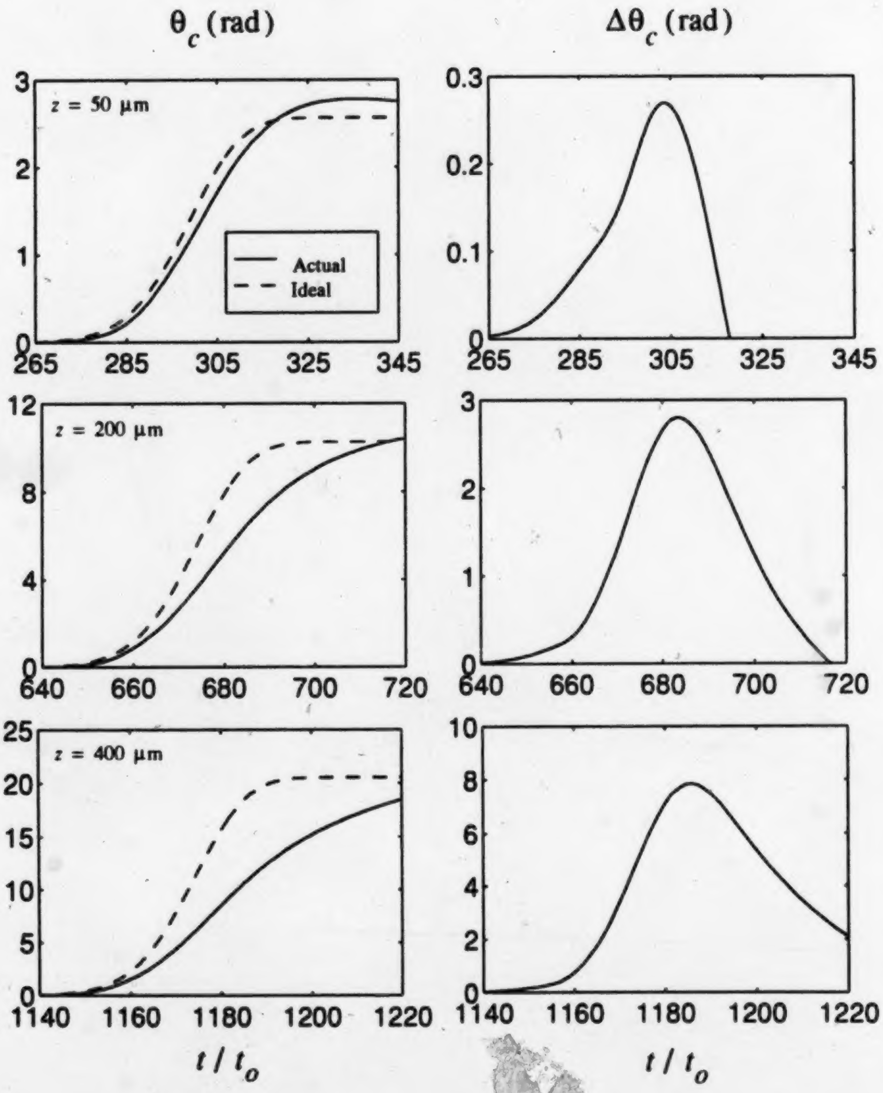

Figure 3.13: Shown on the left is the control phase as obtained from the numerical simulation (solid lines) and from the SVE analysis (dotted lines). Shown on the right is the deviation from the SVE phase.

efficiency can be significantly increased. In this case, a factor of 10 enhancement has been achieved.

It is then tempting to use this propagating model to study the possibility of further increasing the near-26 mixed field by using an even shorter wavelength control field to phase match even higher l-order mixed field components. However, for control field wavelengths less than 3500nm (which has already a half cycle of only 4 fundamental periods), the assumption that the control field amplitude is constant in one fundamental period becomes invalid. It is not clear if the propagating model can still be used in this regime. A different analysis may be needed to study HDM in which the incident frequencies are not very different from one another.

3.4 Summary and Conclusions

In this study, HDM of the type $\omega_{ql} = q\omega_o - l\omega_c$ $(\omega_o \gg \omega_c, q \gg l \geq 1))$ has been studied using a 1-D numerical propagation model incorporating the recombination polarization. It is found that very high order mixed field nonlinear polarization components can be produced by the mixing of a high intensity high frequency fundamental field and a low frequency low intensity control field. It is also found that although a prescription for phase matching a high frequency mixed field in a plasma with constant electron density exists, the conversion efficiency for HDM in an *ionizing* plasma cannot be arbitrarily improved. The saturation of the mixed field in such a plasma is due to the non-zero phase mismatch arising from the nonlinear upshift of the low frequency control wave propagating in a relativistic ionization front.

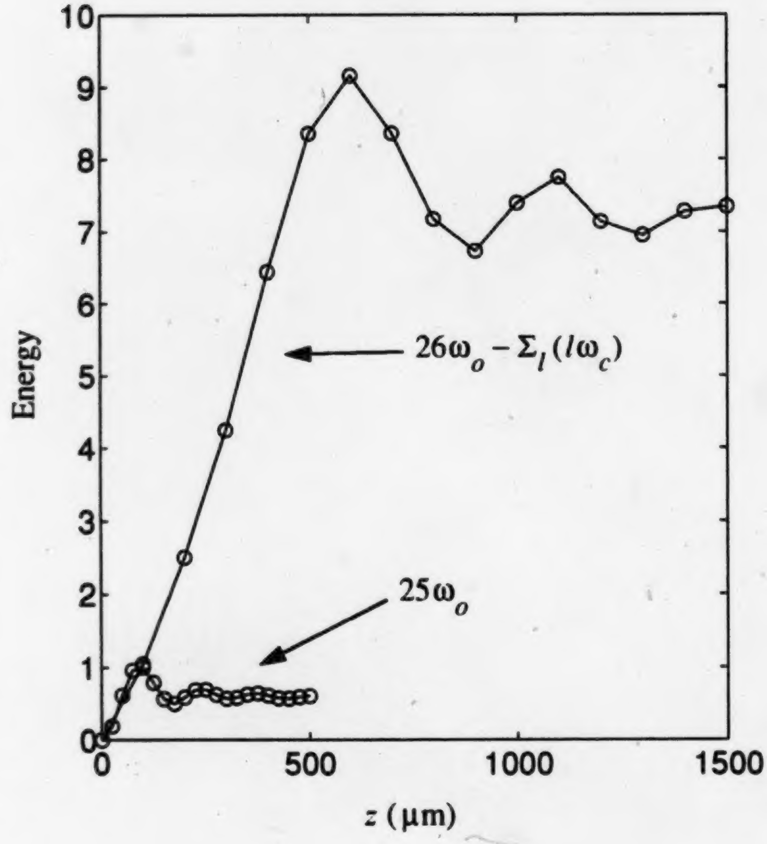

Figure 3.14: Energy conversion of the near-26 mixed field generated by the mixing of the same 400nm fundamental field and a 3500nm control field with an initial amplitude equal to $0.07E_{1o}$.

Chapter 4

Coherent Attosecond Soft-X-Ray pulses

Recent advances in laser technology have resulted in the production of visible laser pulses ($\lambda_o = 750$ nm) with durations as short as only a few femtoseconds and peak focussed intensities as high as 10^{16}W/cm^2 [52]. From the single atom viewpoint [53, 54], these ultra-short driving pulses may be exploited to generate radiation with much shorter wavelengths than is possible from longer driving pulses. As discussed in previous chapters, the highest frequency or cutoff radiation is related to the driving laser's intensity by $\hbar\omega_{max} = I_p + 3.17U_p$ where U_p is the highest ponderomotive potential which can be *felt* by the ionizing atom. As will be shown below, as the driving pulse width is shortened, the atom can experience higher and higher intensities before becoming completely ionized. Consequently, higher frequency radiation can be generated.

In this Chapter, an investigation of ultra high frequency conversion by an ultra-short duration driving pulse propagating in an atomic gas is described[1]. Section 4.1 describes response of a single atom to such an incident field. Section 4.2 discusses propagation effects in the one dimensional limit. Finally, Section 4.4 summarizes the findings and conclusions of this investigation.

---

[1] A version of this investigation has been submitted to Physical Review Letters entitled "Coherent xuv generation from gases ionized by several cycle optical pulses" by C. Kan, N. H. Burnett, C. E. Capjack and R. Rankin.

4.1 Single Atom Analysis

4.1.1 Ionization of the atom

Tunnel ionization by a short duration laser pulse can be quite different from that by a long duration pulse. Specifically, the highest intensity that can be experienced by an atom before it becomes fully ionized is quite different for short duration lasers than for long duration lasers. This is immediately apparent from the fact that the ionization probability, $P(t)$, depends not only on the instantaneous electric field strength but also on the field's history. That is,

$$P(t) = 1 - \exp\left(-\int^{t} R_t(E(t''))dt''\right) \tag{4.1}$$

where R_t is the tunnel ionization rate (see Section 2.1.1). As an example, Figure 4.1 shows the ground state population $(1 - P(t))$ calculated from the average tunnel ionization rate for a Gaussian laser pulse with different temporal (FWHM) durations but a fixed peak intensity equal to $2 \times 10^{15}\mathrm{W/cm}^2$. It is seen that for a 400 fs pulse, no atoms can survive the peak intensity without becoming completely ionized. However, as the pulse is shortened to 25 fs, about 20 % of the atoms can survive the peak intensity. For a 5 fs pulse, more than 70 % of the atoms can experience the peak intensity. Because more atoms can survive higher intensities for ultra-short laser pulses, higher frequency components can be produced with better conversion efficiencies.

4.1.2 The dipole response

The single atom dipole spectrum for an ultra-short duration driving field can be readily obtained by using the Lewenstein dipole model which makes no specific assumptions regarding the temporal duration or structure of the driving laser radiation (See Section 2.1.4 and Section 2.1.6). Shown in Figure 4.2 is the dipole acceleration

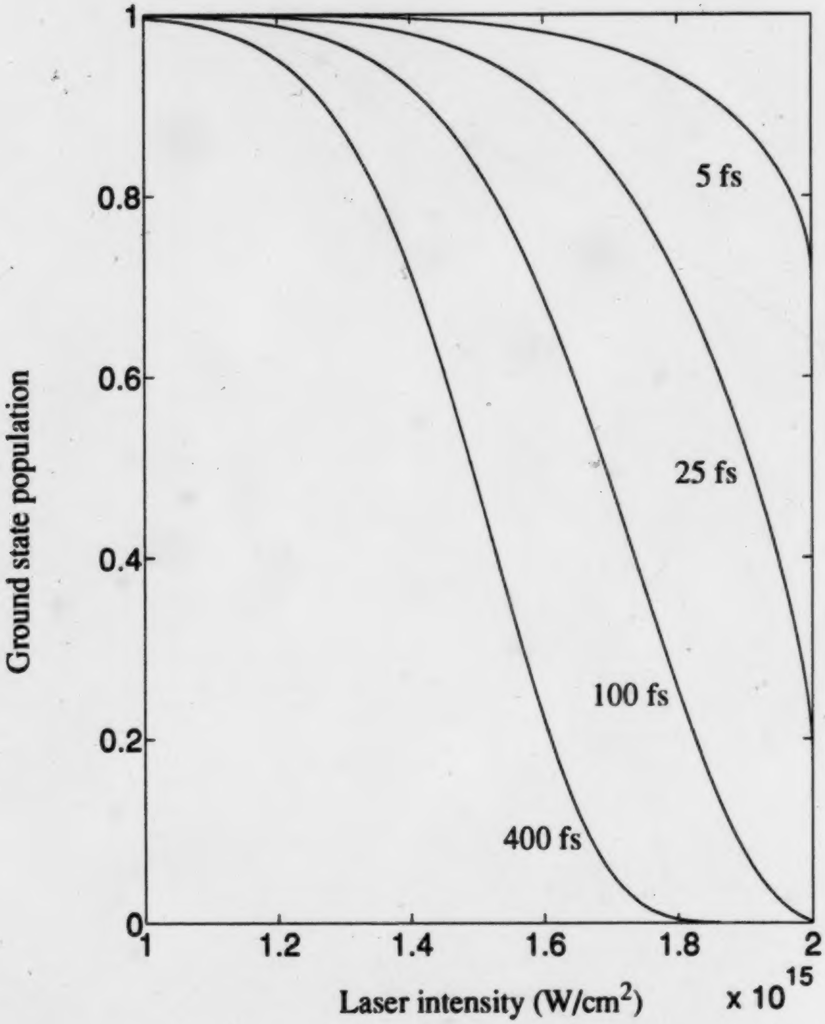

Figure 4.1: Ground state population for helium as calculated from the average ADK ionization rate for a Gaussian laser pulse with different FWHM durations. Plotted is the ground state population versus the *rising* portion of the laser pulse. The laser has a wavelength of 750 nm and a peak intensity of 2×10^{15}W/cm^2.

spectra obtained for a 750 nm, 5 fs, 2×10^{15}W/cm^2 driving laser pulse interacting with a helium atom. The spectra have been normalized with respect to the energy of the laser pulse ε_L. Also shown for comparison is the spectrum obtained for a 200 fs pulse. As expected, the very short duration driving pulse causes a very large frequency shift and broadening of the harmonic lines (See Chapter 2). As a result, distinct harmonic generation no longer exists for the 5 fs pulse. The dipole spectrum for the ultra-short pulse displays a rather complicated spectral structure.

Of the greatest interest in the spectrum is the region near the frequency cutoff which shows the highest frequency radiation achievable from this process. For the long duration driving pulse, the cutoff harmonic has a wavelength of about 750 nm / 175 = 4.3 nm. By using the cutoff law, $\hbar\omega_{max} = I_p + 3.17U_p$, this indicates that the atom has only experienced an intensity of about 1.6×10^{15}W/cm^2 before becoming completely ionized. On the other hand, for the short duration driving pulse, the highest frequency component has a wavelength of about 3.5 nm. By again using the cutoff law, this indicates that the atom has indeed survived the peak intensity of 2×10^{15}W/cm^2.

Also of interest is the temporal behavior of the ultra-high frequency radiation. Shown in Figure 4.3 is the temporal profile of the frequency components as seen through a spectral filter which only allows transmission of frequencies above $\omega/\omega_o = 210$. Also shown is the temporal profiles of the driving laser and ionization probability. It is seen that these frequency components constitute an attosecond pulse in the time domain.

The generation of the attosecond pulse in Figure 4.3 can be understood from the semi-classical picture inherent in the Lewenstein dipole model. In this picture, the generation of the high frequency field is due to the recombination of electrons which were ionized in the previous fundamental cycle and have been accelerated by the laser field. In the simplest case where the laser is only turned on for one fundamental cycle from $\omega_o t = -\pi$ to π, there exists only a very brief moment near $\omega_o t \approx 0.4\pi$ (see Section 2.1.2) where the highest frequency components can be generated. This

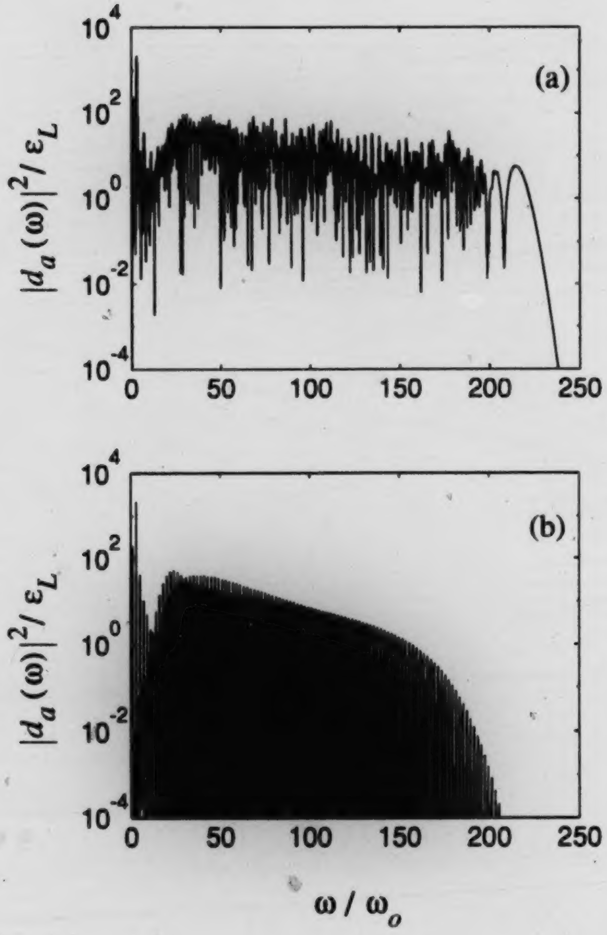

Figure 4.2: Dipole acceleration power spectra for a 750nm, 2×10^{15}W/cm^2 laser pulse interacting with helium. The driving pulse durations are (a) 5 fs and (b) 200 fs. The spectra have been normalized with respect to the energy of the driving pulse.

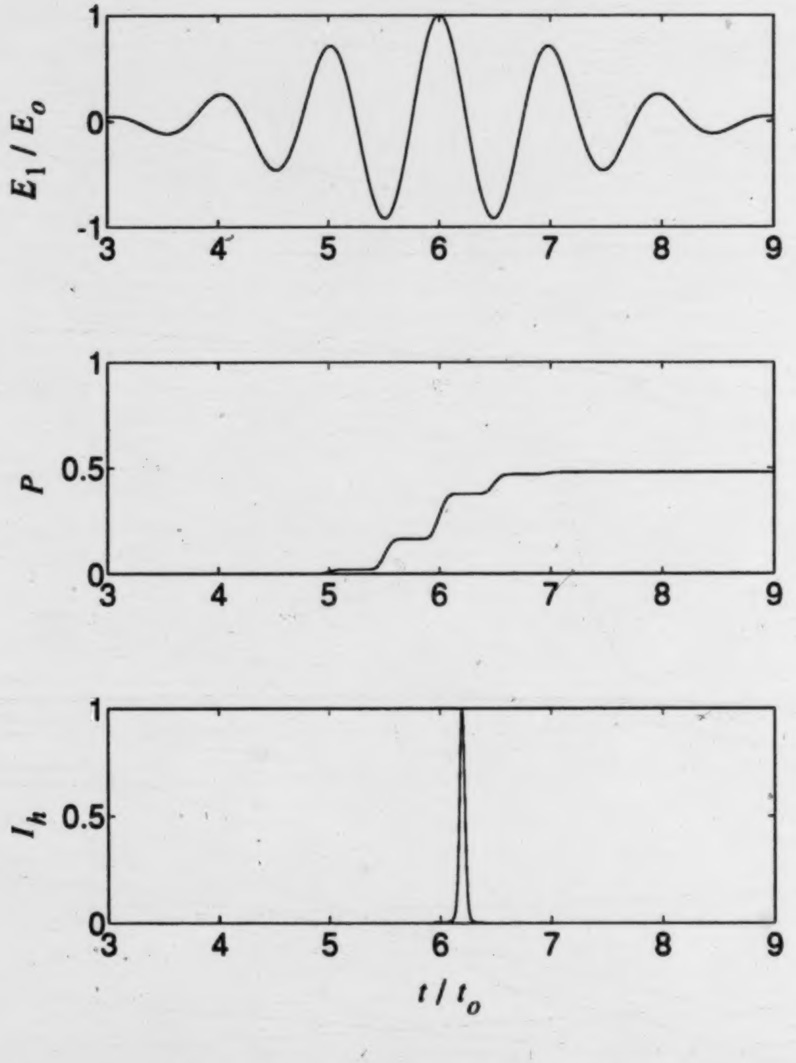

Figure 4.3: The temporal profiles of the incident electric field, $\underline{E}_1$, the ionization probability, P, and the intensity envelope of the dipole acceleration, I_h, as seen through a filter which only allows frequency components above $\omega/\omega_o = 210$ to pass through. Here, E_o is the maximum incident field strength corresponding to an intensity of $2 \times 10^{15}\mathrm{W/cm^2}$, $t_o = 2.5$ fs is the laser's fundamental cycle. The interacting medium is helium.

corresponds to the recombination time of the electrons which were ionized at $\omega t' = -0.6\pi$ and have acquired the maximum kinetic energy $3.17U_p$ from the driving field. In the case of the 5 fs pulse considered here, the maximum incident intensity only occurs in only one particular time interval (i.e. $t/t_o = 5.5$ to 6.5 in Figure 4.3) and has a clear contrast against the intensity peaks in the previous and following cycles. The highest frequency components are therefore generated within this particular cycle. According to the semi-classical picture, these frequency components should be generated near $t/t_o \approx 6.2$ by the electrons which are ionized near $t'/t_o \approx 5.7$. The temporal location of the calculated attosecond pulse agrees very well with that obtained from this semi-classical interpretation.

4.2 Propagation Analysis

4.2.1 The one dimension model

The one dimension model used here is very similar to that used in Chapter 2. The major difference follows from the dipole spectrum no longer consisting of distinct harmonic lines so that the slowly varying envelope approximation can no longer be used to decompose the harmonic equation into a set of envelope equations for the individual harmonic components. As a result, the total induced field generated by the nonlinear polarization must be solved by the full wave equation.

In this model, the total electric field inside the medium is decomposed into a high intensity fundamental field, $\underline{E}_1$ and the induced field, $\underline{E}_h$. Assuming $\underline{E}_1 \gg \underline{E}_h$, the fundamental field is again described by the envelope equation (see Section 2.2.1):

$$\frac{\partial^2 E_1}{\partial z^2} - \frac{1}{c^2}\frac{\partial^2 E_1}{\partial t^2} + \frac{2i\omega_o}{c}\left(\frac{\partial E_1}{\partial z} + \frac{1}{c}\frac{\partial E_1}{\partial t}\right) - \frac{\omega_{pe}^2(\underline{E}_1, t)}{c^2}E_1 = 0 \tag{4.2}$$

where the real field is defined as:

$$\underline{E}_1 = \mathrm{Re}[E_1 e^{i(k_o z - \omega t)}] \tag{4.3}$$

and the plasma frequency ω_{pe} in this case is obtained from tunnel ionization equation (Eqn. (2.7)) using the instantaneous d.c. ionization rate $R_t(\underline{E}_1)$ (Eqn. (2.4)). The propagation of the induced field, however, must now be studied using the full wave equation:

$$\frac{\partial^2 \underline{E}_h}{\partial z^2} - \frac{1}{c^2}\frac{\partial^2 \underline{E}_h}{\partial t^2} - \frac{\omega_{pe}^2(\underline{E}_1, t)}{c^2}\underline{E}_h = \frac{4\pi}{c^2} n_o d_a(\underline{E}_1, t) \tag{4.4}$$

which is required because the dipole acceleration d_a cannot be decomposed into a set of envelope components. Again, the quantum dipole model is used to obtain the dipole acceleration.

4.2.2 Solving the wave equations

In this study, the equation for the fundamental field is solved using the same finite difference technique as described in Appendix B. Although an attempt has been made to also solve the induced wave equation by a similar finite difference method, it is found that due to the large bandwidth of the induced wave, a very fine numerical grid is needed to obtain convergent results. To solve the induced wave equation for realistic modelling conditions in such a numerical grid requires computational power beyond that which is available in this project. Consequently, an approximate integral method has been used instead to solve the induced wave equation.

For very high frequency radiation, the effects of free electrons on its propagation is negligible. Therefore, for the high frequency portion of the induced radiation, the wave equation can be written as:

$$\frac{\partial^2 \underline{E}_h}{\partial z^2} - \frac{1}{c^2}\frac{\partial^2 \underline{E}_h}{\partial t^2} = \frac{4\pi}{c^2} n_o d_a^h(\underline{E}_1) \tag{4.5}$$

where d_a^h denotes the high frequency portion of the dipole acceleration. A Fourier transform of Eqn(4.5) gives:

$$\frac{\partial^2 \underline{E}_h(z,\omega)}{\partial z^2} + \frac{\omega^2}{c^2}\underline{E}_h(z,\omega) = \frac{4\pi}{c^2} n_o d_a^h(z,\omega) \tag{4.6}$$

from which a close form solution exists for $\underline{E}_h(z,\omega)$:

$$\underline{E}_h(z,\omega) = \frac{2\pi}{c} n_o \int^z dz' \frac{d_a(z',\omega)}{i\omega} e^{i\omega\frac{z-z'}{c}} \tag{4.7}$$

Here, the function

$$G(z,z') = \frac{i}{\omega/c} e^{i\omega\frac{z-z'}{c}} \tag{4.8}$$

is just the Green's function for the one dimensional Helmholtz operator, $d^2/dz^2 + (\omega/c)^2$, satisfying the boundary conditions for a wave advancing in the positive z direction assuming a $e^{-i\omega t}$ time dependence. Eqn. (4.7) can be easily integrated numerically once E_1 has been obtained from the numerical wave solver for the evaluation of the dipole moment d_a. Now, by noting the properties of Fourier transform operations, the physical meaning of Eqn. (4.7) becomes apparent. In the temporal domain, the integrand is simply the first time derivative of the dipole moment (or the dipole velocity) evaluated at the retarded time $t_R = t - (z - z')/c$. Hence, Eqn. (4.7) simply says that the temporal profile of the high frequency induced field is proportional to the sum of the dipole velocity fields recorded at earlier locations and evaluated at the retarded time.

4.3 Results and Discussion

The one dimensional model has been solved for a 5 fs incident laser pulse with a peak intensity of 2×10^{15}W/cm^2 and a wavelength of 750 nm interacting with 500 torr of helium. The spectral profiles of the induced field, $\underline{E}_h(z,\omega)$, near the cutoff frequency region are shown in Figure 4.4. Here, it is seen that the growth of the high frequency induced field saturates at about 9 μm. The saturation near the cutoff frequency region can be more clearly visualized by plotting the peak amplitude of the induced field envelope in the temporal domain. Shown in Figure 4.5 is the peak temporal amplitude of the induced field as seen through a spectral filter which only allows frequencies above $\omega/\omega_o = 210$ to pass through. The temporal profile of the filtered induced field at $z = 20\ \mu m$ is shown in Figure 4.6.

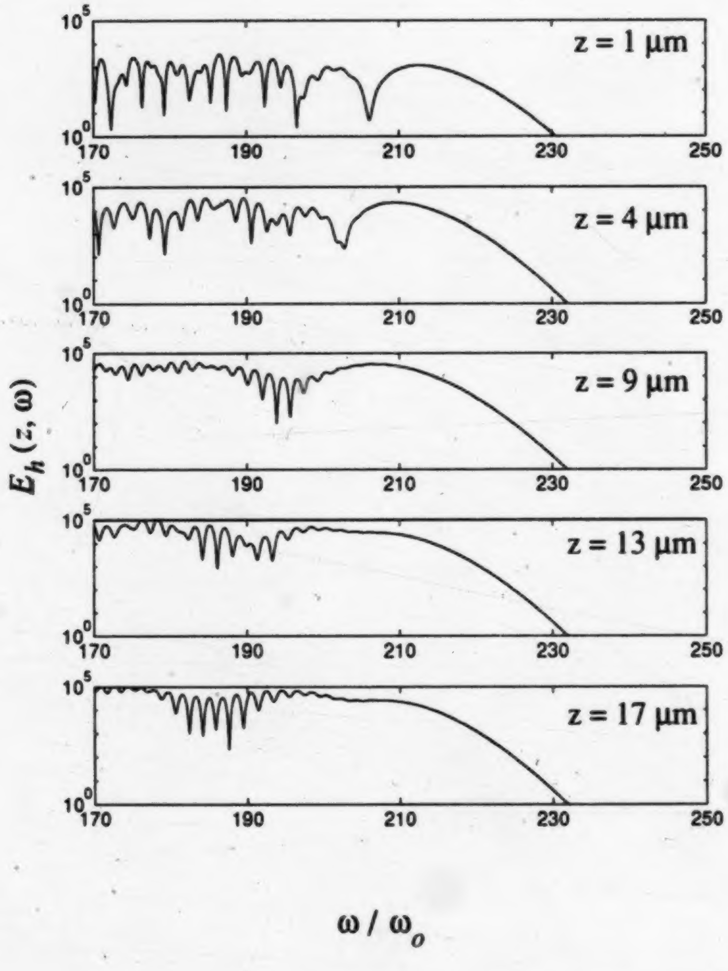

Figure 4.4: Spectral profiles of the induced harmonic field generated by a 750 nm, 5 fs, $2 \times 10^{15}\,\mathrm{W/cm^2}$ incident laser field interacting with 500 torr of helium. The spectral profiles are shown near the cutoff region as a function of propagation distance.

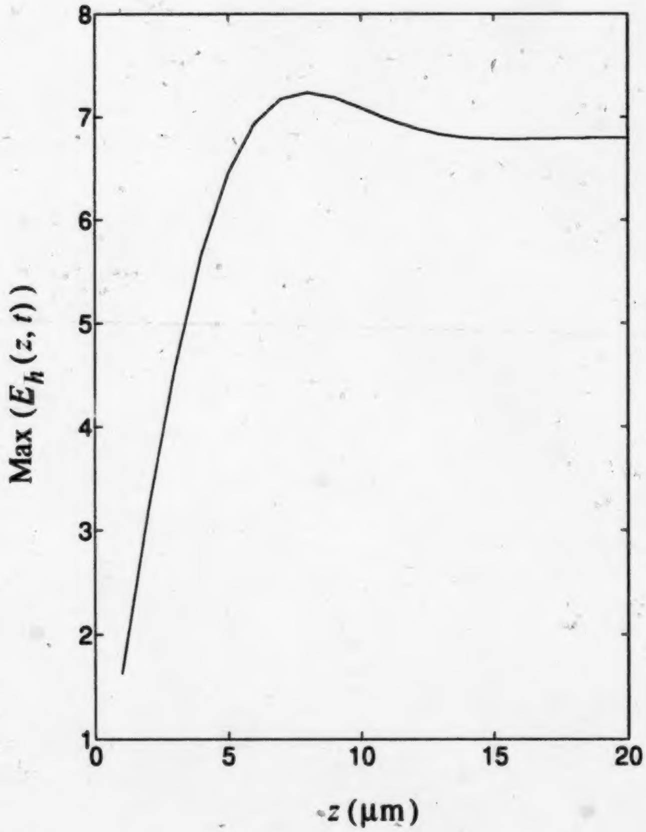

Figure 4.5: Peak amplitude of the induced field as function of propagation distance. The induced field has been spectrally filtered to contain only frequency components above $\omega/\omega_o = 210$

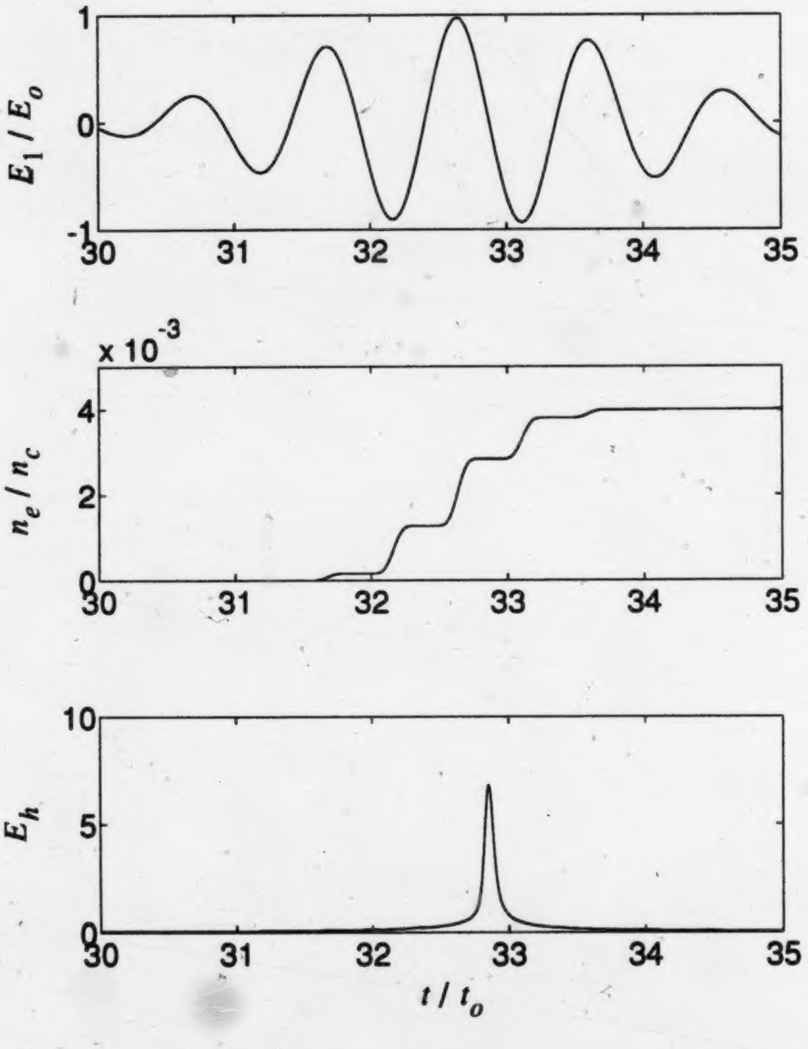

Figure 4.6: Temporal profiles recorded at $z = 20$ μm of the incident electric field, $\underline{E}_1$, the electron density divided by the critical density for the fundamental field, n_e/n_c, and the amplitude envelope of the induced field as seen through a filter which only allows frequency components above $\omega/\omega_o = 210$ to pass through. Here, E_o is the maximum incident field strength corresponding to an intensity of 2×10^{15}W/cm^2 and $t_o = 2.5$ fs is the laser's fundamental cycle. The interacting medium is helium.

4.3.1 Understanding of the conversion saturation

As discussed in Section 4.2.2, the Fourier transformed induced field at a distance z into the medium is proportional to the integral over earlier distances z' of the function:

$$d_v(z',\omega) = \frac{d_a(z',\omega)}{i\omega} e^{i\omega\frac{(z-z')}{c}} \tag{4.9}$$

which is just the Fourier transform of the dipole velocity field at z' evaluated at the retarded time $t_R = t - (z - z')/c$. Therefore, in order to understand the saturation of the induced field, the dependence of both the amplitude and phase of $d_v(z',\omega)$ on z' must be determined. Figure 4.7 and Figure 4.8 show, respectively, the magnitude of the Fourier transformed dipole velocity calculated by Eqn. (4.9) at different z' and the phase of several of its frequency components near the cutoff region as function of z'. From Figure 4.7, it is seen that the cutoff region of the dipole velocity spectrum seems to be moving towards lower frequencies for larger propagating distances. Therefore, the magnitude of the frequency components near the cutoff region ($210 < \omega/\omega_o < 230$) becomes vanishingly small after $z' \approx 13$ μm . Consequently, when these spectra are integrated along z', the high frequency portion (e.g. $210 < \omega/\omega_o < 230$) of the resulting integral will become constant after $z' \approx 13$ μm. This is indeed observed in Figure 4.5. From Figure 4.8, it is seen that the phase of the cutoff frequency components of the dipole velocity decreases for increasing z'. At $z' \approx 9$ μm, the change of phase is about π. Hence the induced field should saturate at this distance. This is also consistent with the result shown in Figure 4.5.

The decrease of the dipole spectrum's cutoff frequency can be understood as a result of the frequency upshift and amplitude reduction of the fundamental driving field which causes a reduction of the field's ponderomotive potential. A reduced ponderomotive potential results in a smaller kinetic energy of the recombination electrons which in turn lowers the frequency of the x-rays emitted. Figure 4.9 shows the amplitude and phase of the complex fundamental field envelope in the retarded time frame recorded at various locations. Also shown is the fundamental phase as

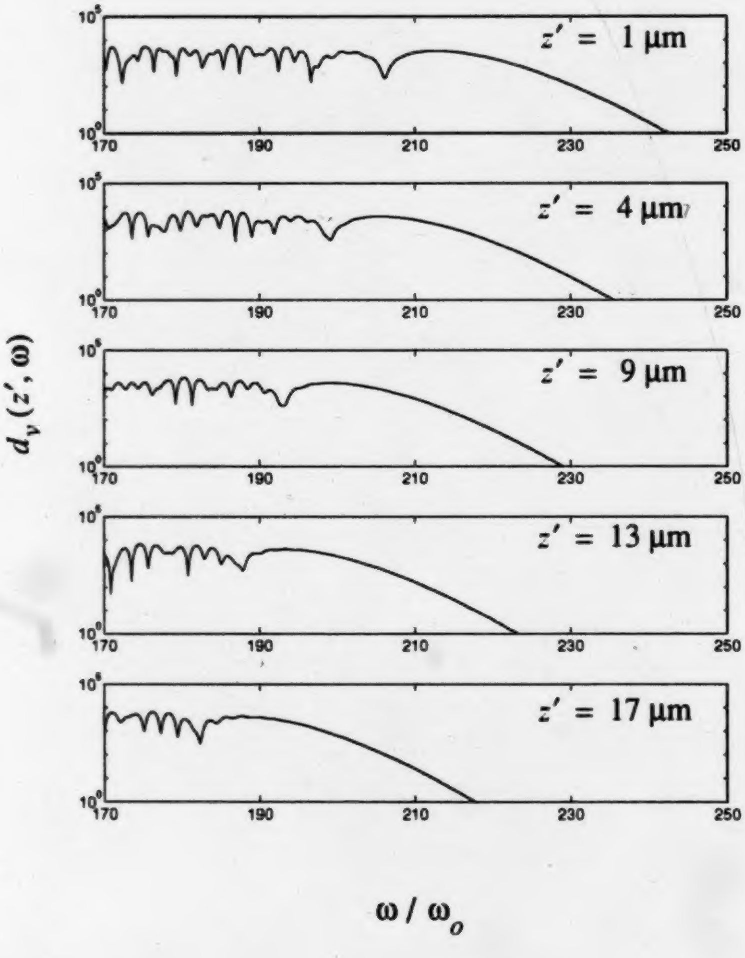

Figure 4.7: Magnitude of the Fourier transformed dipole velocity calculated at different locations in the medium.

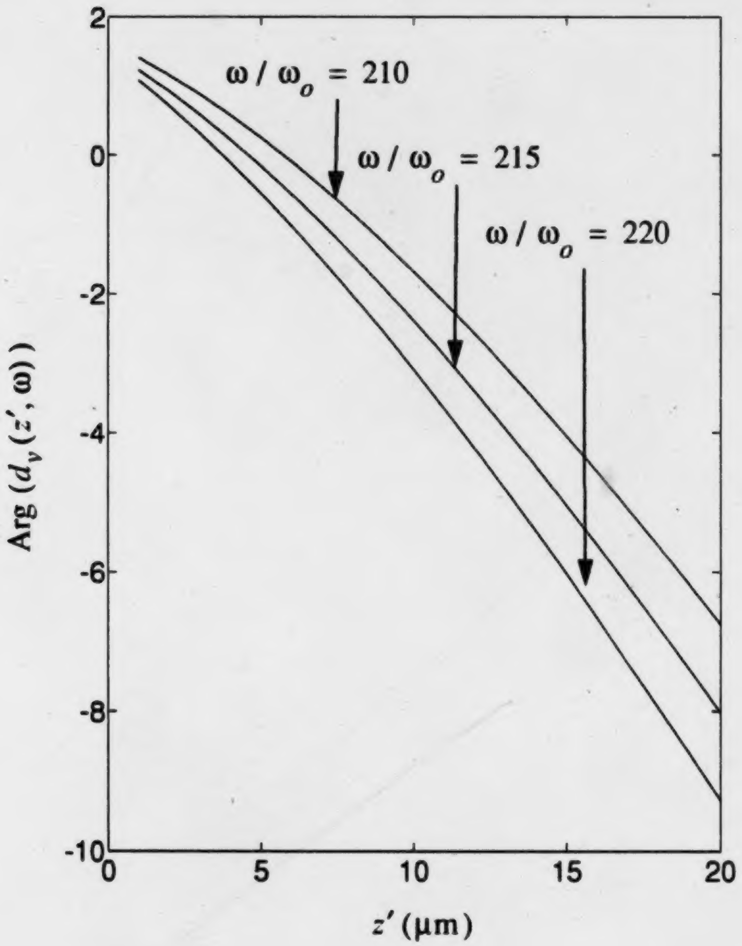

Figure 4.8: Phase of several frequency components near the cutoff region of the Fourier transformed dipole velocity as function of z'.

calculated from the SVE approximation (dashed lines) given by:

$$\theta_1^{SVE} = -\frac{z'}{\lambda_o}\frac{n_e}{n_c} \tag{4.10}$$

It is seen from the calculated results that the field amplitude is distorted as the field propagates. Most noticeable is the non-uniform reduction of the field amplitude. It appears that the reduction is greater at the times when the phase changes more rapidly with time. With regard to the fundamental phase, it is seen that the SVE approximation no longer applies here. Specifically, the calculated phase does not follow the shape of the electron density profile. As is described in Appendix D, a more accurate analysis shows that the phase as viewed in a retarded reference frame ($z' = z$, $t_R = t - z/c$) should be described by:

$$\theta_1 = \frac{z'}{\lambda_o}\mathrm{Re}[f(t_R)] \tag{4.11}$$

where the function f is a solution to the following differential equation:

$$\frac{df}{d(t_R/t_o)} - 2\pi i f - 2\pi^2 i\frac{n_e}{n_c} = 0 \tag{4.12}$$

In addition, the field envelope in the retarded frame should decrease according to:

$$E_1(z', t_R) = E_o \exp(\beta) \tag{4.13}$$

where

$$\beta = \frac{\Delta\omega}{\omega_o} = \frac{1}{2\pi}\frac{d\theta_1}{d(t_R/t_o)} = \frac{z'}{2\pi\lambda_o}\frac{d\mathrm{Re}[f]}{d(t_R/t_o)} \tag{4.14}$$

is just the instantaneous frequency upshift of the fundamental field. Hence, Eqn. (4.13) says that the reduction in field amplitude is largest when the instantaneous frequency upshift is the largest. It is interesting to note that, unlike the SVE analysis [2], the frequency upshift is actually smaller at times when ionization changes more rapidly. Figure 4.10 shows the fundamental phase and amplitude calculated from the semi-analytical analysis (Eqn. (4.11) and Eqn. (4.13)). Also shown are those from the numerical calculations. It is seen that the semi-analytical results agree with the fully numerical results very well. As the amplitude and frequency of the fundamental field are modified, the field's ponderomotive potential is also modified. This in turn modifies the maximum kinetic energy of the recombining electrons and ultimately changes the cutoff frequency of the x-ray emitted. Specifically, assuming the increase in intensity ΔI and the decrease in frequency $\Delta\omega$ is small, the ponderomotive potential of the fundamental field is modified by:

---

[2] In the SVE case, the frequency shift is proportional to dn_e/dt [55].

$$U_p = U_{po}\frac{(1-\Delta I/\Delta I_o)}{(1+\Delta\omega/\Delta\omega_o)^2} \approx U_{po}(1-\frac{\Delta I}{I_o}-2\frac{\Delta\omega}{\omega_o}) \qquad (4.15)$$

For the cutoff frequency components, the responsible electrons are ionized near the retarded time $t'/t_o \approx 32.2$ and recombine near $t''/t_o \approx 32.9$ (see Figure 4.9). By examining the amplitude and phase of E_1 from the simulation results, it is found that the average change in frequency in this temporal region is given approximately by $\Delta\omega \;/\; \omega_o = 0.0025z(\mu\text{m})$ whereas the change in the field envelope follows approximately $\Delta I \;/\; I_o = 0.003z(\mu\text{m})$. By assuming these two quantities are mainly responsible for the change in the ponderomotive potential in Eqn. (4.15), Figure 4.11 shows the cutoff frequency versus propagating distance as calculated from the cutoff law: $\hbar\omega_c = I_p + 3.2U_p$ where U_p is determined by Eqn. (4.15). It is seen that these results agree with the numerical results shown in Figure 4.7.

The phase shift of dipole velocity components in the retarded frame near the cutoff region can be also understood in terms of the phase, frequency and intensity modification of the propagating fundamental field. As discussed in Chapter 1 in the context of distinct harmonic generation, the phase of the high frequency field is related to the phase of the recombination electrons which is in turn determined by the following three quantities: the phase of ionization, the phase of recombination and the accumulated phase of the recombining electrons. These quantities in turn depend on the phase, frequency and amplitude of the fundamental field. Formally, the dependence of the dipole phase shift (in the retarded frame) can be written as:

$$\frac{d\theta_h(z',t_R)}{dz'} = \frac{\partial\theta_h}{\partial t'}\frac{dt'}{dz'} + \frac{\partial\theta_h}{\partial\omega_1}\frac{d\omega_1}{dz'} + \frac{\partial\theta_h}{\partial I_1}\frac{dI_1}{dz'} \qquad (4.16)$$

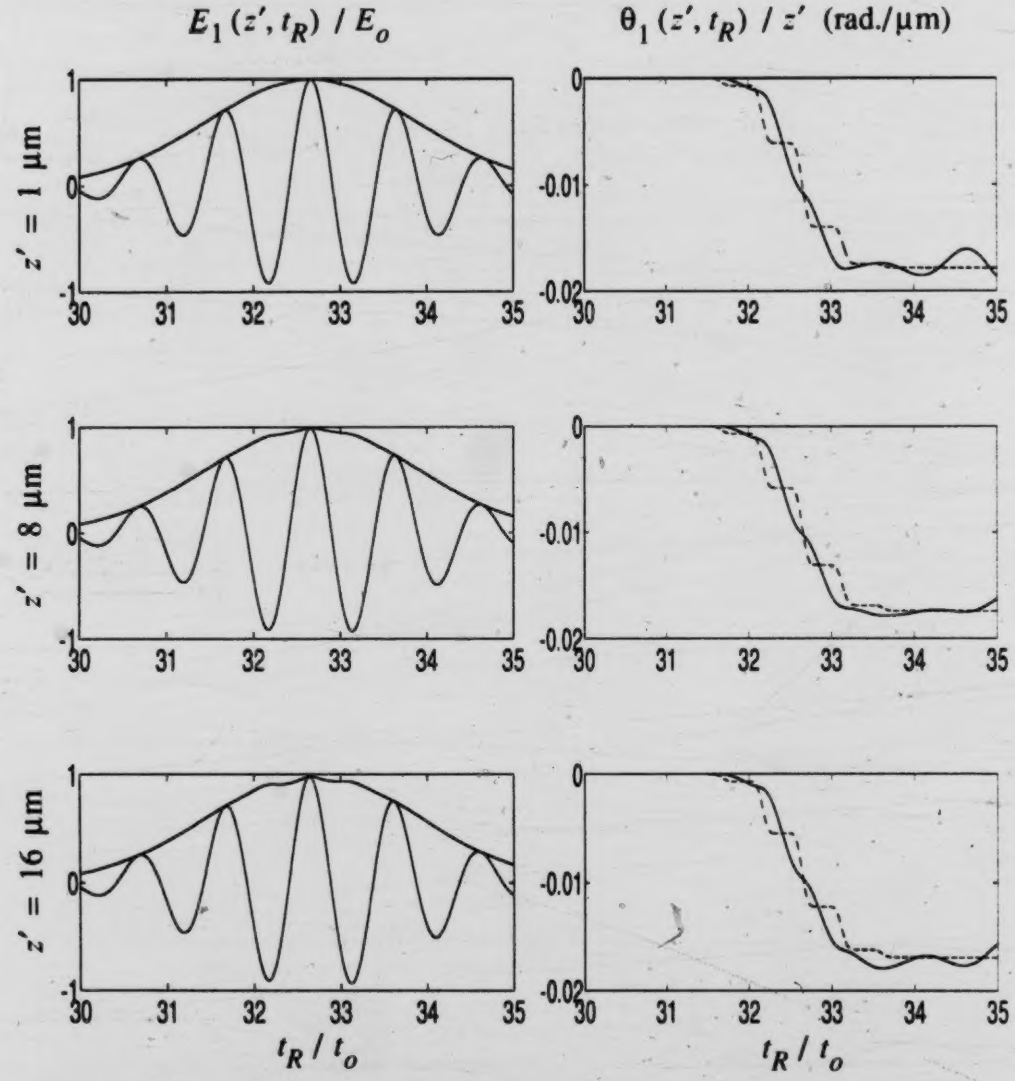

Figure 4.9: The amplitude and phase of the complex fundamental envelope in the retarded time frame recorded at various locations in the medium. E_o and t_o are respectively the initial peak field amplitude at $z = 0$ and the fundamental cycle. The dotted lines denote the phase calculated from the slowly varying envelope approximation.

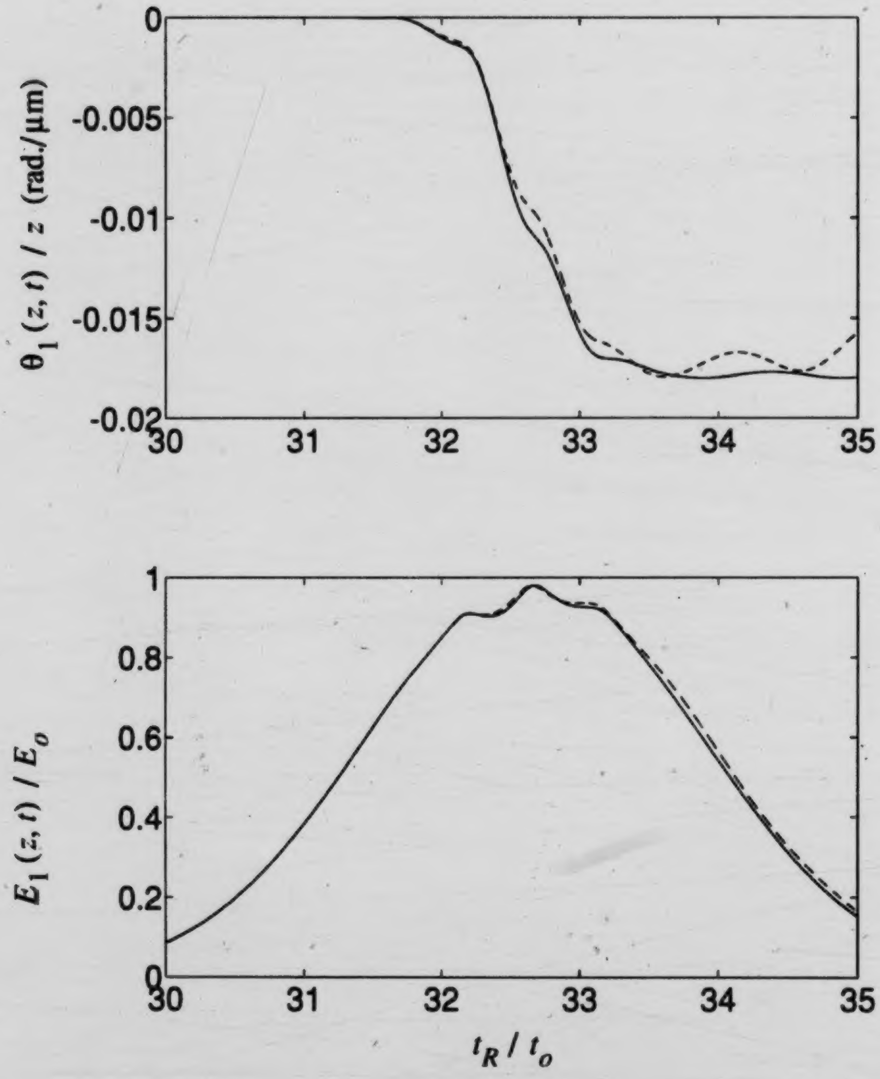

Figure 4.10: The phase and amplitude of the complex fundamental envelope in the retarded time frame recorded at $z = 16$ μm in the medium. E_o and t_o are respectively the initial peak field amplitude at $z = 0$ and the fundamental cycle. The solid lines denote results obtained from the semi-analytical calculations and the dotted lines denote results from numerical solution to the wave equation

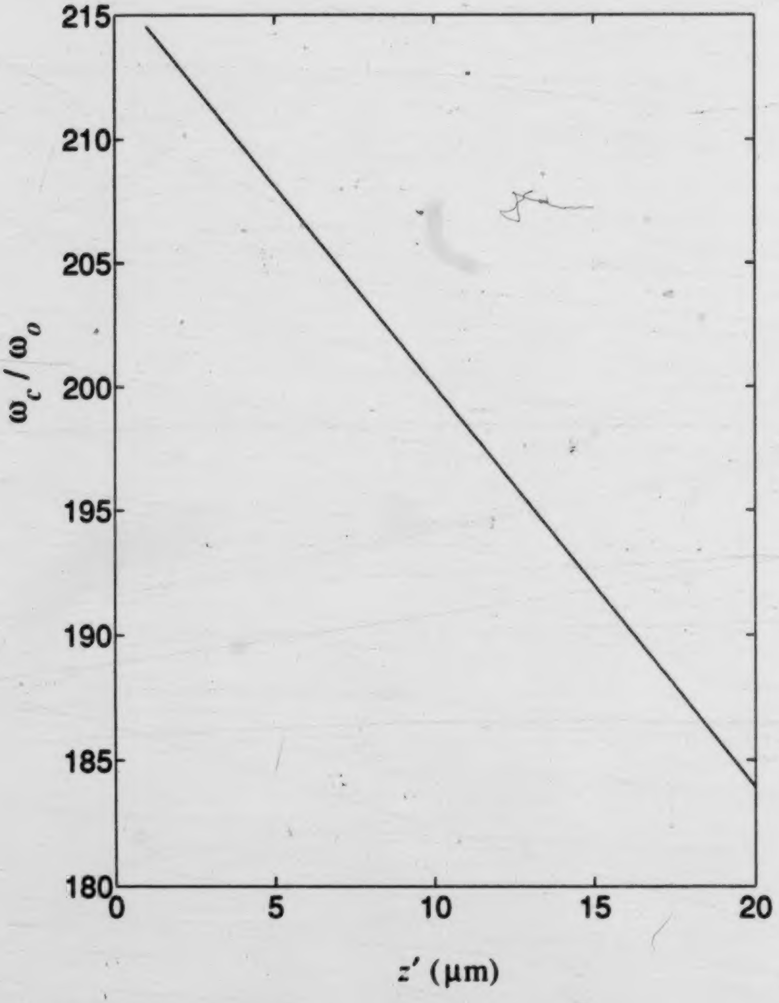

Figure 4.11: Change in cutoff frequency as predicted from the cutoff law. Here the change in the fundamental's ponderomotive potential is assumed to be due to the average frequency shift and the decrease in the peak intensity in the interval where the responsible electrons are ionized and recombine.

where $\omega_o t'$ is the phase at which ionization of the high energy recombining electrons occurs, ω_1 and I_1 are a measure of the fundamental field's frequency and intensity as experienced by the ionized electrons before recombination.

The contribution to the phase shift of the dipole velocity spectrum due to a change in the phase at which ionization occurs can be obtained as follows. When there is only a constant time shift of the fundamental field, i.e. $E_1(t+\delta t)$, it can be shown that the solution to the time dependent Schrödinger equation will only change by the same time shift, i.e. $\Psi(t+\delta t)$. Physically, this means that when the driving field is delayed by δt, the response of the atom is simply delayed by the same amount. Hence the dipole response will also only change by $d_v(t+\delta t)$. Accordingly, the phase of the dipole velocity frequency component ω_h in the Fourier domain will change by[3] $\delta\theta_h \doteq \omega_h \delta t$. Therefore, $\partial\theta_h \,/\, \partial t' = \omega_h$. Now, using the fact that the ionization time is related to the phase of the driving field θ_1 by $t' = \theta_1(t') \,/\, \omega_o$, the first term in Eqn (4.16) is given by:

$$\frac{\partial\theta_h}{\partial t'}\frac{\partial t'}{\partial z'} = \frac{\omega_h}{\omega_o}\frac{d\theta_1(t')}{dz'} \tag{4.17}$$

Then when Eqn (4.16) is integrated, the following expression for the dipole velocity phase shift results:

$$\theta_h = \theta_h^{t'} + \theta_h^{\omega_1, I_1} \tag{4.18}$$

where

$$\theta_h^{t'} = \frac{\omega_h}{\omega_o}\theta_1(t') \tag{4.19}$$

is just the dipole phase shift contribution due to a change in the time or phase at which the recombination electrons are ionized and

$$\theta_h^{\omega_1, I_1}(z') = \int^{z'} \left(\frac{\partial\theta_h}{\partial\omega_1}\frac{d\omega_1}{dz''} + \frac{\partial\theta_h}{\partial I_1}\frac{dI_o}{dz''} \right) dz'' \tag{4.20}$$

---

[3] This is a standard property of Fourier transform.

is the phase shift contribution due to the change in driving frequency and intensity in the time interval between ionization and recombination of the electrons responsible for generating the attosecond soft-x-rays.

In the case of a long driving (> 100 fs) pulse (see Chapter 2), the change in frequency and intensity (in the retarded frame) of the driving field, as experienced by the recombining electrons, should be small. Therefore $d\omega_1 \, / \, dz' \approx 0$ and $dI_1 \, / \, d\, z' \approx 0$. Hence, the main contribution to the dipole velocity phase shift should be mainly due to $\theta_h^{t'}$. In the SVE case, the driving phase is given by Eqn. (4.10). For a harmonic frequency $\omega_h \, /\omega_o = q$, the dipole velocity phase shift is then given by (using Eqn. (4.18) and Eqn. (4.19)) $\theta_h \approx \theta_h^{t'} = -(1/2)qk_o z'(n_e(t')/n_c)$ which is just the phase mismatch for a high frequency ($q \gg 1$) harmonic wave (see Eqn. (2.89)). However, when the driving field duration is as short as the 5 fs pulse studied here where the SVE approximation breaks down, the contribution from $\theta_h^{\omega_1, I_1}$ may become significant. An estimate of this contribution can be obtained as follows. First, the dipole velocity is calculated for the following artificial driving pulse:

$$I_1 = \begin{cases} \alpha I_o(t, \omega_o) & \text{if } t < t' \\ \alpha I_o(t, \omega_o + \delta\omega) & \text{if } t > t' \end{cases} \qquad (4.21)$$

where $I_o(t, \omega_o)$ is equal to the driving field at the entrance to the medium, t' is the release time at $z = 0$ of the electrons responsible for the generation of the ω_h frequency component, $\delta\omega$ is a constant frequency shift, and α is a constant used to adjust the peak intensity of the fundamental pulse. By varying α and $\delta\omega$ to model the effects of $I(z')$ and $\Delta\omega_1(z')$ as seen from the simulation, the phase of the ω_h frequency component can then be obtained as a function of $I(z')$ and $\Delta\omega_1(z')$.

Using the method discussed above, the contribution to the dipole phase shift for the $\omega_h/\omega_o = 215$ component, $\theta_h^{\omega_1, I_1}$, is shown in Figure 4.12. Plotted also are the contribution from $\theta_h^{t'}$ calculated from Eqn. (4.19) using $\theta_1(t')$ obtained from the simulation and the total contribution $\theta_h = \theta_h^{t'} + \theta_h^{\omega_1, I_1}$. Shown as circles are the actual phase shift of the ω_h dipole velocity frequency component as obtained from the simulation. It is seen that the results obtained from the semi-analytical analysis agree quite well with the simulation results and that the main contribution to the phase shift is due to $\theta_h^{t'}$.

Finally, it is interesting to compare the soft-x-ray conversion efficiency between a 200 fs pulse and the 5 fs pulse in this 1-D propagation limit. In Figure 4.13, the solid line denotes the peak intensity of the attosecond soft-x-ray pulse generated by the 5 fs driving pulse. The dashed line represents the peak intensity of the 201st harmonic generated by a 200 fs pulse in the same 500 torr helium with the same wavelength and peak intensity as the 5 fs pulse. It is seen that the attosecond x-ray pulse saturates at much longer distances into the medium with a much better conversion efficiency. Such a conversion improvement is due in large part to the much stronger dipole response produced by the 5 fs pulse (see Figure 4.2). The better conversion efficiency is also due to the longer phase matching length. As discussed above (and in Chapter 2), the phase mismatch for the high harmonic generated by the long driving pulse is $\Delta\theta_q = q\theta_1$ where θ_1 is the driving field's phase deviation from the vacuum phase and is given by Eqn. (4.10). Then the harmonic field should saturate at a distance z_s when $\Delta\theta_q(z_s) = \pi$. For a 200 fs driving pulse, the 201st harmonic is generated near the peak of the driving pulse where the intensity is high enough to accelerate the electrons to generate the high harmonic field. In this region, the atom is almost completely singly ionized and therefore $n_e \approx 500$ torr. Consequently, the anticipated saturation length should be about $z_s \approx 0.4$ μm which agrees very well the results shown in Figure 4.13. For the 5 fs case, the phase mismatch is also to a large extent determined by $q\theta_1$ (see Figure 4.12). However, according to the discussion just presented, θ_1 for the 5 fs pulse should be determined from Eqn. (4.11) and Eqn. (4.12) and should be evaluated at a time t' at which the recombining electrons responsible for the generation of the attosecond soft-x-ray pulse are ionized. At t', it is seen from the above results that θ_1 is much smaller than that calculated from the SVE formula assuming full ionization. As a result, the soft-x-ray field generated by the 5 fs pulse will have a much longer saturation length than for a 200 fs pulse.

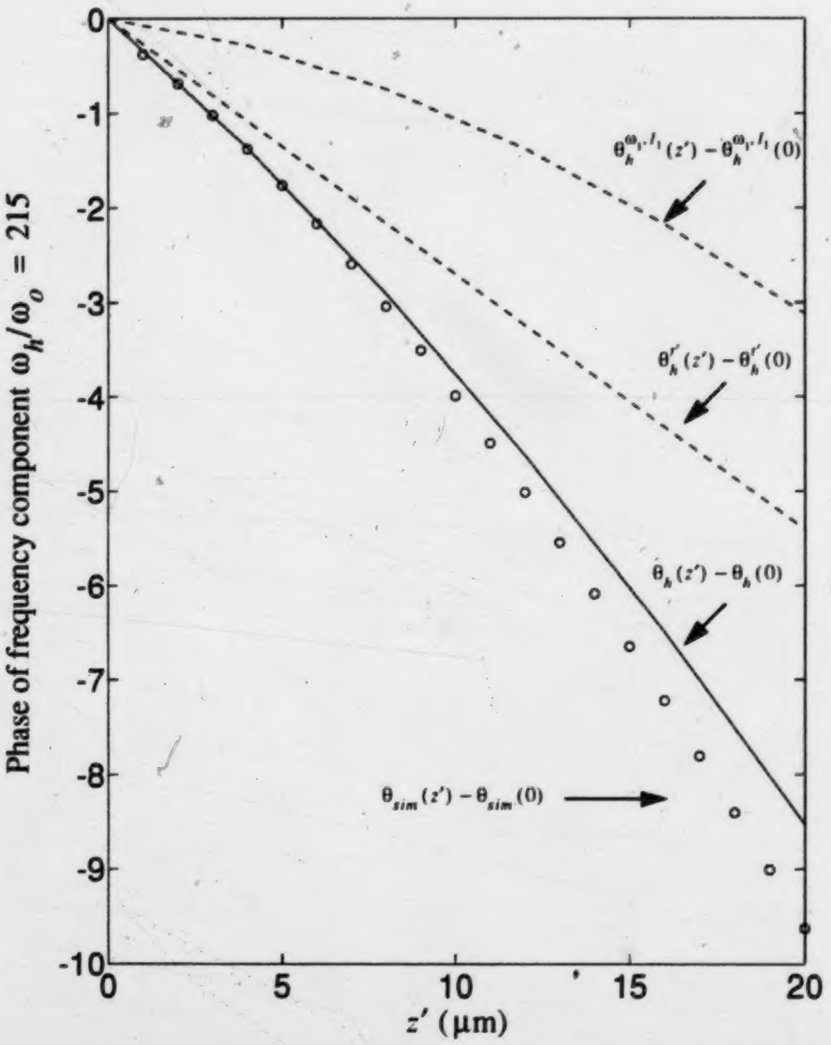

Figure 4.12: Phase of the ω_h / ω_o frequency component. The circles denote the phase obtained from the numerical simulation. The solid line represent the phase obtained from the semi-analytical analysis. The dashed lines denote the two contributions from the semi-analytical analysis.

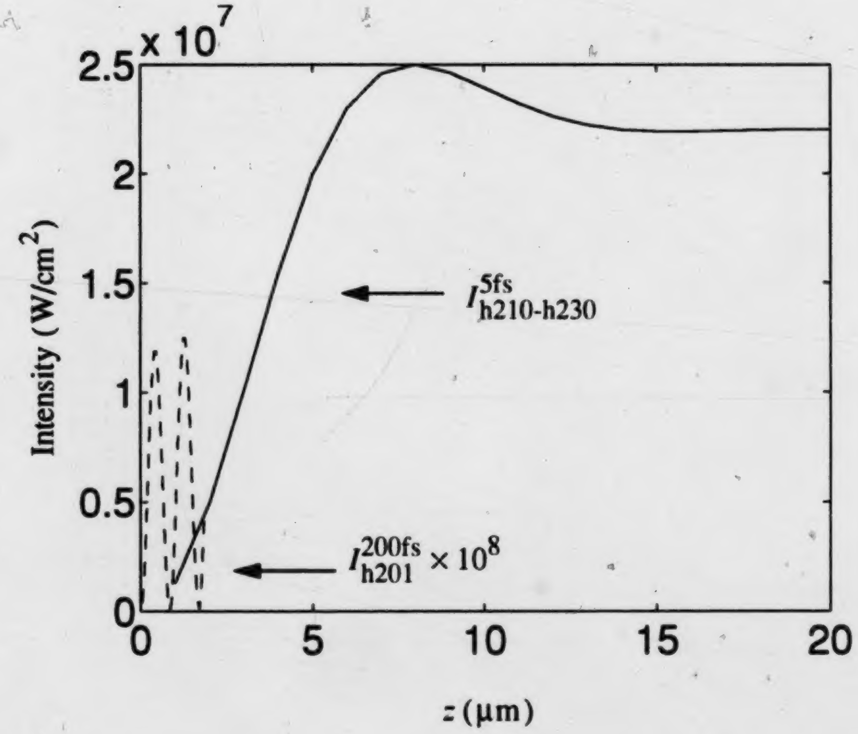

Figure 4.13: Peak intensities of the soft-x-ray attosecond pulse (solid line) and the 201st harmonic generated by a 200 fs incident laser pulse (dashed line).

4.4 Summary and Conclusions

In this study, ultra-high frequency conversion by an ultra-short duration driving pulse propagating in an atomic gas has been investigated. In a single atom study, it is found that much better conversion in the soft-x-ray region can be obtained by a 5 fs driving pulse as compared to that obtained by a 200 fs driving pulse. It is also found that the highest frequency components generated by the 5 fs pulse constitute an attosecond pulse in the temporal domain. Physically, such an attosecond pulse is due to the recombination of the electrons which have acquired the highest kinetic energy from the peak of the driving field during a single optical cycle. In the 1-D propagation analysis, it is shown that the soft-x-ray pulse, as generated by the 5 fs driving pulse, can achieve a much better peak intensity than that generated by a longer (200 fs) pulse. The improved efficiency is due to a stronger dipole response and a longer phase matching length.

Chapter 5

Two Dimensional Propagation Considerations

Propagation results in this thesis research have been obtained in the 1-D approximation. This is mainly because of the heavy computational requirement needed in 2-D studies and the restricted computational power available to this thesis project. However, it is felt that the 1-D approximation, besides providing a first step in understanding phase matching issues in the various studies conducted here, is also applicable in a number of realistic situations. In this chapter, important 2-D effects relevant to these thesis studies are discussed. Preliminary studies to examine the regime of applicability of the 1-D approximation are also given.

One important 2-D effect is the additional phase mismatch caused by focussing of the driving laser field. In a medium with constant dispersion and assuming the driving laser remains a Gaussian beam inside the medium and is not tightly focussed, the phase mismatch for the qth harmonic (where $q \gg 1$) produced by the Gaussian beam near the beam waist is given by[2]:

$$\Delta\theta_q = \Delta\theta_q^d + \Delta\theta_q^g \tag{5.1}$$

where $\Delta\theta_q^d$ is the phase mismatch due to dispersion in the medium and in the case of a plasma is equal to $q[(k_o z/2)(n_e/n_c)]$ as discussed earlier in the 1-D studies. The additional phase mismatch, $\Delta\theta_q^g$, is called the geometrical phase mismatch and is given by:

$$\Delta\theta_q^g = q\tan^{-1}[(z - z_f)/z_R] \tag{5.2}$$

where z_f and z_R are respectively the location of focus and the Rayleigh range of the driving laser. As discussed in Ref.[17], the geometrical mismatch is a direct result of the additional phase shift, $\theta_f = \tan^{-1}[(z - z_f)/z_R]$, that occurs in a focussed Gaussian beam relative to an unfocussed plane wave. This additional phase shift of the driving field then causes an additional phase shift of the harmonic nonlinear polarization equal to $q\theta_f$ which eventually leads to the additional phase mismatch given in Eqn. (5.1).

Focussing of the laser beam can also introduce another phase mismatch due to the change in axial laser intensity [56]. For a focussed laser beam in a constant dispersion medium, its axial intensity profile changes as it propagates according to:

$$I = \frac{I_o(z - ct)}{(1 + (z - z_f)^2/z_R^2)} \tag{5.3}$$

where $I_o(z - ct)$ is the axial intensity profile at focus. Since the atomic dipole moment and hence the nonlinear polarization have an intensity dependent phase (see Chapter 2), the varying axial driving intensity profile will then introduce a phase shift in the nonlinear polarization. This then also leads to a phase mismatch for the harmonic field.

Another important 2-D effect is the refraction of the driving laser beam propagating in the tunnel ionizing medium [41]. Due to the laser beam's radial intensity profile, which is highest on the propagation axis, the density of the tunnel ionized electrons builds up most quickly on axis. This leads to a radial refractive index profile which is *minimum* on axis. Such a refractive index profile then acts as a divergent lens which continually defocuses the driving laser beam as it propagates in the medium. Consequently, the axial intensity decreases as the laser propagates in the medium. Depending on the electron density profile, the effective interaction length of the laser beam can be limited to a value much shorter than the Rayleigh range. In terms of harmonic generation, defocussing of the driving laser beam can have two important effects. The first is the harmonic phase mismatch caused by the varying (decreasing) axial laser intensity as discussed above. The second is the fact that when the laser intensity decreases below the threshold for the generation of the high harmonics, the growth of these harmonics may saturate earlier than that predicted by free electron induced phase mismatch in the 1-D analysis.

Defocussing of a long duration laser pulse corresponding to the driving laser studied in Chapter 2 has been investigated by using a 2-D time dependent paraxial wave solver which has previously been developed at the University of Alberta to study beam refraction problems [41]. Here, the time dependent wave equation is numerically solved in the cylindrical slowly varying envelope (SVE) approximation:

$$\frac{1}{r}\frac{\partial}{\partial r}\left(r\frac{\partial E}{\partial r}\right)+2i\frac{\omega}{c}\left(\frac{\partial E}{\partial z}+\frac{1}{c}\frac{\partial E}{\partial t}\right)-\frac{\omega_{pe}^2}{c^2}E=0 \tag{5.4}$$

where the envelope E is related to the real field by $\underline{E} = \mathrm{Re}[E\exp(i(k_o z-\omega t))]$ and ω_{pe} is the plasma frequency calculated from the tunnel ionization equation.

Results have been obtained for a 150 fs laser pulse interacting with 500 torr of neon. The laser is assumed to have a wavelength of 750 nm and a focussed intensity in vacuum of 10^{15} W/cm^2. The Rayleigh range of the laser is 5 mm and the location of the focus is assumed to be at the entrance to the medium ($z = 0$). Shown in Figure 5.1(a) and (b) are the spatial profiles of the laser beam and the electron density profile recorded near $z = 200$ μm which corresponds to the location of saturation of the 55th harmonic studied in Chapter 1. It is seen that, due to refraction, the peak on-axis intensity is significantly lower than that predicted by Eqn. (5.3). This is more clearly seen in Figure 5.1(c) which shows the maximum axial intensity recorded at different locations in the medium. At $z = 200$ μm, the recorded intensity is about 7×10^{14} W/cm^2 which is about 30% less than the value of 10^{15} W/cm^2 predicted by Eqn. (5.3).

It has been found that one method to reduce the effect of defocussing on the axial intensity profile is to increase the Rayleigh range and consequently the beam waist of the incident laser beam for a fixed target thinkness. Figure 5.2 shows results for a laser beam with the same parameters as Figure 5.1 except that the Rayleigh range is equal

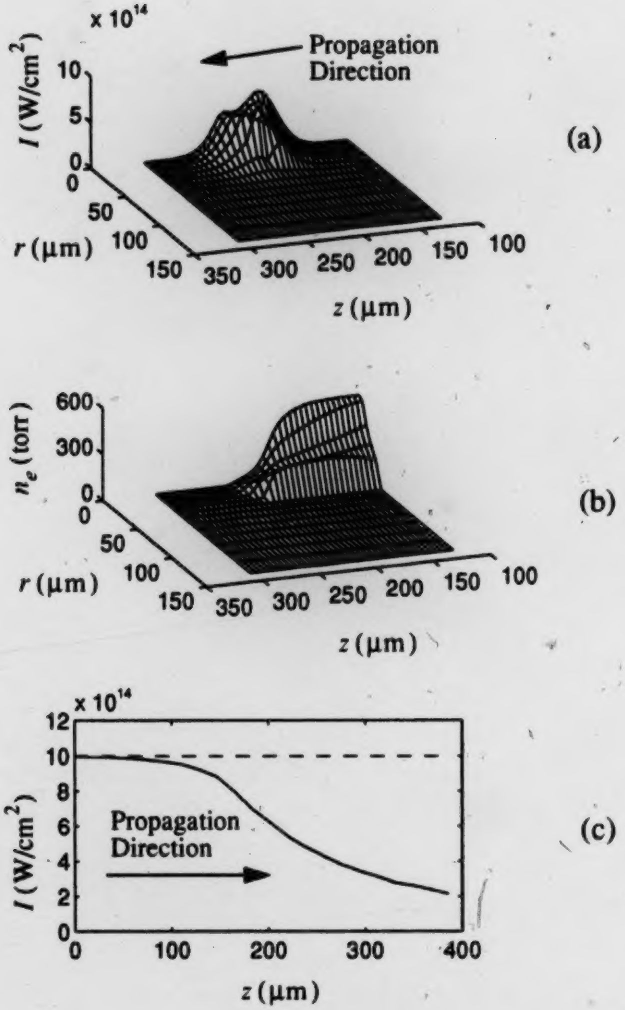

Figure 5.1: (a) and (b) Spatial profiles of the incident laser beam with a Rayleigh range of 5 mm and the electron density recorded near $z = 200\ \mu$m. (c) The peak axial intensity recorded at various locations in the medium (solid line) and that calculated from Eqn. (5.3) (dashed line).

to 20 mm. Here it is seen that the axial intensity is much closer to that determined from Eqn. (5.3). The reason for the improved axial intensity can be explained as follows. For an incident laser beam with a peak intensity much higher than that needed to saturate ionization, a flat-top density profile is created when the laser starts to enter into the medium. This means the electron density is approximately constant near the propagation axis where the intensity is large and decreases rapidly at a certain radial position where the intensity falls below the threshold for ionization. Therefore as the laser enters into the medium, only the wings of the laser beam are strongly refracted by the radial electron density "edge". The axial portion of the laser beam sees a rather constant electron density and does not refract significantly at this stage. However, as the laser propagates, the laser intensity at the "edge" of the flat-top density profile continues to decrease due to refraction and the density edge starts to get closer and closer to the propagation axis. Eventually, even the central portion of the laser beam is refracted. From this consideration, it is apparent that by making the laser beam waist larger at the entrance to the medium, it will take longer for the electron density edge to move near the propagation axis to refract the central portion of the laser beam.

One added advantage of using long Rayleigh range laser beams is the reduction of geometrical phase mismatch. This is immediately apparent from Eqn. (5.2). Figure 5.3 shows the axial phase profile recorded near $z = 200\ \mu$m. Also shown are the axial intensity and density profiles. The circles denotes the axial phase as calculated from the WKB formula: $-(1/2)k_o z(n_e/n_c)$. These results suggest that the axial phase of the laser closely follows that predicted from 1-D analysis and that geometrical phase mismatch plays no role here.

From the above analysis, it is seen that for long duration driving fundamental pulses studied in Chapter 2 and Chapter 3, the 1-D geometry can be achieved by propagating a loosely focussed beam in a thin target medium and considering only the central portion of the laser beam. These considerations may also be applicable in the propagation analysis of the 5 fs driving pulse studied in Chapter 4, although

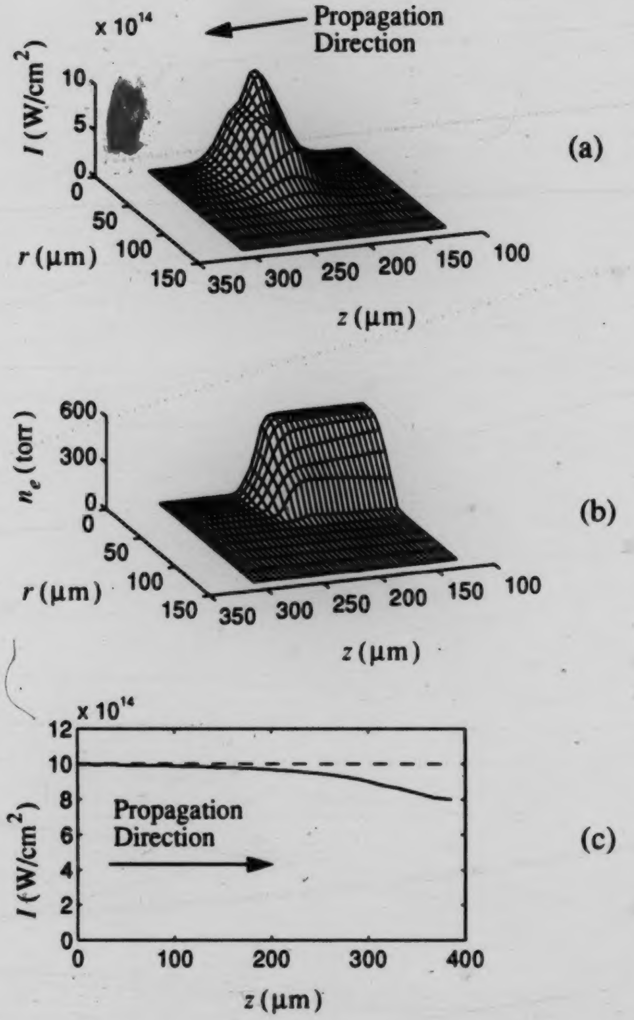

Figure 5.2: (a) and (b) Spatial profiles of the incident laser beam with a Rayleigh range of 20 mm and the electron density recorded near $z = 200$ μm. (c) The peak axial intensity recorded at various locations in the medium (solid line) and that calculated from Eqn. (5.3) (dashed line).

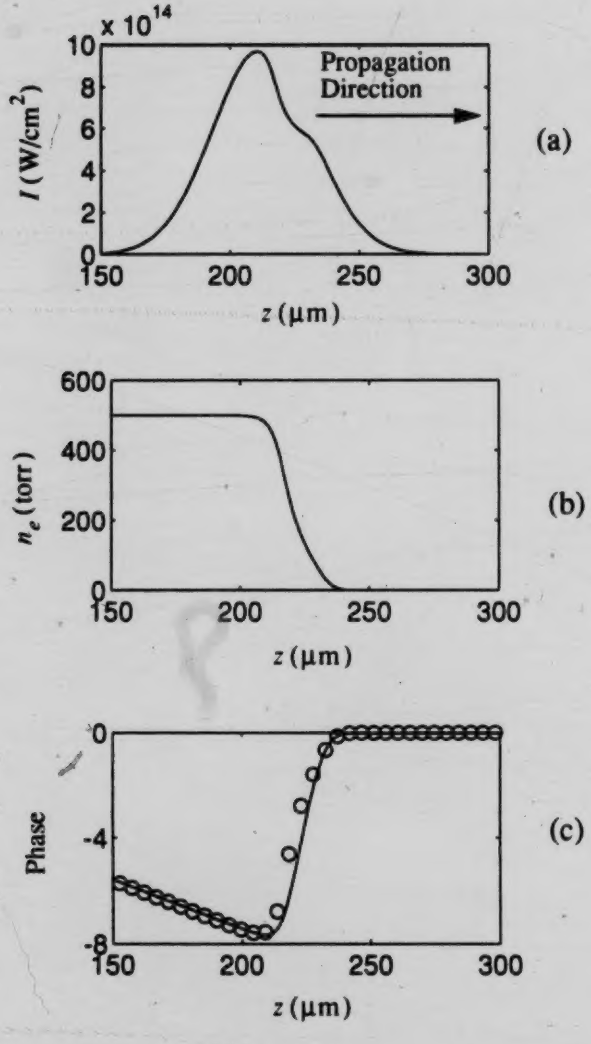

Figure 5.3: (a) and (b) On axis spatial profiles of the incident laser beam with a Rayleigh range of 20 mm and the electron density recorded near $z = 200$ μm. (c) On axis phase of the laser beam recorded at the same location. The solid line denotes the phase obtained from the numerical simulation while the circles denote the phase calculated from the WKB formula: $-(1/2)k_o z(n_e/n_c)$.

a model which goes beyond the SVE paraxial approximation may be needed to accurately describe the 2-D effects associated with these pulses. Finally, for the CW low frequency lasers studied in Chapter 3, refraction of these lasers may be much more severe than for the high frequency lasers discussed above due to their much longer wavelength. In this case, a plasma waveguide [40] may be needed to achieve an effective 1-D geometry for the problem.

Chapter 6

Conclusions

In this thesis, a number of studies have been carried out to investigate several important and practical issues in high harmonic generation. These include: (i) the spectral and temporal characteristics of the high harmonic emission; (ii) phase matching by high order difference frequency mixing; and (iii) generation and propagation of coherent attosecond soft-x-ray pulses. In this concluding chapter, a summary of the thesis investigation and results is given. The implications of the results are also discussed. The chapter ends will a discussion of possible future investigations.

Spectral and Temporal Study of High Harmonic Generation

This study examines the temporal and spectral characteristics of the high harmonic emission from both single atom and propagation analyses. In single atom analysis, two similar dipole models based on a three-step recombination model are used to obtain the single atom response. From these models, single-atom harmonic spectra as well as the temporal profile of individual harmonics have been obtained. It is identified that the harmonics are all spectrally blue shifted and can have very large linewidths. The origin of these blue shifts and large linewidths has been found and is due to the harmonic's phase dependence on the driving intensity which is varying in time. Specifically, it is found that each harmonic line can consist of several degenerate components whose phase is locked to the accumulated phase of the electron wavefunction at the recombination time at which the electron has the necessary recombination energy to produce the harmonic. The degeneracy comes from the fact that there can be several possible electron trajectories which have the same recombination energy but recombine at different times in each laser cycle.

A one dimensional propagation analysis has been carried out to study the effects of propagation on the spectral and temporal profiles of the harmonics. Here, the three-step recombination dipole model has been coupled to a 1-D wave equation with dispersion assumed to be caused by tunnel ionizing electrons. Results from the propagation analysis have shown that the temporal and spectral profiles of a propagated harmonic resemble those obtained from the single atom dipole analysis only at very small propagation distances near the entrance to the medium. As the harmonic propagates, the harmonic temporal widths shorten although the overall harmonic energy is still increasing. This continues until the harmonic becomes a transform-limited pulse with a duration as short as only a few femtoseconds. At this point, the harmonic energy also saturates. The propagation distance at which the harmonic saturates is larger for the lower order plateau harmonics compared to that for the high order cutoff harmonics. The shortening and saturation of the harmonic pulse has been explained by free electron induced phase mismatch introduced by the ionization front generated by the driving laser.

An important implication of these results is that the generated harmonic pulse *may* not be transform limited. Therefore, experimental measurements of the harmonic's spectral linewidth may not be able to determine the temporal duration of the harmonic field. These results also indicate that for femtosecond driving pulses, harmonic blue shifts and broad linewidths are *not* caused by the blue shift and line broadening of the driving wave due to time-dependent ionization [55], but are caused by a time or intensity dependent dipole phase. Another implication is concerned with the tunability of the harmonic radiation. Since the harmonics can have very large linewidths, they cannot be tuned by simply adjusting the frequency of the fundamental field. Special filtering techniques which can choose a practical frequency component within a harmonic line may be needed to achieve tunability. From these results, it is also seen that one method of making narrow harmonic lines is to use a driving pulse with a flat top temporal profile, i.e., a laser pulse which can rise rapidly to an intensity needed to produced the desired harmonics and remain constant at such an intensity for many laser periods. This will greatly reduce the blueshift and line broadening due to the intensity dependent harmonic phase. Results from this study also indicate that in the one dimensional propagation geometry, phase matched XUV harmonic pulses with temporal durations of a few femtoseconds may be produced. Such a geometry may be achieved by propagating a loosely focussed laser beam with a flat top spatial profile near the propagation axis in a thin high density target.

High order Difference Frequency Mixing

This study explores a possibility to reduce or eliminate the phase mismatch caused by free electrons. Here, a previously proposed phase matching scheme is investigated. In this scheme, a low frequency (ω_c) control field is allowed to co-propagate with a high frequency (ω_o) driving field in the interacting medium. It was shown under a number of general assumptions that the generated "mixed" field ($\omega_{ql} = q\omega_o - l\omega_c$) can be phase matched by adjusting the frequencies of the incident fields such that $\omega_c = (l/q)\omega_o$. A study has been done to investigate the high order difference mixing (HDM) scheme in a regime where HHG can also take place. Here, the dipole model previously used to study HHG is used to obtain the HDM nonlinear polarization. It is found that if the intensity of the high frequency field is sufficiently high to produce a broad HHG dipole spectrum, the addition of a very moderate intensity low frequency control field can produce very high order mixed field components. Specifically, apart from a small frequency blue shift due to an intensity dependent phase, the mixed field dipole components are located very close to the expected frequencies $q\omega_o - l\omega_c$ where, unlike HHG in which only $q =$ odd is possible, $q =$ even is also possible in HDM. However, due to the atomic symmetry, only $l =$ even lines exist for $q =$ odd and only $l =$ odd lines exist for $q =$ even. The maximum achievable amplitudes of these mixed field components are about an order of magnitude lower than those of the neighboring odd harmonics when no control field is present.

A propagation model which incorporates the HDM dipole response has been used to investigate the mixed field conversion efficiency in the HDM phase matching scheme. This model is very similar to that used in Chapter 2 to study HHG. Results have been obtained to examine the phase matching of two "near even" mixed waves with frequencies $q\omega_o - 1\omega_{c1}$ and $q\omega_o - 3\omega_{c2}$ where $\omega_{c1} = (1/q)\omega_o$ and $\omega_{c2} = (3/q)\omega_o$. It is found that even though the frequencies of the driving and control waves are chosen to satisfy the proposed phase matching condition, the mixed field still saturates. The saturation distance is about an order of magnitude shorter for the $q\omega_o - 1\omega_{c1}$ field compared to that for the $q\omega_o - 3\omega_{c2}$ field. For the $q\omega_o - 3\omega_{c2}$ wave, about an order of magnitude increase in conversion efficiency has been obtained compared to the conversion efficiency of the neighboring odd harmonic when no control field is present. For the $q\omega_o - 1\omega_{c1}$ field, no improvement has been obtained. The cause of the saturation of the mixed field has been found. It is due to the fact that HDM is taking place in a relativistic ionization front in which nonlinear frequency upshifts of low frequency fields due to the electron density gradient can introduce a large phase mismatch in the high frequency mixed field.

These results show that HDM cannot be used to arbitrarily increase the conversion efficiency of the high frequency mixed field even in a one dimensional geometry such as that achieved in a plasma waveguide [40]. However, it may be possible to greatly increase the conversion efficiency of a high frequency mixed field generated by ions. The use of ions is attractive because it can increase the shortest wavelength achievable due to the ions' higher ionization potential and larger saturation intensity as compared to neutral atoms. This can be seen from the cutoff law. The anticipated conversion improvement is due to the fact that for $n_e/n_c \ll 1$ the phase mismatch of the mixed field is caused by the electron density *gradient* and is not due to the static electron density. Therefore, HDM can be used to eliminate the potentially large phase mismatch of the mixed field due to the background electron density in the ionized plasma.

Attosecond Coherent X-rays

In this study, the possibility of increasing the conversion efficiency of the cutoff harmonics is explored. This investigation has been done in light of the availability of high intensity optical laser pulses with a duration of only a few laser cycles. Preliminary analysis from tunnel ionization considerations has shown that as the width of the driving laser pulse shortens, many more neutral atoms can experience the peak of the laser pulse. Therefore, many more electrons can still be ionized and accelerated near the peak of the driving field. Consequently, much stronger high frequency emission can be expected from the recombination of these energetic electrons.

Calculations from the quantum dipole model have verified this simple picture. From these calculations, it is shown that the amplitudes of the cutoff dipole frequency components as obtained from an ultra-short driving pulse are many orders of magnitude larger than those obtained using a much longer driving pulse. It is also found that due to the very short duration of the driving pulse, distinct harmonic generation no longer exists. The dipole spectrum obtained from the ultra-short driving pulse actually resembles a continuum spectrum. It is also found that the high frequency components in the spectrum constitute an attosecond soft-x-ray pulse in the temporal domain. Physically, the attosecond pulse is due to a *single* recombination of the electrons which are ionized just before the peak of the laser pulse and which recombine just after the peak of the laser pulse. A propagation analysis has been done to examine phase matching issues in the 1-D limit. Results from this analysis show that the attosecond soft-x-ray pulse has a phase matching length about an order of magnitude greater than that of a soft-x-ray harmonic generated from longer driving pulses. An explanation of the improved phase matching length has been found. It is due to the ultrashort driving pulse's much smaller phase deviation from the vacuum phase at the time when the electrons are ionized. As a result of the enhanced dipole response and phase matching length, the attosecond soft-x-ray pulse is found to have a peak intensity many orders of magnitude larger than that of the soft-x-ray harmonic produced by longer driving pulses.

Results in this study indicate that in the one dimensional limit, efficient generation of attosecond coherent x-ray pulses is possible. This is achieved by propagating an intense optical laser pulse with a few femtoseconds duration in a high density helium gas.

Future Investigations

An interesting extension to the present work is the investigation of the effects of the relative carrier phase of the several-femtosecond driving pulse studied in Chapter 4. Preliminary calculations have shown that the value of the carrier phase can affect the intensity of the x-ray spectrum near the cutoff region by an order of magnitude.

Phase matching of the XUV radiation generated by several-femtosecond optical pulses also deserves further investigation. Preliminary calculations have shown that these ultra-short optical pulses can also efficiently generate the frequency components in the XUV region.

References

[1] M. Gavrila, editor, *Atoms in Intense Laser Fields*, (Academic, Boston, 1992).

[2] Anne L'Huillier, Louise-Andre Lompre, Gerard Mainfray, "High-order harmonic generation in rare gases", in *Atoms in Intense Laser Fields*, edited by M. Gavrila (Academic, Boston, 1992).

[3] R. C. Elton, *X-ray lasers* (Academic Press, Boston, 1990).

[4] J. J. Macklin, J. D. Kmetec, and C. L. Gordon, III, "High-order harmonic generation using intense femtosecond pulses", Phys. Rev. Lett. **70**, 766 (1993).

[5] Anne L'Huillier and Ph. Balcou, "High-order harmonic generation in rare gases with a 1-ps 1053-nm laser", Phys. Rev. Lett. **70**, 774 (1993).

[6] Nobuhiko Sarukura, Kiyoshi Hata, Takashi Adachi, Ryoichi Nodomi, Masayoshi Watanabe, and Shuntaro Watanabe, "Coherent soft x-ray genration by the harmonics of an ultrahigh-power KrF laser", Phys. Rev. A **43**, 1669 (1991).

[7] Yutaka Nagata, Katsumi Midorikawa, Minoru Obara, and Koichi Toyoda, "High-order harmonic generation by subpicosecond KrF excimer laser pulses", Opt. Lett. **21**, 15 (1996).

[8] S. G. Preston, A. Sanpera, M. Zepf, W. J. Blyth, C. G. Smith, J. S. Wark, M. H. Key, K. Burnett, M. Nakai, D. Nelly, A. A. Offenberger, "High-order harmonics of 248.6nm KrF laser from helium and neon ions", Phys. Rev. A **53**, R31 (1996).

[9] T. Ditmire, J. K. Crane, H. Nguyen, L. B. DaSilva and M. D. Perry, "Energy-yield and conversion-efficiency measurements of high-order harmonic radiation", Phys. Rev. A **51**, R902 (1995)

[10] R. Haight and D. R. Peale, "Antibonding state on the Ge(111):As surface: spectroscopy and dyamics", Phys. Rev. Lett. **70**, 3979 (1993).

[11] R. Haight and D. R. Peale, "Tunable photoemission with harmonics of subpicosecond lasers", Rev. Sci. Instrum. **65**, 1853 (1994).

[12] R. Haight and P. F. Seidler, "High resolution atomic core level spectroscopy with laser harmonics", Appl. Phys. Lett. **65**, 517 (1994).

[13] Ph. Balcou, P. Salieres, K. S. Budil, T. Ditmire, M. D. Perry and A. L'Huillier, "High-order harmonic generation in rare gases: a new source in photoionization spectroscopy", Z. Phys. D **34**, 107 (1995).

[14] J. Larsson, E. Mevel, R. Zerne, A. L'Huillier, C.-G. Wahlstrom, and S. Svanberg, "Two-colour time-resolved spectroscopy of helium using high-order harmonics", J. Phys. B **28**, L53 (1995).

[15] M. M. Murnane, H. C. Kapteyn, S. P. Gordon, R. W. Falcone, "Ultrashort X-Ray Pulses", Appl. Phys. B**58**, 261 (1994)

[16] T. Ditmire, K. Kulander, J. K. Crane, H. Hguyen, M. D. Perry, "Calculation and measurement of high-order harmonic energy yields in helium", J. Opt. Soc. Am. B**13**, 406 (1996)

[17] John F. Reintjes, *Nonlinear optical parametric processes in liquids and gases* (Academic Press, Orlando, 1984).

[18] Kenneth C. Kulander, Kenneth J. Schafer and Jeffrey L. Krause, "Time-Dependent Studies of Multiphoton Processes", in *Atoms in Intense Laser Fields*, edited by M. Gavrila (Academic, Boston, 1992).

[19] K. C. Kulander and B. W. Shore, "Calculations of Multipole-Harmonic Conversion of 1064-nm Radiation in Xe", Phys. Rev. Lett. **62**, 524 (1989).

[20] M. Ferray, A. L'Huillier, X. F. Li, L. A. Lompre, G. Mainfray, and C. Manus, J. Phys. B **21**, L31 (1988).

[21] A. L'Huillier, K. J. Schafer, and K. C. Kulander, "High-Order harmonic generation in Xenon at 1064nm: the role of phase matching", Phys. Rev. Lett. **66**, 2200 (1991).

[22] Anne L'Huillier, Philippe Balcou, Sebastien Candel, Kenneth J. Schafer, and Kenneth C. Kulander, "Calculations of high-order harmonic generation processes in xenon at 1064 nm", Phys. Rev. A **46**, 2778 (1992).

[23] Jeffrey L. Krause, Kenneth J. Schafer, and Kenneth C. Kulander, "High-order harmonic generation from atoms and ions in the high intensity regime", Phys. Rev. Lett **68**, 3535 (1992).

[24] J. K. Crane, M. D. Perry, S. Herman, and R. W. Falcone, "High-field harmonic generation in helium", Opt. Lett. **17**, 1256 (1992).

[25] P. B. Corkum, "A plasma perspective on strong-field multiphoton ionization", Phys. Rev. Lett. **71**, 1994 (1993).

[26] L. D. Landau and E. M. Lifshitz, *Quantum Mechanics* 2nd ed. (Pergamon, New York, 1965)

[27] L. V. Keldysh, "Ionization in the field of a strong electromagnetica wave", Sov. Phys. JETP **20**, 1307 (1965).

[28] A. M. Perelomov, V. S. Popov and M. V. Terent'ev, "Ionization of atoms in an alternating electric field", Sov. Phys. JETP **23**, 924 (1996).

[29] M. V. Ammosov, N. B. Delone, and V. P. Krainov, "Tunnel ionization of complex atoms and of atomic ions in an alternating electromagnetic field", Sov. Phys. JETP **64**, 1191 (1986).

[30] K. J. Schafer, Baorui Yang, L. F. DiMauro, and K. C. Kulander, "Above threshold ionization beyond the high harmonic cutoff", Phys. Rev. Lett **70**, 1599 (1993).

[31] P. B. Corkum, N. H. Burnett, and F. Brunel, "Multiphoton ionization in large ponderomotive potentials", in *Atoms in Intense Laser Fields*, edited by M. Gavrila (Academic, Boston, 1992).

[32] M. Lewenstein, Ph. Balcou, M. Yu. Ivanov, Anne L'Huillier, and P. B. Corkum, "Theory of high-harmonic generation by low-frequency laser fields", Phys. Rev. A **49**, 2117 (1994).

[33] P. Dietrich, N. H. Burnett, M. Ivanov, and P. B. Corkum, "High harmonic generation and correlated two electron multiphoton ionization with elliptically polarized light", Phys. Rev. A **50**, R3585 (1994).

[34] N. H. Burnett, C. Kan, and P. B. Corkum, "Ellipticity and polarization effects in harmonic generation in ionizing neon", Phys. Rev. A **51**, R3418 (1995).

[35] Anne L'Huillier, Kenneth J. Schafer and Kenneth C. Kulander, "Theoretical aspects of intense field harmonic generation", J. Phys. B **24**, 3315 (1991)

[36] Anne L'Huillier, M. Lewenstein, P. Salieres and Ph. Balcou, "High-order harmonic-generation cutoff", Phys. Rev. A **48**, R3433 (1993).

[37] S. C. Rae and K. Burnett, "Generation and propagation of high-order harmonic in a rapidly ionizing medium", Phys. Rev. A **50**, 3438 (1994).

[38] P. L. Shkolnikov, A. E. Kaplan, and A. Lago, "Phase matching for Large-scale frequency upconversion in plasma", Opt. Lett. **20**, 1700 (1993).

[39] P. L. Shkolnikov, A. E. Kaplan, A. Lago, "Phase-matching optima for high-order multiwave mixing and harmonic generation beyond perturbation limit", Opt. Comm. **111** 93 (1994).

[40] H. M. Milchberg, C. G. Durfee III, and T. J. McIlrath, "High-Order Frequency Conversion in the Plasma Waveguide", Phys. Rev. Lett. **75** 2494 (1995).

[41] R. Rankin, C. E. Capjack, N. H. Burnett and P. B. Corkum, "Refraction effects associated with multiphoton ionization and ultrashort-pulse laser propagation in plasma waveguides", Opt. Lett. **16**, 835 (1991).

[42] F. Brunel, "Harmonic generation due to plasma effects in a gas undergoing multiphoton ionization in the high-intensity limit", J. Opt. Soc. Am B**7**, 521 (1990).

[43] N. H. Burnett, C. Kan and P. B. Corkum, "High harmonic generation in ionizing atomic gases with elliptically polarized light", presented at the International Topical Conference on Research Trends on Nonlinear and Quantum Optics, Sponsored by the American Institute of Physics, November 22 - 24, 1993, La dolla, California, USA.

[44] Thomas Brabec, Misha Yu. Ivanov, and Paul B. Corkum, "Coulomb focusing in intense field atomic processes", Phys. Rev. A **54**, R2551 (1996).

[45] N. B. Delone and V. P. Krainov, *Multiphoton Processes in Atoms*, (Springer-Verlag, Berlin, 1994)

[46] S. Augst, D. D. Meyerhofer, D. Strickland, and S. L. Chin, "Laser ionization of noble gases by Coulomb-barrier suppression", J. Opt. Soc. Am. B **8**, 858 (1990)

[47] M. Y. Ivanov and K. Rzazewski, "Are free-free transitions a good basis for nonlinear optics", J. Mod. Opt. **39**, 2377 (1992).

[48] G. Arfken, *Mathematical methods for physicists*, 3rd ed. (Academic Press, San Diego, 1985).

[49] J. Jackson, *Classical electrodynamics* 2nd ed. (John Wiley & Sons, New York, 1962).

[50] G. D. Smith, *Numerical Solution of Partial differential Equations: Finite Difference Methods*, 2nd ed. (Clarendon Press, Oxford).

[51] E. Esarey, G. Joyce, and P. Sprangle, "Frequency up-shifting of laser pulses by copropagating ionization fronts", Phys. Rev. A **44**, 3908 (1991).

[52] M. Nisoli, S. DeSilvestri, O. Svelto, R. Szipocs, K. Ferencz, Ch. Spielman, S. Sartania, and F. Krausz, "Compression of high energy laser pulses below 5 fs", to be published.

[53] Ivan P. Christov, Margaret M. Murname, and Henry C. Kapteyn, "High-Harmonic Generation of Attosecond Pulses in the Single-Cycle Regime", Phys. Rev. Lett. **78**, 1251 (1997).

[54] Kenneth J. Schafer and Kenneth C. Kulander, "High Harmonic Generation from Ultrafast Pump Lasers", Phys. Rev. Lett. **78**, 638 (1997).

[55] E. Yablonovich, "Energy Conservation in the Picosecond and Subpicosecond Photoelectric Effect ", Phys. Rev. Lett. **60**, 795 (1988).

[56] Pasçal Salieres, Anne L'Huillier, and Maciej Lewenstein, "Coherence Control of High-Order Harmonics", Phys. Rev. Lett. **74**, 3776 (1995).

Appendix A

Stationary Phase Evaluation of the qth Harmonic Dipole Component

The method of stationary phase is useful in evaluating the approximate value of an integral of the form [1]:

$$I = \int F(t) e^{i\Phi(t)} dt \tag{A.1}$$

If the function $F(t)$ is slowly varying in time while the phase $\Phi(t)$ is rapidly varying, the main contribution to the integral should come from the times at which the phase Φ is stationary with respect to time, i.e., $\dot{\Phi} = 0$ where $\dot{\Phi}$ is the first time derivative of Φ. At other times, the function $e^{i\Phi(t)}$ oscillates rapidly from positive to negative values, meaning that the integrand averages to almost zero. As a result, it can be shown that the integral can be given approximately by:

$$I \approx I_s = \left(\frac{2\pi i}{\ddot{\Phi}(t_s)} \right)^{1/2} F(t_s) e^{i\Phi(t_s)} \tag{A.2}$$

where t_s is the time at which $\dot{\Phi} = 0$ and $\ddot{\Phi}$ is the second time derivative of Φ.

From Eqn. (2.39), the semi-classical dipole moment can be written as:

$$d(t) = D(t) e^{-iS(t)} + D^*(t) e^{+iS(t)} \tag{A.3}$$

---

[1] A discussion of this method can be found in Ref. [49] p316-p317.

Then if the dipole moment can be expanded as a sum of harmonic components: $d(t) = \sum_q d_q e^{iq\omega_o t}$, the envelope of an individual component can be calculated as:

$$d_q = I_1 + I_2 = \frac{1}{t_o}\int_0^{t_o} dt D(t) e^{-i\Phi_1(t)} + \frac{1}{t_o}\int_0^{t_o} dt D^*(t) e^{+i\Phi_2(t)} \tag{A.4}$$

where $\Phi_1 = S + q\omega_o t$ and $\Phi_2 = S - q\omega_o t$. Using the stationary analysis, the main contribution to I_2 in comes from the time when:

$$\frac{dS}{dt} - q\omega_o = 0 \tag{A.5}$$

Using $S = (1/\hbar)\int_{t'}^{t} dt''(p^2(t'')/2m + I_p)$ and assuming the ionization time t' is a weak function of the recollision time t, this stationary phase condition leads to:

$$\frac{p^2(t_q)}{2m} + I_p - q\hbar\omega_o = 0 \tag{A.6}$$

where t_q is the time at which the above condition is satisfied. It should be noted that this equation is just the cutoff law described in Chapter 1. From Figure 2.3, it is seen that for a given $q\hbar\omega_o$ below $I_p + 3.2\, U_p$, there are four different times at which the above stationary phase condition is satisfied. As for the first integral, I_1, the stationary phase condition is:

$$\frac{p^2(t_q)}{2m} + I_p + q\hbar\omega_o = 0 \tag{A.7}$$

Since all terms in the above equation are positive, there is no stationary phase for I_1. As a result, I_1 should be negligible compared to I_2. Consequently,

$$d_q = \sum_l \frac{D^*(t_q^l)}{2t_o}\left(\frac{2\pi i}{\dot{KE}_r(t_q^l)/\hbar}\right)^{1/2} e^{i[S(t_q^l) - q\omega_o t_q^l]} \tag{A.8}$$

where t_q^l are the four recombination time at which the stationary phase condition is satisfied and $\dot{KE}_r = \ddot{S}$ where KE_r is the recollision kinetic energy given by $p^2/(2m)$.

Appendix B

The One Dimension HHG Wave Solver

An efficient numerical scheme has been developed to solve the one dimensional HHG wave equations (Eqn. (2.71) and Eqn. (2.72)). Details of this scheme are described below.

Normalization of wave equations

The wave equations can be conveniently solved in the normalized form where variables are expressed in units which are relevant to the physical problem. Here, the normalization is given by:

$$\begin{aligned} t/t_o &\rightarrow t \\ z/\lambda_o &\rightarrow z \\ E/E_A &\rightarrow E \\ P/E_A &\rightarrow P \\ n_e/n_c &\rightarrow n_e \end{aligned} \tag{B.1}$$

$$\tag{B.2}$$

where t_o is the laser cycle, λ_o is the laser wavelength, E_A is the atomic unit of electric field, and n_c is the critical density in the laser field. The wave equations then become:

$$\frac{\partial^2 E_1}{\partial z^2} - \frac{\partial^2 E_1}{\partial t^2} + 4\pi i \left(\frac{\partial E_o}{\partial z} + \frac{\partial E_1}{\partial t} \right) - (2\pi)^2 n_e E_1 = 0 \tag{B.3}$$

$$\begin{aligned} \frac{\partial^2 E_q}{\partial z^2} - \frac{\partial^2 E_q}{\partial t^2} + 4\pi i q \left(\frac{\partial E_q}{\partial z} + \frac{\partial E_q}{\partial t} \right) - (2\pi)^2 n_e E_q \\ = 4\pi \left(\frac{\partial^2 P_q}{\partial t^2} - 4\pi i q \frac{\partial P_q}{\partial t} - (2\pi)^2 q^2 P_q \right) \end{aligned} \tag{B.4}$$

Finite difference scheme

A second order finite difference scheme based on that given in Ref. [50] is used to solve the HHG wave equations. In this scheme, with the fields discretized as $F^{j,k} = F(k\Delta z, j\Delta t)$, the partial derivatives are computed as:

$$\begin{aligned} \frac{\partial^2 F}{\partial z^2} &= \frac{F^{j,k+1} - 2F^{j,k} + F^{j,k-1}}{\Delta z^2} \\ \frac{\partial^2 F}{\partial t^2} &= \frac{F^{j+1,k} - 2F^{j,k} + F^{j-1,k}}{\Delta t^2} \\ \frac{\partial F}{\partial z} &= \frac{F^{j,k+1} - F^{j,k-1}}{2\Delta z} \\ \frac{\partial F}{\partial t} &= \frac{F^{j+1,k} - F^{j-1,k}}{2\Delta t} \end{aligned} \tag{B.5}$$

The resulting finite difference equations are then given by:

$$F_1 E_1^{j+1,k} - A_1 E_1^{j,k+1} - (B_1 + B_{11} n_e^{j,k}) E_1^{j,k} - C_1 E_1^{j,k-1} - D_1 E_1^{j-1,k} = 0 \tag{B.6}$$

$$F_q E_q^{j+1,k} - A_q E_q^{j,k+1} - (B_q + B_{q1} n_e^{j,k}) E_q^{j,k} - C_o E_q^{j,k-1} - D_q E_q^{j-1,k} = S \tag{B.7}$$

where

$$S = -\left(H_a P_q^{j+1,k} + H_b P_q^{j,k} + H_c P_q^{j-1,k} \right) \tag{B.8}$$

and the coefficients are given by:

$$A_1 = m^2 + 2\pi i m \Delta t$$

$$
\begin{aligned}
B_1 &= -2m^2 + 2 \\
B_{11} &= -(2\pi\Delta t)^2 \\
C_1 &= m^2 - 2\pi i m\Delta t \\
D_1 &= -1 - 2\pi i\Delta t \\
F_1 &= 1 - 2\pi i\Delta t
\end{aligned}
\qquad \text{(B.9)}
$$

$$
\begin{aligned}
A_q &= m^2 + 2\pi i q m\Delta t \\
B_q &= -2m^2 + 2 \\
B_{q1} &= -(2\pi\Delta t)^2 \\
C_q &= m^2 - 2\pi i q m\Delta t \\
D_q &= -1 - 2\pi i q\Delta t \\
F_q &= 1 - 2\pi i q\Delta t
\end{aligned}
\qquad \text{(B.10)}
$$

$$
\begin{aligned}
H_a &= 4\pi(1 - 2\pi i q\Delta t) \\
H_b &= -4\pi(2 + (2\pi q\Delta t)^2) \\
H_c &= 4\pi(1 + 2\pi i q\Delta t)
\end{aligned}
\qquad \text{(B.11)}
$$

and

$$m = \frac{\Delta t}{\Delta z} \qquad \text{(B.12)}$$

Initial conditions, boundary conditions and method of solution

Assuming the fields are to be solved from $t = 0$ to $t = N_t\Delta t = T_t$ for $z = 0$ to $z = N_z\Delta z = Z_t$, the finite difference equations can be readily solved when two initial conditions, $E^{-1,k}$ and $E^{0,k}$, and two boundary conditions, $E^{j,0}$ and E^{j,N_z}, are provided in each equation. These conditions are obtained as follows. If the peak of the incident laser pulse arrives at the left boundary ($z = 0$) much later than $t = 0$, say a few FWHM's, the driving field as well as the harmonic field can be assumed to be zero inside the medium prior to $t = 0$. Thus the initial conditions are:

$$\begin{aligned} E_1(z, t = 0) &= 0 \\ E_1(z, t = -\Delta t) &= 0 \\ E_q(z, t = 0) &= 0 \\ E_q(z, t = -\Delta t) &= 0 \end{aligned} \tag{B.13}$$

Now, if the simulation region is made large enough, say $Z_t > c(T_t + 10 * FWHM)$ where c is the speed of light, no fields can propagate to the right boundary ($z = Z_t$) within T_t. Therefore, together with the left boundary conditions discussed in Section 2.2.1, the boundary conditions for the driving and harmonic fields should be:

$$\begin{aligned} E_1(z = 0, t) &= E_L(z = 0, t) \\ E_1(z = Z_t, t) &= 0 \\ E_q(z = 0, t) &= 0 \\ E_q(z = Z_t, t) &= 0 \end{aligned} \tag{B.14}$$

With these initial and boundary conditions, the difference equations can be explicitly solved as:

$$E_1^{j+1,k} = \frac{1}{F_1}\left(A_1 E_1^{j,k+1} + (B_1 + B_{11} n_e^{j,k}) E_1^{j,k} + C_1 E_1^{j,k-1} + D_1 E_1^{j-1,k}\right) \tag{B.15}$$

$$E_q^{j+1,k} = \frac{1}{F_q}\left(A_q E_q^{j,k+1} + (B_q + B_{q1} n_e^{j,k}) E_q^{j,k} + C_o E_q^{j,k-1} + D_q E_q^{j-1,k} - S\right) \tag{B.16}$$

where the electron density is calculated by:

$$\begin{aligned} n_e^{j,k} &= n_o\left(1 - e^{-Q^{j,k}}\right) \\ Q^{j,k} &= Q^{j-1,k} + \Delta t R_t(E_1^{j-1,k}) \end{aligned} \tag{B.17}$$

Now, by using Eqn. (2.74) and noting that the probability of ionization is given by $P^{j,k} = 1 - \exp[-Q^{j,k}]$, the polarization P_q at each grid point can be calculated as:

$$P_q^{j,k} = n_o e^{-Q^{j,k}} e^{\arg E_1^{j,k}} D_q^{j,k} \tag{B.18}$$

where $D_q^{j,k} = D_q(E_1^{j,k})$ and

$$D_q(E_1) = \int_0^{t_o} dt'' \bar{d}(|E_1| \cos(\omega_o t''), t'') e^{iq\omega_o t''} \tag{B.19}$$

In practice, a table of D_q is obtained as a function of $|E_1|$ prior to the actual simulation. During the simulation, $D_q^{j,k}$ is obtained by simple linear interpolation from the D_q table. This greatly reduces the computational time for each simulation by not having to calculate the numerically intensive integral (Eqn. (B.19)) at each grid point. Finally, this numerical scheme has been shown to be stable for [50]:

$$m < 1 \tag{B.20}$$

However, for computation efficiency, m should be set to be as close to unity as possible. This is because in wave propagation problems, if Δz is small enough to resolve the spatial variation of the propagating fields, $\Delta t = \Delta z$ (or in real units $\Delta t = \Delta z/c$) should also be small enough to resolve the temporal variation of the fields. Thus if $m \ll 1$, then $\Delta t \ll \Delta z$ and many unnecessary temporal grid points will be used.

The moving frame technique

The technique utilizes some general properties of the finite difference scheme to avoid calculating unnecessary computation points. The basic principle can be explained as follows. First, since the initial condition for E_1 is $E_1^{0,k} = E_1^{-1,k} = 0$ for $k \geq 0$, it is seen from Eqn. (B.15) that $E_1^{1,k} = 0$ for $k \geq 1$. Similarly, $E_1^{2,k} = 0$ for $k \geq 2$, $E_1^{3,k} = 0$ for $k \geq 3$ and so on. As a result, E_1 at the computation points to the right of a straight line with a slope $m = \Delta t/\Delta z$ passing through the origin should be all zero. This region is denoted as I in Figure B.1 as bound by the line l_1 and the z-axis. Furthermore, since E_1 is zero in this region, $P_q(E_1^{j,k})$ and consequently $E_q^{j,k}$ as calculated from Eqn. (B.16) should also be zero in this region. Now, consider a second straight line, l_2, having a slope m and intersecting the t-axis at $T_p = N_p\Delta t$. From Eqn. (B.15) and Eqn. (B.16), it is seen that in each time step the fields to the right of l_2 at the current time step depend only on the fields in the previous two time steps *also to the right of* l_2. Therefore, computation of the fields to the right of l_2 does not require the knowledge of the fields in region III (see Fig. B.1) as bound by l_2 and the t-axis. Consequently, if the interesting computation region is to the right of l_2, calculation of the fields in both regions I and III can be totally ignored.

Physically, the calculated fields in region II (which is bound by l_1, l_2 and the t-axis) represent the solution to the wave equations as viewed by a window having a spatial width of Z_p and propagating at the speed c/m where c is the speed of light. Since $m < 1$ for numerical stability, the numerical scheme simply implies that information in region II cannot propagate faster than c to affect information in region I. Similarly, information in region I cannot affect information in region II. Now, since E_1 and E_q both propagate at about the speed of light and E_q is only generated in a region where E_1 is appreciable, a moving frame with a spatial extend of a few times $c(FWHM)$, initially centered at the peak of E_1, can be used to greatly reduce the computation time.

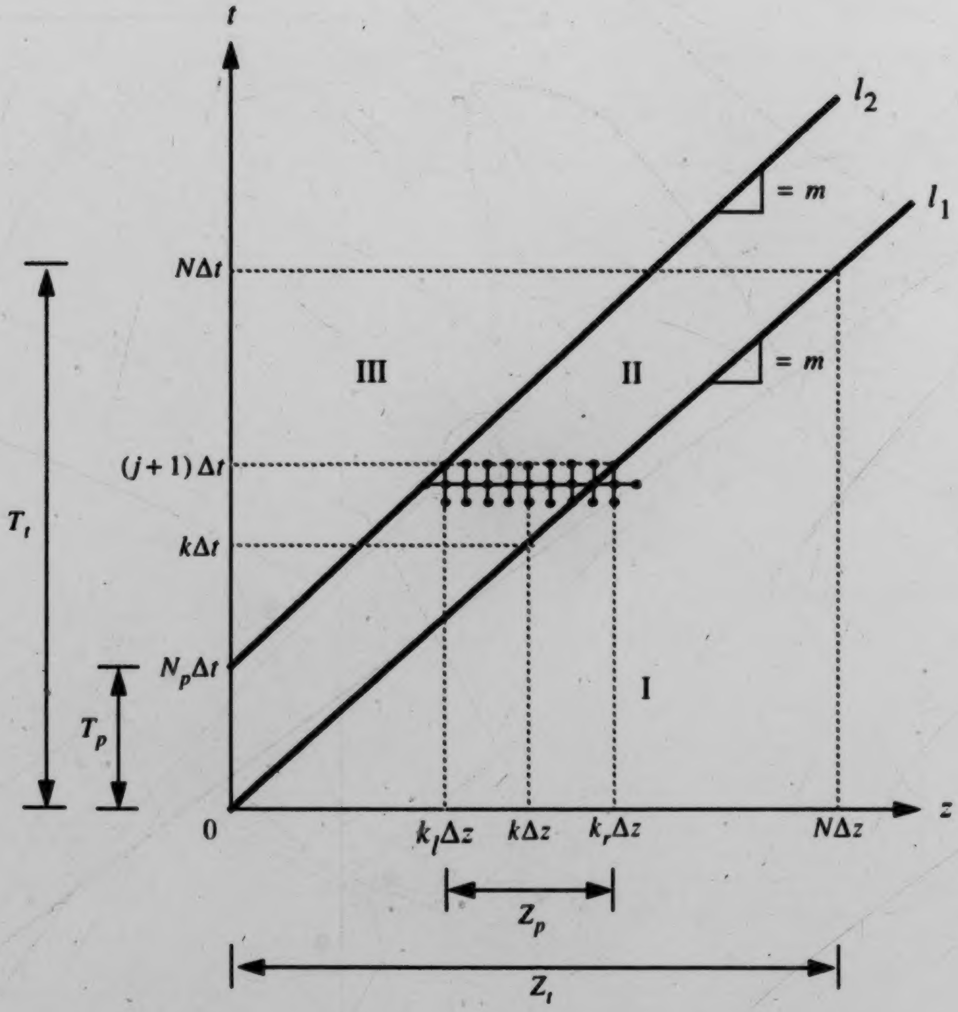
t
l_2
l_1
$= m$
$= m$
$N\Delta t$
III
II
$(j+1)\,\Delta t$
T_t
$k\Delta t$
$N_p\Delta t$
T_p
I
0
$k_l\Delta z$
$k\Delta z$
$k_r\Delta z$
$N\Delta z$
z
Z_p
Z_t

Figure B.1: The computation grid and the moving frame. Z_t and T_t are respectively the total simulation length and time; Z_p and T_p are respectively the spatial and temporal extend of the moving frame; and $k_l\Delta z$ and $k_r\Delta z$ are respectively the left and right spatial boundaries of the moving frame. The solid circles denote the grid points near the $(j+1)\Delta t$ time step.

Appendix C

The One Dimension HDM Wave Solver

The HDM wave equations are solved using a similar numerical scheme as that used in solving the HHG wave equations. Using the same normalized variables defined by Eqn. (B.2), the wave equations become:

$$\frac{\partial^2 E_1}{\partial z^2} - \frac{\partial^2 E_1}{\partial t^2} + 4\pi i \left(\frac{\partial E_o}{\partial z} + \frac{\partial E_1}{\partial t} \right) - (2\pi)^2 n_e E_1 = 0 \tag{C.1}$$

$$\frac{\partial^2 E_c}{\partial z^2} - \frac{\partial^2 E_c}{\partial t^2} + 4\pi i q_c \left(\frac{\partial E_c}{\partial z} + \frac{\partial E_c}{\partial t} \right) - (2\pi)^2 n_e E_c = 0 \tag{C.2}$$

$$\begin{aligned} \frac{\partial^2 E_q}{\partial z^2} - \frac{\partial^2 E_q}{\partial t^2} + 4\pi i q \left(\frac{\partial E_q}{\partial z} + \frac{\partial E_q}{\partial t} \right) - (2\pi)^2 n_e E_q \\ = 4\pi \left(\frac{\partial^2 P_q}{\partial t^2} - 4\pi i q \frac{\partial P_q}{\partial t} - (2\pi)^2 q^2 P_q \right) \end{aligned} \tag{C.3}$$

where $q_c = \omega_c/\omega_o$. The same second order finite difference scheme used to solve the HHG wave equations are used here to solve the HDM wave equations. With the initial and boundary conditions for E_1 and E_q given by Eqn. (B.13) and Eqn. (B.14) and the initial and boundary conditions for E_c given by:

$$\begin{aligned} E_c(z, t = 0) &= 0 \\ E_c(z, t = -\Delta t) &= 0 \end{aligned}$$

$$\begin{aligned} E_c(z=0,t) &= E_c(z=0,t) \\ E_c(z=Z_t,t) &= 0 \end{aligned} \tag{C.4}$$

The fields are solved as:

$$E_1^{j+1,k} = \frac{1}{F_1}\left(A_1 E_1^{j,k+1} + (B_1 + B_{11} n_e^{j,k}) E_1^{j,k} + C_1 E_1^{j,k-1} + D_1 E_1^{j-1,k}\right) \tag{C.5}$$

$$E_c^{j+1,k} = \frac{1}{F_c}\left(A_c E_c^{j,k+1} + (B_c + B_{c1} n_e^{j,k}) E_c^{j,k} + C_c E_c^{j,k-1} + D_c E_c^{j-1,k}\right) \tag{C.6}$$

$$E_q^{j+1,k} = \frac{1}{F_q}\left(A_q E_q^{j,k+1} + (B_q + B_{q1} n_e^{j,k}) E_q^{j,k} + C_o E_q^{j,k-1} + D_q E_q^{j-1,k} - S\right) \tag{C.7}$$

where the electron density is calculated by Eqn. (B.17), the coefficients for E_1 and E_q are given by Eqn. (B.9) andEqn. (B.10), and the coefficients for the E_c equation are:

$$\begin{aligned} A_c &= m^2 + 2\pi i q_c m \Delta t \\ B_c &= -2m^2 + 2 \\ B_{c1} &= -(2\pi\Delta t)^2 \\ C_c &= m^2 - 2\pi i q_c m \Delta t \\ D_c &= -1 - 2\pi i q_c \Delta t \\ F_c &= 1 - 2\pi i q_c \Delta t \end{aligned} \tag{C.8}$$

The polarization P_q at each grid point is calculated as:

$$P_q^{j,k} = n_o e^{-Q^{j,k}} e^{\arg E_1^{j,k}} D_q^{j,k}. \tag{C.9}$$

where $D_q^{j,k} = D_q(E_1^{j,k}, E_c^{j,k})$ and

$$D_q(E_1, E_c) = \int_0^{t_o} dt'' \bar{d}(|E_1|\cos(\omega_o t''), \underline{E}_c, t'') e^{iq\omega_o t''} \tag{C.10}$$

Here the real control field $\underline{E}_c$ at each grid point is obtained as:

$$\underline{E}_c^{j,k} = |E_c^{j,k}| \cos[(\omega_c/c)(k\Delta z - j\Delta t) - \arg E_c^{j,k}] \tag{C.11}$$

Similar to the HHG wave solver, a table of D_q is obtained as a function of $|E_1|$ *and* $\underline{E_c}$ prior to the actual simulation. During the simulation, $D_q^{j,k}$ is obtained by simple bi-linear interpolation from the D_q table. Finally, the moving frame technique is also used here to improve computation efficiency.

Appendix D

Phase and Amplitude of an Ultra-Short Laser Pulse in a Steep Ionization Front

The phase and amplitude of a very short duration laser pulse can be obtained as follows. First, by using the normalized variables defined by Eqn. (B.2), the envelope wave equation for the fundamental field (Eqn. (4.2)) in the retarded time frame ($z' = z$ and $t_R = t - z/c$) is given by:

$$\frac{\partial^2 E_1}{\partial z'^2} - 2\frac{\partial^2 E_1}{\partial t_R \partial z'} + 4\pi i \frac{\partial E_1}{\partial z'} - (2\pi)^2 n_e E_1 = 0 \tag{D.1}$$

Secondly, it is assumed that the complex envelope E_1 can be written as $E_1(z', t_R) = Ae^{iS}$ where A is a real envelope and S is the phase. It is further assumed that the real envelope is not significantly distorted as it propagates in the medium and is therefore a function of t_R only, i.e. $A = A(t_R)$. It is also assumed that the phase is a linear function of z' given by $S(z', t_R) = z'f(t_R)$. Finally, it is assumed that the relativistic ionization front n_e also propagates undistorted in the medium and is therefore also a function of t_R only. The assumptions concerning the fundamental envelope and ionization front are made based on the the simulation results observed in Figure 4.9

in Section 4.3. Using these assumptions, the wave equation becomes:

$$\frac{df}{dt_R} - f\left(2\pi i - \frac{\frac{dA}{dt_R}}{A}\right) - 2i\pi^2 n_e(t_R) = 0 \tag{D.2}$$

In obtaining Eqn. (D.2), terms involving f^2 and z' have been neglected. These omissions are reasonable if $f \ll 1$ and have been justified by Figure 4.10 in Section 4.3 where the semi-analytical results obtained here agree very well with the simulation results. Now, as can be seen from the results shown in Figure 4.10, f becomes significant when ionization is appreciable. In this region, the term dA/dt_R, which is proportional to $t_R \,/\, \tau^2$ where τ is the FWHM of the fundamental pulse, should be very small. Consequently, the phase of the fundamental envelope near the ionization front is described by:

$$S = \frac{z'}{\lambda_o} f(t_R) \tag{D.3}$$

where the function f is governed by the following differential equation:

$$\frac{df}{d(t_R/t_o)} - 2\pi i f - 2i\pi^2 \frac{n_e(t_R)}{n_c} = 0 \tag{D.4}$$

Here, z', t_R and n_e are expressed in real units. It should be noted that since Eqn. (D.4) is a complex equation, the phase S is also a complex quantity. Consequently, the real phase of the fundamental envelope should be given by:

$$\theta_1 = \frac{z'}{\lambda_o} \mathrm{Re}[f(t_R)] \tag{D.5}$$

It is also found that by subsituting $f = \mathrm{Re}[f] + i\mathrm{Im}[f]$ into Eqn. (D.4) and grouping together real and imaginary terms, Re[f] is related to Im[f] as:

$$\mathrm{Im}[f] = -\frac{z'}{2\pi\lambda_o} \frac{d\mathrm{Re}[f]}{d(t_R/t_o)} \tag{D.6}$$

Consequently, the magnitude of the fundamental envelope is modified by:

$$|E_1| = A(t_R) \exp\left(-\frac{z'}{2\pi\lambda_o} \frac{d\mathrm{Re}[f]}{d(t_R/t_o)}\right) \tag{D.7}$$

Finally, since the instantaneous frequency shift is defined as $\Delta\omega = -d\theta_1/dt_R$, the magnitude of the fundamental envelope can also be written as:

$$|E_1| = A(t_R) e^{-\frac{\Delta\omega}{\omega_o}} \tag{D.8}$$